ANALYSIS OF UNSATURATED FLOW BASED ON PHYSICAL DATA RELATED TO LOW-LEVEL RADIOACTIVE WASTE DISPOSAL, CHIHUAHUAN DESERT, TEXAS

Bridget R. Scanlon, Fred P. Wang, and Bernd C. Richter

Final Contract Report

Prepared for
Texas Low-Level Radioactive Waste Disposal Authority
under Interagency Contract Number IAC(90-91)0268

Bureau of Economic Geology
W. L. Fisher, Director
The University of Texas at Austin
Austin, Texas 78713

July 1990

CONTENTS

Figures

Tables

EXECUTIVE SUMMARY

Unsaturated flow in the Chihuahuan Desert of Texas was analyzed to evaluate the suitability of this region for low-level radioactive waste disposal because thick unsaturated zones that have low moisture fluxes in arid regions are considered suitable for radioactive waste disposal. The principal study area was instrumented with neutron-probe access tubes and psychrometers with which to monitor moisture content and water potential, respectively. The absence of temporal variations in moisture content monitored in deep (41 m [135 ft]) profiles indicated that recharge pulses are not moving through the system. Penetration of moisture after rainfall was restricted to the uppermost meter of the unsaturated zone because of the low degree of saturation of the surficial sediments. Water potentials were as low as –15.6 MPa near land surface in the summer. Except in the shallow subsurface after precipitation events, water potentials generally decreased upward; this trend indicated primarily upward flow under isothermal conditions, probably controlled by evapotranspiration.

The computer code, TRACRN, was used to evaluate various unsaturated-flow processes in this system. Numerical simulations of upward flow indicated that small variations in water content result in large variations in water potential in dry unsaturated zones. One-dimensional simulation of infiltration was calibrated using ^{36}Cl data. Sensitivity analyses suggested that applied flux and initial water potential are the most critical factors in controlling the propagation of the wetting front. Analyses of potential leakage from the base of a possible facility indicated that the direction as well as the net rate of water movement is controlled by lithologic layering in the system. Simulations of downward leakage rates that are similar to the saturated hydraulic conductivity of the deep clays showed that a saturated zone will develop at the contact between the shallow coarse material and underlying clays.

INTRODUCTION

The unsaturated zone in an arid region of West Texas is being considered as a repository of low-level radioactive waste. The purpose of this study was to determine the predominant direction and rate of water movement in the unsaturated zone by monitoring moisture content, water potential, and temperature and by measuring hydraulic conductivity. These data were used in numerical simulations to evaluate unsaturated-flow processes. Potential pathways for waste migration from a waste-disposal facility include upward movement into the atmosphere, downward movement to the water table, or lateral movement to arroyos. Although the facility will be designed to contain the waste, reliance will be placed on the natural system itself to act as a barrier to waste migration for the 500-yr time period specified by the regulatory guidelines of the U.S. Nuclear Regulatory Commission (10 CFR 61, NUREG 0902, and NUREG 1200).

Description of Principal Study Area

The principal study area, approximately 65 km (40 mi) southeast of El Paso, lies within the Chihuahuan Desert of Texas (fig. 1) in the Hueco Bolson, a sediment-filled basin approximately 200 m (656 ft) thick at the principal study area and overlying Cretaceous bedrock that is exposed in the Diablo Plateau northeast of the study area. Ground water flows southwesterly from the Diablo Plateau to the Rio Grande and is approximately 150 m (492 ft) deep within the study area (Mullican and others, 1989). The unsaturated zone consists of approximately 0 to 15 m (0 to 49 ft) of coarse-grained material of the Tertiary/Quaternary-age Camp Rice Formation and 140 m (459 ft) of clay containing interbedded silts and sands of the underlying Tertiary-age Fort Hancock Formation (fig. 2). Extreme local textural variations from clay to gravel were observed in trenches dug to a depth of 7 m (23 ft). A discontinuous layer of caliche lies at approximately a 2-m (6.6-ft) depth. Caliche deposits result from successive periods of infiltration and evapotranspiration of soil water in the shallow unsaturated zone and are thought to reflect the lower limit of moisture penetration (Winograd, 1981).

The topography at the site is relatively flat—slopes are less than 1 percent—and the elevation is approximately 1,300 m (4,265 ft) (fig. 1). Ephemeral streams on the site have no well-defined channels and drain into arroyos that border the principal study area. In general, both the streams and arroyos are dry except after rainfall events. Shrubs such as creosote (*Larrea tridentata*) and mesquite (*Prosopis glandulosa*) are common and root to depths of 1 to 5 m (3 to 16 ft).

The regional climate is subtropical arid (Larkin and Bomar, 1983). Long-term meteorologic data were obtained at Fort Hancock, situated 18 km (11 mi) southwest of the study area, and El Paso, 65 km (40 mi) to the northwest (Griffiths, personal communication, 1989). Precipitation in the region is characterized by large interannual variations (110 to 430 mm [4.3 to 17 inches]). During the monitoring period (July 1988 through December 1989) annual precipitation, recorded at four different rain gauges, ranged from 115 to 186 mm (4.5 to 7.5 inches) (fig. 3) (Baumgardner, 1990). These values are lower than the long-term average annual precipitation of 280 mm (11 inches). Approximately 60 percent of the precipitation falls as local, intense, short-duration convective storms from June through September, when temperature and potential evaporation are highest (fig. 4). Minor winter frontal storms are of longer duration. Mean annual class-A pan evaporation is approximately seven times mean annual precipitation. Mean monthly temperatures range from 5°C in December to 28°C in July. High-intensity precipitation events result in large amounts of runoff, estimated by hydrologic modeling to be as much as 50 percent of the precipitation (Akhter, 1989).

Hydrodynamic Approach

The potential gradient is used to assess the direction and rate of water movement because water flows from regions of high to low potential. Although temporal variations in moisture content are generally used to evaluate the movement of recharge pulses through the unsaturated zone, moisture content is discontinuous across different lithologies, and variations in moisture content with depth do not indicate the direction of water movement. In contrast, energy potential is continuous across different materials. Many potential gradients may be important in the unsaturated zone, as indicated by the generalized flow law (modified from de Marsily [1986])

$$q = -L_1 \nabla\Phi - L_2 \nabla T - L_3 \nabla C, \qquad (1)$$

where q is the flux,

L_1, L_2, and L_3 are proportionality constants,

∇ is the gradient operator,

Φ is hydraulic head,

T is temperature,

and C is chemical concentration.

The hydraulic head is the sum of the matric (ψ_m) and gravitational (ψ_g) potential gradients. Matric potential results from capillary and adsorptive forces. Gravitational potential is the elevation above the water table, which is used as a reference datum. Chemical-concentration gradients are equivalent to osmotic-potential (ψ_π) gradients. A priority concerning unsaturated-flow systems is the determination of the relative importance of the different potential gradients. In many flow systems temperature and concentration gradients are negligible, and the flow law can be simplified to the Buckingham-Darcy Law,

$$q = -K(\theta)\, \nabla\Phi, \qquad (2)$$

where K is the hydraulic conductivity, which is a function of the moisture content (θ). Matric potential is also a function of moisture content. The characteristic relationships between K, ψ_m, and θ must be defined in order to describe flow quantitatively.

Various methods are used to measure the potential gradients in the generalized flow equation. Tensiometer measurements are restricted to matric potentials between 0 and –0.08 MPa and generally are not operational in arid regions because the unsaturated zone is too dry. Thermocouple psychrometers measure water (matric and osmotic) potentials of less than –0.1 MPa (figs. 5 and

6). Temperature is measured by the chromel-constantan junction of the thermocouple psychrometers. Concentration or osmotic-potential gradients are calculated from chloride concentrations of the soil water according to the Vant Hoff equation (Campbell, 1985):

$$\psi_{\pi} = -(\upsilon \, C \, \chi \, R \, T) / 1000, \qquad (3)$$

where υ is the number of osmotically active particles (2 for NaCl),

C is the concentration (moles/kg),

χ is the osmotic coefficient (Robinson and Stokes, 1959),

R is the gas constant (8.3142 J mole^{-1} K^{-1}),

and T is the temperature (K).

Because thermocouple psychrometry forms an integral part of soil-physics monitoring in arid systems, principles of operation and potential sources of errors of psychrometers (Rawlins and Campbell, 1986) are presented below. Psychrometers consist of two junctions of dissimilar metals, chromel and constantan. The sensing junction serves as a wet bulb and equilibrates with the soil atmosphere through a metal screen cage, whereas the reference junction serves as a dry bulb, is in an insulated medium, and measures the ambient temperature. There are two basic types of psychrometers, the Spanner-type or Peltier-type psychrometer, which uses a cooling current (~ 5 ma for ~ 30 s) (the Peltier effect) to condense water below the dew point on the thermocouple (Spanner, 1951), and the Richards-type psychrometer in which a drop of water is added mechanically to the thermocouple. This water then evaporates into the atmosphere at a rate that depends on the relative humidity of the soil atmosphere. Evaporation of water decreases the temperature of the wet bulb, and this temperature depression is translated into output voltage. Initially the output voltage decreases rapidly and then stabilizes at a plateau value before final reduction to the reference voltage level. Drier soils result in higher microvolt output from the thermocouple, and the duration of the plateau is also much shorter. Both types of psychrometers measure the relative humidity (p/p_o) of the soil atmosphere, which is proportional to water (matric and osmotic) potential (ψ) according to the Kelvin equation

$$\psi = (RT / V_W) \ln (p/p_o) / 1000, \qquad (4)$$

where ψ is in MPa,

R is the ideal gas constant (8.3143 J °K^{-1} mol^{-1}),

V_w is the molar volume of water ($1.8 \times 10^{-5} m^3 mol^{-1}$),

and T is the temperature (°K).

The voltage used in water-potential calculations is the value obtained by extrapolation of the plateau value to the beginning of evaporation. Temperature gradients, whether in laboratory systems or near the soil surface, are critical because a 1°K temperature difference between the dry bulb and the sample at 20°C can result in a measurement error of 13 MPa (Rawlins and Campbell, 1986). Temperature gradients can be inferred in Spanner-type psychrometers from the null offset (Brown and Bartos, 1982). The null offset is the temperature difference between the reference and measuring junctions before Peltier cooling and should be zero under isothermal conditions. For example, a null offset of +60 μV indicates that the sensing junction is approximately 1°C cooler than the reference junction. Spanner-type psychrometers are used for field measurements; they operate in the range of –0.2 to –8 MPa because the Peltier effect cannot condense water at potentials of less than approximately –8 MPa. Richards-type psychrometers are generally restricted to laboratory use but can span a much larger range in water potential (–0.2 to –300 MPa) (Rawlins and Campbell, 1986).

Numerical Modeling

Because the monitoring period is relatively short compared with the life of a radioactive-waste-disposal facility, numerical models are required to evaluate long-term unsaturated-flow processes. Unfortunately, unsaturated flow in arid regions is extremely difficult to simulate numerically because of large variations in water potential and hydraulic conductivity within the flow field and because of the highly nonlinear relations between moisture content, water potential, and hydraulic conductivity. There are two basic types of unsaturated-flow codes, those that use moisture content (θ) as the dependent variable and those that use matric potential (ψ) as the dependent variable. The advantages of the θ-based formulation include (1) reduced numerical difficulty in simulating infiltration into very dry systems because θ varies less than ψ across the wetting front, (2) inherent ability to conserve mass, and (3) the fact that most studies monitor θ rather than ψ because θ is more easily measured (Hills and others, 1989b). The θ-based approach, however, cannot be used for simulating combined saturated and unsaturated or near-saturated flow (Hills and others, 1989b), and most publicly available θ-based codes cannot solve flow in layered soil systems. Traditionally, ψ-based codes have been favored for numerical simulation of unsaturated flow because ψ is a continuous physical quantity in space, whereas θ is discontinuous at lithologic contacts. Although ψ-based codes can solve variably saturated flow problems, infiltration into dry unsaturated zones is numerically difficult because ψ may vary by a few orders of magnitude across a wetting front. The degree of numerical difficulty increases as the initial water potentials decrease and as the applied moisture flux and sediment grain size increase because the resultant wetting front is steeper. Many of the available ψ-based codes, such as UNSAT2 (Davis and Neuman, 1983), TRUST (Narasimhan and others, 1978) and FEMWATER (Yeh and Ward, 1979) cannot solve the flow equation in very dry ($\psi \leq -1$ MPa) systems.

In order to validate numerical models, several computer codes have been used to simulate field infiltration experiments into a dry unsaturated zone in New Mexico (Hills and others, 1989a). These studies are part of the INTRAVAL (International Validation of Flow and Transport) program. The initial water potentials used in many of the simulations were much higher than those observed (–1 MPa at surface to –5 MPa at 5-m [16-ft] depth). Use of UNSAT2 in two-dimensional simulations of the infiltration experiment that have initial water potentials of –0.07 MPa resulted in as much as 50 percent mass balance error (Yabusaki, personal communication, 1990). Water potentials of –0.01 MPa were used as initial conditions in three-dimensional simulations of the experiment to reduce computational costs; however, sensitivity analyses were not conducted to evaluate the effect of varying initial conditions (Ababou, 1988). Although various techniques have been incorporated into VAM2D to improve its ability to converge in highly nonlinear flow problems, the lowest water potential reported in the literature as initial conditions was –1 MPa (Huyakorn and others, 1984). Many of the available ψ-based codes were used to simulate the test cases presented in this study; however, with the exception of TRACRN, these codes would not converge for many of the test cases simulated.

TRACRN

Details of the TRACRN code are provided in Travis and Birdsell (1990), and a summary of some of the important features are presented in this section. TRACRN uses a low-order (5-point operator), implicit finite difference approximation of the transient flow equation

$$\frac{\partial}{\partial t}(\phi\ \rho\ \sigma) + \nabla \cdot \left((-\rho \frac{\overline{k_r}\,\overline{k_s}}{\mu} (\nabla P + \rho\ \hat{g}) \right) = 0, \tag{5}$$

where ϕ is the porosity,

ρ is the fluid density,

σ is the saturation (volume of water / volume of voids),

$\overline{k_r}$ is the relative permeability,

$\overline{k_s}$ is the saturated permeability,

μ is the fluid viscosity,

P is the pressure, and

$\hat{g}$ is the gravitational acceleration (Travis and Birdsell, 1990).

The nonlinear differential equations are solved at each time step by means of the Newton-Raphson iterative scheme, which is more strongly convergent (second order) than the generally used Picard scheme (first order) and which enhances the ability of TRACRN to converge in dry conditions. An efficient preconditioned, conjugate-gradient method is used to solve the asymmetric matrices at each iteration. Two tolerance criteria must be satisfied for convergence: one for the Newton-Raphson iterations and the other for the matrix solver. These tolerance criteria generally result in a total mass balance that is accurate to one part in 10^6. An automatic time-stepping scheme based on the number of iterations is employed. Solution of highly nonlinear flow problems is sensitive to the time-stepping scheme because the time step may vary by many orders of magnitude.

METHODS

Field Techniques

Neutron thermalization was used to monitor moisture content, and psychrometers were used to monitor water potential (figs. 7a, 7b, and 8). The monitoring equipment was installed in the bed of an ephemeral stream because infiltration was expected to be greater there than in other geomorphic settings. Hydraulic conductivity was measured in areas characterized by different grain-size distributions. In addition to the field measurements, samples were collected from stream and interstream areas for laboratory measurements of moisture content, water potential, saturated hydraulic conductivity, and moisture-retention. Data on the boreholes drilled, monitoring equipment installed, and soil samples collected, have been compiled in table 1.

Moisture Content

Approximately 230 soil samples were collected from 10 boreholes (5 to 21 m [16 to 69 ft] deep; fig. 7a) for laboratory determination of gravimetric-moisture content. Most samples were obtained from the shallow (<15-m [<49-ft] depth), coarse-grained material of the Camp Rice Formation because of the difficulties of drilling into the deeper clay of the Fort Hancock Formation. Except for the deeper clays, the shallow material generally was not sufficiently cohesive to allow collection of undisturbed samples for volumetric moisture content and bulk density analyses; therefore, undisturbed samples were only collected from the upper 1.5 m (5 ft) of a study area that had been ponded for 15 hr. Bulk densities of the deeper clays were determined from core samples.

Moisture content was monitored by means of a Campbell Pacific Nuclear neutron moisture probe (Model 503 DR; CPN Corporation, Martinez, CA)). Two boreholes were drilled approximately 6 m (20 ft) apart with an air-rotary rig to install neutron-probe access tubes to depths of 21 and 41 m (69 and 135 ft) (figs. 7a, 7b, and 8). The boreholes were drilled with a drag bit (58-mm [2.3-inch] diameter) and a 60-kg (22-lb) hammer (Mullican and others, 1989). Because of drilling difficulties, steel drill pipe (70-mm [2.8-inch] O.D., 60-mm [2.4-inch] I.D.) was used instead of conventional aluminum access tubes. The access tube was driven with a 180-kg (67-lb) hammer and was advanced every 3 m (10 ft) to minimize drying of the overlying material during drilling. The annulus of the top 21 m (69 ft) of the deeper borehole was cemented for stability. To inhibit erosion during surface-water runoff and to prevent downward flow around the access tubes, cement was poured into a 1-m × 1-m (3-ft × 3-ft) area at the surface around the access tubes. Shallow (1.8 m [6 ft]), neutron-probe access tubes were also installed in boreholes drilled using a solid-stem auger (50-mm [2-inch] diameter).

The neutron probe was calibrated within both aluminum and steel access tubing by the manufacturer. These data show that approximately 50 percent more fast neutrons are attenuated through the steel than through the aluminum. Two neutron-probe access tubes were installed to 1.8-m (6-ft) depth in the field for further calibration of the neutron probe. One access tube was located in a plot that was ponded for an instantaneous-profile test (Hillel and others, 1972), and the other was offset by approximately 10 m (33 ft) in an adjacent dry area. Neutron counts were recorded at approximately 0.1-m (0.3-ft) intervals from depths of 0.3 to 1.2 m (1 to 4 ft). Soil samples were collected adjacent to the access tubes in brass cylinders (54-mm [2.1-inch] diameter, 60-mm [2.4-inch] length) using a double-cylinder, hammer-driven core sampler (Soil Moisture Equipment, Incorporated, Santa Barbara, CA). These samples were obtained from the same depths as those that were logged with the neutron probe. The samples were weighed in the field and analyzed for volumetric moisture content in the laboratory using standard methods. Because neutron-count ratios (neutron counts/standard counts) may introduce more uncertainty into moisture-content measurements than the natural drift of the count rate (Hudson and Wierenga, 1988), neutron counts were used in the calibration equation. The calibration curve was calculated by least squares linear regression of the volumetric moisture content and neutron counts

$$\theta = -6.4674 + 0.003912\ \mathrm{Cn}, \tag{6}$$

where θ is the volumetric moisture content and Cn is the neutron count/min (fig. 9). The calibration equation had a coefficient of determination (r^2) of 0.98 and a standard error of estimate of 1.2 $m^3\ m^{-3}$ (1.2 $ft^3\ ft^{-3}$). Moisture content was monitored monthly. The deep-access tubes were logged at 0.3-m (1-ft) intervals from 0.3- to 3-m (1- to 10-ft) depth and at 1-m (3-ft) intervals to a depth of 41 m (135 ft). Moisture content also was monitored monthly in the shallow-access tubes at 0.1-m (0.3-ft) intervals from 0.3- to 1.6-m (1- to 5-ft) depth.

Water Potential

Tensiometers, used to measure matric potential, were obtained from Soil Measurement Systems (Tuscon, AZ). Each tensiometer consisted of a plastic tube that had a porous ceramic cup at one end and a septum stopper at the other. Tensiometers were installed using a hollow-stem pipe (25-mm [1-inch] diameter) that was pushed into the ground by means of a drill rig. In order to provide a good contact between the tensiometer cup and the surrounding sediments, a slurry made of sieved sediment from the boreholes was poured along the outside of the tensiometer. A tensimeter, which is a hand-held pressure transducer having a digital readout (sensitivity = 1×10^{-4} MPa), was calibrated by the manufacturers against a hanging water column and was used to measure matric potential in the tensiometers (Marthaler and others, 1983). Tensiometers installed at depths of 0.9, 1.5, and 1.8 m (3, 5, and 6 ft) (figs. 7a, 7b, and 8) to monitor natural potentials were not operational because the matric potential was less than the operating range (<-0.08 MPa). However, areas ponded for unsaturated hydraulic conductivity measurements had matric potentials within the range measured by tensiometers.

Field psychrometers consisted of screen-caged, thermocouple psychrometers (Model PST 66; Wescor, Incorporated, Logan, UT) (fig. 5). To install psychrometers at shallow depths, a pit was dug to 1.4 m (4.6 ft) and psychrometers were placed into holes (13-mm [0.5-inch] diameter, 0.5-m [1.6-ft] length) drilled horizontally into the pit wall. This procedure ensured that the material overlying the psychrometers was undisturbed and that a good contact existed between the psychrometers and the surrounding sediments. Because the psychrometers were not retrievable, they were installed in duplicate for data verification at a depth of 0.3 m (1 ft) and at 0.3-m (1-ft) intervals between depths of 0.5 m (1.6 ft) and 1.4 m (4.6 ft). The psychrometers were placed so that their symmetry axis was perpendicular to temperature gradients to minimize the effect of such gradients on psychrometer output (Rawlins and Campbell, 1986). After these holes were sealed with sediment from the pit, the pit was backfilled with the original sediments.

At greater depths, duplicate psychrometers were installed in a borehole that was drilled to a depth of 14.5 m (48 ft) using a solid-stem auger (50-mm [2-inch] diameter) (figs. 8 and 10). Wetting or drying of native material was expected to be minimal because no drilling fluid was used. For protection during installation, the psychrometers were emplaced in a PVC screen that was filled with commercial (Ottawa) sand (0.1- to 0.4-mm [0.3- to 1.57-inch] grain size). Borehole cuttings below a 6-m (20-ft) depth were used to backfill immediately around the psychrometers, and because cuttings from above a 6-m (20-ft) depth were too coarse, commercial Ottawa sand was used. Epoxy (DER324/DEH24, Dow Chemical Company) was used to prevent preferential water or air flow between psychrometer stations within the borehole and to form a seal at the surface that would preclude surface drainage into the borehole. Epoxy also was chosen because it does not introduce water into the system. Epoxy properties (curing time, viscosity, and exothermic curing temperature) were tested in the laboratory before field use to ensure that the epoxy would not become viscous while being poured down the tremie pipe nor emit too much heat to the surroundings. Sand was poured down a separate tremie pipe immediately after the epoxy to form a sand/epoxy column that reduced the reaction temperature to 80°C. The small diameter of the borehole and use of sieved natural materials as a backfill were designed to minimize psychrometer equilibration time. The psychrometers were connected to a data logger (Model CR7; Campbell Scientific, Incorporated, Logan, UT) that was powered by a solar panel and a rechargeable internal battery, backed up by an external marine-type battery. Water potentials and temperatures were logged daily at 0900 hr. Hourly data were recorded for 1 to 4 d each month, and all data were downloaded monthly.

In addition to the use of tensiometers and psychrometers for monitoring water potential, approximately 200 soil samples were collected from 13 boreholes (0.3 to 20 m [1 to 66 ft]) for water-potential (matric and osmotic) measurements in the laboratory (figs. 7a, 7b, and 8). The shallow holes (≤1 m [≤3.3 ft]) were sampled manually by pushing a shelby tube (0.2-m [0.7-ft] diameter) into the ground; the deeper boreholes were drilled using a hollow-stem auger, and samples also were collected in shelby tubes. The samples were transferred in the field to mason jars and their lids sealed with paraffin to minimize moisture loss.

Hydraulic Conductivity

Saturated Hydraulic Conductivity

Field-saturated hydraulic conductivity (K_{fs}) was measured by means of a Guelph permeameter, which has a measurement range of 10^{-4} to 10^{-8} m s^{-1} (Reynolds and Elrick, 1985; Reynolds and Elrick, 1986). Field-saturated hydraulic conductivity is determined from the Guelph permeameter by applying an equation for steady-state flow from a cylindrical test hole,

$$2\,\pi\,H^2\,K_{fs} + C\,\pi\,a^2\,K_{fs} + 2\,\pi\,H\,\phi_m = C\,Q, \tag{7}$$

where H (m) is the steady-state depth of water in the test hole,

C is a dimensionless proportionality constant primarily dependent on H a^{-1},

a is the radius of the test hole,

ϕ_m (m s^{-1}) is the matric flux potential, and

Q (m^3 s^{-1}) is the steady-state flow rate out of the test hole (Reynolds and Elrick, 1985).

The matric flux potential, ϕ_m, is

$$\phi_m = \int_{\psi_i}^{0} K(\psi)\, d\psi, \tag{8}$$

where ψ is the initial matric potential in the soil and $K(\psi)$ is the hydraulic conductivity/matric potential relationship for infiltration (Reynolds and Elrick, 1985). The three terms in the left-hand side of equation 7 represent water flow resulting from pressure potential, gravitational potential, and matric potential, respectively. The first two terms combined yield the field-saturated flow component, and the third term represents the unsaturated-flow component. The Richards equation was used to solve for K_{fs} by means of the simultaneous equations approach when two head measurements were made (Reynolds and Elrick, 1985):

$$K_{fs} = G_2\, Q_2 - G_1\, Q_1, \tag{9}$$

where

$$G_1 = G_2 \left[\frac{H_2 C_1}{H_1 C_2}\right]$$

$$G_2 = \frac{H_1\, C_2}{\pi\left[2H_1\, H_2\, (H_2 - H_1) + a^2\, (H_1\, C_2 - H_2\, C_1)\right]} .$$

In contrast to the Richards analysis, the LaPlace analysis for K_{fs}, which only requires one head measurement, solves the equation

$$2\, \pi\, H^2\, (K_{fs})^l + C\, \pi\, a^2\, (K_{fs})^l = CQ\, , \tag{10}$$

in which capillarity is ignored and, therefore, $(K_{fs})^l$ is a maximum estimate of the K_{fs} (Reynolds and Elrick, 1985). The Glover analysis of K_{fs} is identical to the LaPlace analysis and was used for comparison with the Richards analysis. The Glover equation (Amoozegar and Warrick, 1986),

$$(K_{fs})^g = Q\left[\sinh^{-1}\left(\frac{H}{a}\right) - \sqrt{\frac{a^2}{H^2} + 1} + \frac{a}{H}\right] / \left(2\pi H^2\right), \tag{11}$$

was solved with the use of the identity

$$\sinh^{-1}(x) = \ln\left[\, x + \sqrt{x^2 + 1}\,\right] .$$

A total of 20 conductivity tests were performed in three different areas characterized by different soil textures to evaluate the relationship between conductivity and grain size. The permeameter was placed in cylindrical test holes that had radii of 0.03 m (0.12 ft) that were augered to 0.15 m (0.5 ft). A constant water depth (0.05 m [0.16 ft] $\leq H \leq$0.25 m [0.82 ft]) was maintained in the test hole, and the water flux into the soil was monitored until steady-state outflow was attained, which indicated soil saturation. The water depth was set by adjusting the height of the air-inlet tube. The rate of water-level decline was recorded at 1-min intervals until five consecutive readings of the same rate of water-level decline were recorded.

Unsaturated Hydraulic Conductivity

Under field conditions, the instantaneous-profile method was used to measure the field relationship between hydraulic conductivity and moisture content and between matric potential and moisture content in the wet range (Rose and others, 1965; Hillel and others, 1972) (figs. 7a and 7b). A level, vegetation-free, 4-m^2 (43-ft^2) area was chosen for the test. A trench was dug around the test plot, and wooden boards and plastic sheets were used to isolate the plot from the surrounding sediments. In the center of the plot, a neutron-probe access tube was installed to monitor moisture content to a depth of 1.6 m (5.3 ft). A total of 20 tensiometers were installed; 4 tensiometers were installed at 0.3-m (1-ft) intervals to a total depth of 1.5 m (5 ft) at 5 locations. A hand drill was used in the top 0.6 m (2 ft), and a hollow steel pipe was used to install the deeper tensiometers. The boreholes were larger than the diameters of the tensiometers and were backfilled with a slurry of sieved native material; bentonite was placed in the annulus to prevent downward leakage of water around the tensiometer. The plot was flooded for 26 hr with an average ponding head of 0.4 m (1.3 ft). After cessation of ponding, the plot was covered with plastic sheets and soil to minimize evaporation, and infiltration was estimated from the rate of decline of the ponded water. Moisture content (0.1-m [0.3-ft] intervals) and matric potential (0.3-m [1-ft] intervals) were measured during ponding and drainage.

The data were analyzed to calculate unsaturated hydraulic conductivity. The governing equation for flow is obtained by substitution of the conservation of momentum equation (12a) into the conservation of mass equation (12c):

$$q_z = -K_z \frac{\partial \Phi}{\partial z} = K_z + K_z \frac{\partial \psi_m}{\partial z}, \qquad (12a)$$

where $$\Phi = \psi_m - z\,, \qquad (12b)$$

$$\int_{t1}^{t2} (-q_z)\, dt = \int_{t1}^{t2} \int_{z1}^{z2} dz\, dt, \text{ and} \qquad (12c)$$

$$K_2 = \left\{ \int_{1}^{t2} \left(- \int_{z1}^{z2} \frac{\partial \theta}{\partial t} dz \right) dt \right\} / \left\{ \left(\frac{\partial \Phi}{\partial z} + 1 \right)_z T \right\}, \text{ and} \qquad (12d)$$

where q_z is the vertical water flux at depth z,

Φ is the hydraulic head (the sum of the matric [ψ_m] and gravitational potential [z, depth below land surface]),

K_z is the local average unsaturated hydraulic conductivity across the depth interval, and

T is the time between t1 and t2 (Rose and others, 1965).

K_z was calculated at four depths and corresponds to moisture content and matric potential between the two successive moisture- or matric-potential profiles that include the depth z. In heterogenous soils, the calculated hydraulic conductivity may be negative because of hydraulic conductivity differences at soil boundaries. This limitation was eliminated by setting z1 equal to 0 (the land surface) in all calculations (Rose and others, 1965). Because barometric pressure and temperature effects on matric-potential measurements resulted in negative gradients during some time intervals, a 5-point moving average algorithm was used to smooth the data.

Laboratory Methods

Water Potential

Water potential was measured in the laboratory with a Decagon psychrometer SC-10 sample changer (Decagon Devices, Incorporated, Pullman, WA) (fig. 6) that was calibrated using NaCl solutions of known osmotic potential (ψ_π). (Osmotic potentials for certain molalities and certain temperatures are listed in Lang [1967]). NaCl solutions were prepared according to procedures outlined in Brown and van Haveren (1972), the solutions ranging in concentration from 0.05 M to saturated and corresponding to osmotic potentials of –0.2 to –38 MPa at 20°C. The 1-s readings were recorded by a data logger (Model Terra 8×, Terrascience Systems, Limited, Vancouver, Canada) for a period of 120 s. Typical psychrometric output during evaporation shows that the plateau is stable. Next, the 2-min microvolt output reading was used to calculate water potential. A set of 20 calibration solutions were prepared and measured initially to test the instrument, and the resulting regression line gave r^2 of 1.0 and a standard error of estimate of 0.06 MPa (fig. 11). Because water potentials from –0.01 to –10 MPa correspond to relative humidities from 93 to 100 percent, all measurements were conducted in a glove box lined with wet paper towels to minimize moisture loss from the samples. Temperature variations in the laboratory were minimal. During routine analyses, a set of six samples were placed in the sample changer (fig. 6); after 30 min of temperature- and vapor-pressure equilibration, the output was scanned to determine what bracketing standards should be run with the samples. The standards were then placed in the chamber and after another 30-min equilibration period, the samples and standards were measured. Least squares linear regression was used to calculate the sample water potential. Different equilibration times were also tested by analyzing a set of six samples at 1, 1.5, and 2.5 hr; mean psychrometer output (–8.9 MPa) was not affected by variations between 1 and 2.5 hr.

Erratic readings or nonconcurrence of the two sets of standard-count readings indicated that the SC-10 sample changer occasionally malfunctioned. The first step taken was to clean the thermocouple psychrometer and thermocouple mount with distilled deionized water and then to dry the units with canned compressed air. If these steps were unsuccessful, the thermocouple was replaced and the samples reanalyzed.

Field psychrometers were calibrated in the laboratory at five different water potentials and at three different temperatures before installation (table 2). Calibration procedures similar to those outlined in Brown and Bartos (1982) were followed. A Tronac refrigerated water bath (Model # PTC 41; Tronac, Incorporated, Orem, UT) equipped with a temperature control of 1×10^{-4}°C standard deviation was used to provide a constant temperature environment. The temperature of the water bath was recorded with thermistors, thermocouple psychrometers, and a mercury thermometer. Typical psychrometer response during evaporation at different water potentials indicated that the plateau value decreased and that the duration of the plateau increased with increasing (less negative) water potential (fig. 12). Because psychrometer output may correspond to two different water potentials, at least 60 readings were recorded for each psychrometer to distinguish between readings in the dry and wet ranges. Psychrometer readings are dependent on the magnitude and duration of the cooling current. A Peltier cooling current of 5 milliamps (ma) and a 30-s cooling time are considered optimal (Brown and Bartos, 1982). Higher cooling currents cause adverse effects associated with heating of thermocouple wires. Shorter cooling times result in less precise water-potential measurements, whereas longer cooling times do not extend the range of psychrometers more than 0.5 MPa and, therefore, are not considered advantageous. Condensation time, cooling current, and voltage-endpoint determination were kept constant during calibration and field measurement of water potential. Approximately 1 m (3 ft) of lead wire was submerged in the water bath during calibration to minimize heat conduction along the wires. Psychrometers were calibrated with the required cable lengths for field installation. Because the psychrometer lead wires were of different lengths, different cooling voltages were applied to obtain a 5-ma cooling current at the psychrometer tip. The required cooling currents were measured with an ampmeter. As many as four psychrometers having similar lead-wire lengths were attached to each interface in the CR7 data logger because only one cooling current could be applied to each interface. In most cases, four psychrometers were attached to each interface, which resulted in a minimum time interval of 1.2 s between readings. Psychrometer output was recorded every hour by the data logger during calibration. Temperature equilibration was indicated by the null offset and was usually attained within 1 hr. Vapor-pressure equilibration was reached when similar consecutive hourly readings were recorded.

The psychrometers were suspended initially in test tubes filled with NaCl solution. Various materials, including beeswax and parafilm, were used to seal the thermocouple wires to the lid of the test tubes. Some of the psychrometers showed a slow decline in microvolt output during calibration, whereas others recorded a marked drop to zero within 1 hr. These output reductions were attributed to leakage through psychrometer screens, although screen cages were designed to prevent water movement into the psychrometer. Final calibrations were conducted in a sample chamber made of Swagelock copper fittings similar to those described in Brown and Bartos (1982) and using Whatman 1 filter paper saturated with NaCl solutions. Psychrometers were cleaned in warm soapy water between immersions in different molality solutions. The mean calibration curve calculated for 24 psychrometers at 15, 20, and 25°C is shown in figure 13.

Saturated Hydraulic Conductivity

Saturated hydraulic conductivity was measured in the laboratory on five undisturbed soil cores according to a procedure modified from Elrick and others (1981). The soil samples were collected in brass cylinders using a core sampler at several locations in the study area (figs. 7a and 7b). A nylon screen and filter paper were used to contain the soil on the bottom, and a retaining ring that had a rubber seal and a hose clamp were attached at the top. The samples were placed in a plexiglass tank that was filled slowly (300 mL hr^{-1}) with tap water to saturate the cores. Once saturated, a rubber stopper that contained an outflow tube was placed on the cylinder, and the tank was filled to the level of the overflow tube. The outflow from the cylinder was recorded every 15 min until three consecutive readings agreed within one order of magnitude.

Soil Texture, Moisture Content, Bulk Density, and Porosity

Particle-size analyses were conducted on approximately 100 soil samples at the University of Wisconsin. The samples were ground initially to disaggregate calichified material. The >2-mm fraction was determined by sieve analysis, and the percent sand, silt, and clay were determined by hydrometer analysis (Bouyoucos, 1962). Gravimetric- and volumetric-moisture content was determined by weighing and oven drying the samples at 105°C at 24-hr intervals until the weight change was less than 5 percent. Bulk density was calculated by dividing the weight of the oven-dried sample by the sample volume. Porosity (n) was calculated from the bulk density (ρ_b) data thus:

$$n = 1 - \rho_b / \rho_s. \tag{13}$$

A particle density (ρ_s) of 2.65 kg m^{-3} was assumed.

Moisture-Retention Curves

Soil-moisture-retention curves were determined in the laboratory using many different techniques (Klute, 1986) to cover the range in observed water potential. The main drying (desorption) curve was measured by means of Tempe pressure cells (0.0 to –0.1 MPa), pressure-plate extractors (–0.1 to –1.5 MPa), and a thermocouple psychrometer sample changer (–0.2 to –10 MPa). Hysteresis was ignored. Data on the retention curve were obtained by allowing saturated soil samples to drain until equilibrium was reached by means of the applied pressure and then determining the corresponding moisture content by oven drying. Undisturbed cores that had already been saturated for hydraulic conductivity tests were placed in the Tempe cells in order to measure matric potential using 0.05 and 0.1 MPa pressures plates. Pressures of 0.02, 0.05, 0.07, and 1.0 MPa were applied using nitrogen gas.

Soil cores that had been saturated for hydraulic conductivity measurements were used in the Tempe cells. Coarse-grained material was not sufficiently cohesive for use in the Tempe cells. Disturbed material was used for retention curves below –0.1 MPa. This situation was satisfactory because most of the water is adsorbed on the grain surfaces at these matric potentials and soil structure is not important (Papendick and Campbell, 1980). For samples that contained gravel, the less-than-2-mm [.07-inch] size fraction was used for the retention curves, and the resultant moisture content was corrected for the percentage gravel, assuming that the gravel contained no moisture (Nichols, 1987). Soil samples were saturated on the pressure plates in a water tank by allowing water to rise for approximately 1 d. A paste was made of finely ground soil to ensure a good contact between the soil and the pressure plate. Pressures of 0.15, 0.3, 0.4, 0.5, 0.75, 1.0, and 1.5 MPa were applied, and 0.5- and 1.5-MPa pressure plates were used. Equilibration times ranged from 1 to 7 d, depending on the pressure. The retention curves were extended beyond –1.5 MPa by air-drying the samples and measuring water potential with a laboratory thermocouple psychrometer at various intervals. Although the psychrometer measures matric and osmotic potentials and the pressure plate measures matric potentials only, chloride-concentration data from soils at the site indicate that the osmotic potential is negligible and that water potential estimated from psychrometers using equation 4 is essentially the same as the matric potential.

Numerical Modeling

Input data required for the numerical simulations include information on the constitutive relations between moisture content and water potential and between moisture content and hydraulic conductivity. The following analytical function was used to describe the θ/ψ relationship (Van Genuchten, 1980):

$$\theta = \theta_r + \frac{\theta_s - \theta_r}{[1 + (\alpha\,\psi)^n\,]^m}, \tag{14}$$

where θ_r is the residual water content,

θ_s is the saturated water content,

ψ is the matric potential, and

α, n, and m are empirical parameters.

The computer program RETC (Van Genuchten, 1985) was used to obtain estimates of the fitting parameters (θ_r, θ_s, α, and n). The following objective function (E) is minimized in the program

$$E(b) = \sum_{i=1}^{N} \left\{ w_i \left[\theta_i - \hat{\theta}_i (b) \right] \right\}^2 , \tag{15}$$

where b is the trial parameter vector representing the unknown coefficients (θ_r, θ_s, α, and n),

N is the number of retention data, and

θ_i and θ_i are the observed and fitted water contents.

RETC uses a least squares optimization process based on Marquadt's maximum-neighborhood method (Marquadt, 1963). The unsaturated hydraulic conductivity was estimated from the fitted soil-water-retention curves and the measured Ks data using Mualem's model (Mualem, 1976) and by restricting m to 1–1/n (Van Genuchten, 1980):

$$K_u(\psi) = \left(\frac{\{1 + (\alpha\, \psi)^{n-1} \, [1 + (\alpha\, \psi)^n]^{-m}\}^2}{[1 + (\alpha\, \psi)^n]^{m/2}} \right) K_s \, . \tag{16}$$

RESULTS

Soil Texture and Moisture Content

The shallow (≤15 m [≤49 ft]), coarse-grained material (Camp Rice Formation) generally contains 50 to 60 percent sand and 10 to 20 percent silt and clay; however, some zones contain as much as 60 percent gravel. Sediment samples that contained gravel were classified according to Folk (1974), and those that did not contain gravel were classified according to the U.S. Department of Agriculture (1975). The predominant texture of the shallow material ranges from sandy-clay loam to sandy loam, whereas the deeper material penetrated by boreholes 18, 30, 50, and 74 consists of clay (table 1).

Volumetric moisture content monitored with the neutron probe ranged from 0 to 0.32 $m^3\ m^{-3}$ (0 to 0.32 $ft^3\ ft^{-3}$) (figs. 14 and 15a through d). Differences in soil moisture with depth corresponded to variations in sediment grain size. Moisture content of the shallow (15 m [49 ft]), coarse-grained deposits was low (0 to 0.18 $m^3\ m^{-3}$ [0 to 0.18 $ft^3\ ft^{-3}$]), whereas that in the deeper clays was much higher (as much as 0.32 $m^3\ m^{-3}$ [0 to 0.32 $ft^3\ ft^{-3}$]). The lowest moisture content was recorded in access tube 71 where the sediments are coarsest (fig. 15d). Unrealistically low moisture contents in this access tube were attributed in part to the standard error associated with the neutron-probe calibration curve (±1 $m^3\ m^{-3}$ [±1 $ft^3\ ft^{-3}$]) and may also result from the inapplicability of this curve, which was developed for finer grained material.

Volumetric moisture contents of samples collected in a nearby borehole (74) ranged from 0.02 to 0.33 $m^3\ m^{-3}$ (0.02 to 0.33 $ft^3\ ft^{-3}$) (fig. 16r). The contrast in moisture content at the contact between the shallow, coarse-grained material and deeper clay is most apparent in neutron access tube 71 where moisture content increases from 0 to 27 $m^3\ m^{-3}$ (0 to 27 $ft^3\ ft^{-3}$) in 2 m (6.6 ft) (fig. 16d). Coarse-grained interbeds within the deeper clay also have low moisture content (0.01 to 0.07 $m^3\ m^{-3}$ [0.01 to 0.07 $ft^3\ ft^{-3}$]). Porosities of surficial sediments calculated from bulk densities ranged from 40 to 56 percent and indicate a 10- to 20-percent saturation. Porosities of the deeper clays ranged from 26 to 36 percent and average 31 percent. On the basis of these porosity data, moisture content of the deep clays is close to saturation. The range in moisture contents of closely spaced access tubes (61 and 62) was similar (figs. 7a, 7b, and 15a and b). Volumetric moisture content, which was determined from soil samples collected predominantly from the shallow, coarse-grained material, ranged from 0.01 to 0.33 $m^3\ m^{-3}$ (0.01 to 0.33 $ft^3\ ft^{-3}$) (figs. 16a through t and 17a through i).

With the exception of access tube 61, monthly monitoring showed that, within the detection limits of the neutron probe, moisture content remained constant with time from 0.3 to 41 m (1 to 135 ft) (figs. 14 and 15a through d). Variations in moisture content were recorded to a depth of

0.7 m (2.3 ft) in access tube 61, which is located in an ephemeral pond (fig. 15a). The shallowest depth monitored by the neutron probe was 0.3 m (1 ft); however, moisture contents as much as 0.26 m^3 m^{-3} (0.26 ft^3 ft^{-3}) were measured down to 0.3 m (1 ft) after a rainfall event (borehole 50, fig. 16p).

Water Potential

Results from laboratory psychrometric measurements of samples show that water potential generally increased with depth except in the shallow subsurface after rainfall events (figs. 16a through t and 17a through i; app.). Although water potential measured by psychrometers is the sum of matric and osmotic potential, psychrometers at this site essentially measured the matric potential because the osmotic potentials were negligible (<–0.8 MPa). Total potentials (matric + osmotic + gravitational) generally are used to indicate the direction of water flow. Under the dry conditions at this study area, however, gravitational potentials were small (<1.5 MPa) relative to the water potential (matric + osmotic); therefore, water potentials, which ranged from –0.1 to –15.6 MPa, approximated total potential and were used to estimate water-flow directions.

The highest water potentials were measured in the top 1 m (3 ft) of soil after rainfall, and the lowest water potentials were measured at shallow depths after dry periods. After a dry period in the summer, water potentials ranged from –15.6 MPa in near-surface samples to –4.5 MPa in samples collected at 9 m (30 ft) (borehole 21, fig. 16f). The hydraulic gradient was steepest near the surface, approximately –5 MPa m^{-1}. Similar water potentials were recorded in samples from other areas (boreholes 41: –3 to –12 MPa; borehole 15: –1 to –12 MPa; borehole 74: –3 to –12 MPa). After a rainfall event, near-surface water potentials were close to 0 MPa and decreased to –12 MPa within a 1.5-m (5-ft) depth (borehole 15, fig. 16c). In order to examine the hydraulic gradient near a wetting front in detail, samples were collected at 0.05-m (0.16-ft) intervals from borehole 41C (fig. 16l). A decrease in water potential from –0.1 to –13.2 MPa within a 0.05-m (0.16-ft) interval indicated that the wetting front was sharp. The lowest water potential recorded at depth (<5 m

[<16.4 ft]) was –2 MPa. Water potentials of samples collected in the winter (boreholes 30: –2 to –8 MPa; 31: –3 to –7 MPa; and 54: –3 to –8 MPa) were generally higher and had a smaller range than those measured in the summer (fig. 17a through i). Smaller sampling intervals in borehole 56 showed that the water-potential gradient is steeper and the low water-potential zone is narrower and closer to land surface in the winter than in the summer.

The shallow in situ psychrometers (≤1.4-m [≤4.6-ft] depth), which were installed in a pit in close contact with the surrounding sediments, equilibrated within a day of installation, whereas the deeper borehole psychrometers (2.7- to 14.3-m [8.9- to 47-ft] depth) required approximately 20 d to equilibrate (fig. 18). Water potentials increased during equilibration because the backfill sediments that dried while being stored during drilling recovered moisture from subsurface sediment after installation. The rate of equilibration decreased with time. After equilibration, water potentials measured by psychrometer pairs generally agreed within 0.2 MPa during the first 200 d, which signified that the water potentials were reliable during this period. After this time, readings from 7 of the 19 psychrometers drifted, and examination of the psychrometer evaporation curves indicated that some of the psychrometers had become contaminated with NaCl. Water potentials measured by psychrometers from 0.3 to 0.8 m (1 to 2.6 ft) decreased gradually during the monitoring period and went out of range (<–7 to –8 MPa) during May through September 1989 because the system became too dry and stayed out of range during the remainder of the monitoring period.

Psychrometers at depths greater than 2.5 m (8.2 ft) did not exhibit long-term variations in water potential, whereas those at shallower depths showed a reduction in water potential during the monitoring period. Diurnal variations in water potential were restricted to the psychrometers at a depth of 0.3 m (1 ft). These variations, however, are interpreted as an artifact of temperature variations and temperature gradients (indicated by the null offset) in the shallow zone (fig. 19) and do not reflect water movement. As in the laboratory psychrometric measurements, vertical profiles show that water potentials increased with depth (fig. 20). The water-potential gradient was steepest in the upper 3 m (10 ft) and became steeper with time at shallow depths.

Temperature

Temperature oscillations over time were most pronounced in the shallow zone and decreased with depth (fig. 21). Hourly variations in temperature were primarily restricted to psychrometers at 0.3 m (1 ft) (fig. 22). Temperature variations at this depth lagged surface temperature variations by approximately 12 hr. The vertical distribution of temperatures showed that temperature gradients were steepest in the upper 5 m (16.4 ft) and were near zero below this depth (fig. 23a and b). The temperature decreased with depth in the summer (early April to late September, Julian days 90 to 275) and increased with depth in the winter. Temperature gradients were steepest in midsummer (Julian day 200) and midwinter (Julian day 350). Temperatures ranged from 20 °C below a depth of 5 m to 30 °C at a 0.3-m (1-ft) depth in midsummer and to 7°C at a 0.3-m (1-ft) depth in midwinter. During the summer, temperature gradients oppose water-potential gradients, whereas during the winter both temperature- and water-potential gradients are in the same direction (fig. 24a and b).

Hydraulic Conductivity

The rate of water percolation for the field-saturated hydraulic conductivity tests ranged from 1×10^{-6} to 8×10^{-7} m^3 s^{-1} (3.5×10^{-5} to 2.8×10^{-5} ft^3 s^{-1}) (table 3). Steady-state outflow was generally attained within 30 min. Use of the Richards analysis resulted in some negative values of K_{fs}; this result is attributed to the fact that equation 9 is not well conditioned (that is, the K_{fs} solution is dependent on the ratio of Q_2 to Q_1; Elrick and others, 1988). There is no systematic difference between K_{fs} data based on the Richards analysis and those from the Glover analysis, even though the latter would be expected to be higher because capillarity is ignored in the Glover analysis. Laboratory-measured saturated hydraulic conductivities ranged from 1.6×10^{-8} to 1.7×10^{-4} m s^{-1} (5.2×10^{-8} to 5.6×10^{-4} ft s^{-1}) (table 4).

Downward movement of a sharp wetting front was recorded during the ponding phase of the instantaneous-profile test (fig. 25). The infiltration rate was approximately 20 times greater than the drainage rate because the hydraulic-head gradient was much higher during the wetting phase (figs. 25 and 26). Water contents and water potentials monitored during the instantaneous-profile test were much higher than those recorded in the natural system. As expected for gravitational flow, the hydraulic-head gradient was close to unity throughout drainage (fig. 27).

With the exception of data from a 1.05-m (3.3-ft) depth, water-retention curves for the other three depth intervals were similar (fig. 28). Calculated unsaturated hydraulic conductivities at 0.45 m (1.5 ft) and 0.75 m (2.5 ft) were similar and ranged from 9×10^{-7} m s^{-1} (3×10^{-6} ft s^{-1}) at a water content of 0.32 m^3 m^{-3} (0.32 ft^3 ft^{-3}), to 2×10^{-8} m s^{-1} (6.6×10^{-8} ft s^{-1}) at a water content of 0.27 m^3 m^{-3} (0.27 ft^3 ft^{-3}) (fig. 29). Hydraulic conductivities for the 1.05-m-depth (3.4-ft) interval are approximately one order of magnitude higher than those calculated for the other layers. Although the hydraulic conductivity/matric potential relationship exhibited a high degree of variability (as much as two orders of magnitude variation in K_u for a given water potential), this relationship showed no systematic variation with depth (fig. 30). The field-saturated hydraulic conductivity, calculated from the infiltration rate of the water after cessation of ponding, was 8.9×10^{-6} m s^{-1} (2.9×10^{-5} ft s^{-1}) and was within the range of saturated hydraulic conductivities measured nearby using the Guelph permeameter (1×10^{-5} to 3×10^{-6} m s^{-1} [3×10^{-5} to 10×10^{-5} ft s^{-1}]).

Numerical Modeling

Numerical simulations were used to analyze unsaturated-flow processes at the principal study area and to examine various pathways for waste migration from a possible facility. Three basic test problems were considered. Test problem 1 was used to evaluate upward flow, which is suggested by the observed water-potential data. Infiltration at the land surface and leakage from the base of a facility were considered in test problem 2. Both of these problems focused on the upper 15 m

(49.2 ft) of the unsaturated zone (Camp Rice Formation) because water-potential data were available from this section. Because the water-potential data indicated upward flow, much of the infiltrated water would be expected to move back to the surface. The effect of lithologic heterogeneities on flow directions was also examined. Test problem 3 evaluated the hydrologic effect of the contact between shallow coarse-grained material and deeper fine-grained material, which corresponds to the contact between the Camp Rice and Fort Hancock Formations. The main purpose of this test problem was to evaluate the potential for development of perched conditions at the contact and to assess the likelihood that leakage from a facility would migrate along the contact and discharge in nearby arroyos. The computer code, TRACRN, was implemented on a DEC VAX 3100 station that had double precision (64 bit words). The required CPU time ranged from on the order of minutes in the one-dimensional simulations to as much as 8 hr in the two-dimensional simulations.

Test Problem 1

One-dimensional, upward flow was simulated by means of TRACRN to evaluate observed water-potential variations. Upward flow is an easier problem to solve than infiltration, from a computational point of view. The soil-layering configuration for the model was based on grain-size analyses from borehole 50 located adjacent to the in situ psychrometers (fig. 31a). Material properties were assigned on the basis of laboratory-retention data for similar soil textures (fig. 32; table 5). When RETC was used to obtain parameters (θ_r, θ_s, α, and n) to fit van Genuchten's analytic function (eq. 14) to the retention data, unrealistic values of saturated- (θ_s) and residual- (θ_r) water content were obtained; therefore, these parameters were fixed at more appropriate values. Saturated-water content was estimated from bulk-density data according to equation 13. The residual-water content was fixed at a value slightly lower than the lowest recorded water-content value. The spatial discretization of the grid ranged from 0.05 m (0.16 ft) in the upper 5 m (16 ft) to 0.1 m (0.3 ft) in the lower 10 m (33 ft) (table 6). Initial conditions for the simulation consisted of water potentials measured by the in situ psychrometers on Julian day 117 (–2 to –7 MPa), which were linearly interpolated to obtain water-potential values for the grid nodes (fig. 31b). Water potentials from Julian day 117 were chosen because these data represent relatively wet initial conditions. The corresponding moisture-content profile shows large discontinuities at the various sediment interfaces, which indicates that moisture content is unsuitable for determination of water-flow directions (fig. 31c). Upward flow was imposed by applying a constant water-potential- (Dirichlet) boundary condition of –10 MPa at the surface. The bottom boundary was constant water potential at ambient conditions (–2 MPa). The simulation time of 1,000 yr was used to ensure that equilibrium with the upper boundary condition was reached.

Most of the water movement was restricted to the upper 0.4 m (1.3 ft) of the unsaturated zone (fig. 33). The cumulative water movement out of the system was 2.5 mm (0.1 inch). The maximum water-content change during the simulation was 1 percent and shows that water content is not a very sensitive indicator of water movement in arid systems. These data suggest that a small change in water content can cause large variations in water potential in dry unsaturated zones. The reverse is also true in that only a small influx of water would be required to reduce the water potentials.

Test Problem 2

The second test problem evaluated infiltration into the dry unsaturated zone and was used to assess the fate of radionuclide spills at the surface and leakage from the base of a disposal facility. The soil-layering configuration that was simulated in the previous test problem also was used in this test case (fig. 31a). Water potentials measured by the in situ psychrometers on Julian day 175 (–2 to –10 MPa) were used as the initial conditions because this profile is representative of the steep upward water-potential gradients when the system is dry during the summer (fig. 34a; table 6).

The dry initial conditions and the soil layering that had large conductivity contrasts across the layers made this problem computationally difficult. The model was calibrated using data from the anthropogenic ^{36}Cl profile by simulating a constant flux of 1.4 mm a^{-1} (0.06 inch a^{-1}) for 35 yr, which is based on the net flux from the depth of the ^{36}Cl peak (case 1, table 6) (Scanlon, 1990). No parameter adjustment was performed, and the simulated depth of migration of the wetting front of 0.5 m (1.6 ft) was in good agreement with the penetration depth of the ^{36}Cl peak (0.5 m [1.6 ft]) (fig. 34a and b). Note the sharp water-potential gradient calculated for the base of the wetting front, which is similar to observed wetting fronts in the field after precipitation events (fig. 17).

Sensitivity analyses were conducted to evaluate the effect of varying selected parameters on the penetration depth of the wetting front as indicated by water potentials. Because the fronts were sharp, they were approximated by water potentials within ±0.1 MPa of the initial conditions. Several test cases were run in which one input parameter was changed in each case. The nominal case (case 2, table 6) consisted of one-dimensional simulations of 10-mm a^{-1} (0.4-inch a^{-1}) applied flux and a total simulation time of 50 yr. The parameters were similar to those used in the calibration run. The test cases evaluated changes in the input parameters that ranged from 10 percent to 99 percent of the values used in the nominal case. Increases and decreases in grid size, applied flux, and Ks; increases in initial water potentials; and decreases in residual water contents were evaluated. The input parameters and their effects on the wetting front are summarized in figure 35.

The wetting front penetrated to a depth of 2.43 m (8 ft) in the nominal case. A reduction in the grid size from 0.05 to 0.01 m (0.16 to 0.03 ft) in the upper 5 m (16 ft) resulted in a slightly shallower wetting front (2.38-m [7.8-ft] depth), which differs from the nominal case by approximately 2 percent. The CPU time required to solve the flow equation for the finer grid was approximately 1440 s, whereas that required for the nominal case was 600 s. A coarser grid size of 0.1 m (0.3 ft) was also evaluated and resulted in a wetting-front depth of 2.55 m (8.4 ft), which is 5 percent deeper than the nominal case. Because of the increased CPU time required for the very fine grid, particularly in two-dimensional simulations, a grid size of 0.05 m (0.16 ft) in the upper 5 m (16 ft) and 100 mm (3.9 inches) in the lower 10 m (33 ft) was used in the remainder of the simulations.

The penetration depth of the wetting front is most sensitive to variations in the applied flux, which ranged from 1 to 19 mm a^{-1} (0.04 to 0.7 inch a^{-1}). The effect of variations in the flux are asymmetrical (that is, the decrease in wetting-front depth caused by reducing the flux is much less than the increase in wetting-front depth caused by increasing the flux by the same amount). Variations in the initial water potentials had a negligible effect on the position of the wetting front except in cases where the water potential was high (–0.1 MPa at the surface). Increasing the initial ψ values results in a corresponding increase in the water content, which effectively decreases the storage capacity of the system and allows the wetting front to penetrate more deeply. This minimal effect of the initial conditions, except at high water potentials, is attributed to the shape of the retention curves, which show negligible variations in θ corresponding to large variations in ψ, except at high ψ values (fig. 32a). The unsaturated hydraulic conductivity also increases as the initial water potential increases and results in a more rapid migration of the wetting front. The penetration of the wetting front is rather insensitive to variations in Ks. Variations in the residual-water contents were also evaluated, and retention curves were fitted with new values of θ_r. Only reductions in θ_r were considered in the sensitivity analyses because increasing the residual-water content above the lowest observed values is not realistic. Reducing the residual-water content is similar to increasing the storage capacity of the unsaturated zone and results in a slightly shallower wetting front.

These sensitivity analyses show the relative importance of the different factors controlling the migration of the wetting front. The most significant variables are the applied flux and the initial water potentials.

Two-dimensional simulations of infiltration were used to evaluate the amount of lateral flow and the effect of the upward-decreasing water potentials (case 3, table 6). A finer grid was employed in the area of applied flux because steeper water-potential gradients are expected in this zone (fig. 36). The applied flux was restricted to 1 m (3 ft) of the upper surface, and the remaining boundary conditions consisted of constant water potential at the base and zero flux on all other sides (fig. 36). Zero flux was assigned to the left side for symmetry. The dimensions of the grid were set to minimize the effect of the lower and right boundary conditions on the flow solution. The initial conditions were similar to those used in the one-dimensional simulations and were uniform across each layer. A flux of 10 mm a^{-1} (0.4 inch a^{-1}) was applied at the surface (Neumann boundary condition) for 50 yr. To examine redistribution of moisture, the surface flux was reduced to 0 for the next 50 yr and the total simulation time was 100 yr.

Propagation of the wetted region is illustrated in figure 37a through c. The core of the wetted zone is represented by the –0.05-MPa contour, and the fringe of the wetted region is represented by water potentials that are within ±0.1 MPa of the initial conditions. Because the initial conditions consist of upward-decreasing water potentials, the fringe contour varies in water potential with depth. The core of the wetted plume penetrates approximately three times more in the vertical direction than in the horizontal direction (fig. 37a). In contrast, the fringe of the wetted zone propagates laterally the same distance that it moves vertically (fig. 37b). The greater vertical movement of the core of the plume relative to the fringe is attributed to the increased gravitational component of flow at these higher water potentials. Although initially the water-potential gradients are fairly uniform in the horizontal and vertical directions (fig. 38a), after 50 yr of infiltration the water-potential gradients are much steeper in the vertical direction than in the horizontal direction (fig. 38b). During redistribution, the core of the moisture plume shrinks as the surface dries (water potential decreases) and the base of the core remains stationary (fig. 38c). Eventually the wetted zone becomes attenuated. The water-potential gradients are markedly reduced at the end of the redistribution period compared with those at the end of the infiltration period (fig. 38b and c).

To simulate potential leakage from the base of the proposed facility, a constant flux was applied at a depth of 10 m (33 ft) for 50 yr (case 4, table 6). The grid was the same as that used in the previous simulation (fig. 36); however, it would be more realistic to exclude natural sediments above the zone of applied flux to represent a disposal facility. Most of the applied water moved vertically upward (fig. 39a). The initial water potentials are fairly uniform (~ –2 MPa) at this depth and probably do not control the preferential upward flow of water. The depth at which the flux was applied (10 m [33 ft]) marks the contact between overlying silty clay and underlying gravel (fig. 31a) and may affect the direction of water movement because the unsaturated hydraulic conductivity of the gravel is much lower than that of the silty clay at the initial water potential. To further test this hypothesis another simulation was run with uniform lithology of silty clay (case 5, table 6). The results of this simulation show that water moves equal distances upward and downward (fig. 39b) and confirms the hypothesis that at low water potentials water moves preferentially into the finer grained material. These data suggest that in areas of uniform water potentials, soil layering and the corresponding unsaturated hydraulic conductivity may be critical in controlling the direction of water movement.

Test Problem 3

In order to evaluate the hydrologic effect of the contact between the shallow coarse-grained material and the deeper clays, one- and two-dimensional flow into a 2-m (6.6-ft) loamy sand section underlain by 4 m (13 ft) of clay was simulated. Hydraulic conductivity and retention curves were not determined in the deep clays in this study; therefore, hydrologic parameters for shallow clays were used in the simulations. Because the bulk densities of the deep clays (1.9 to 2.0) are much higher than those of the surficial clays (1.3), the saturated hydraulic conductivity of the deep clays would be expected to be lower than those of the surficial clays (Ks=850 mm a^{-1} [33 inches a^{-1}]). Reported saturated hydraulic conductivities for these deep clays range from 6×10^{-13} to 3×10^{-10} m s^{-1} (1.97×10^{-12} to 9.8×10^{-10} ft s^{-1}) (Kreitler and others, 1987). The contrast in saturated hydraulic conductivity at the contact between the shallow coarse material and deeper clay was approximately three orders of magnitude. A uniform matric potential at –0.1 MPa was used as an initial condition because of the numerical difficulty of simulating large fluxes into dry systems. In order to obtain a better fit for the retention curves in the high water-potential range, only water-potential data ≥–1.5 MPa were used in the RETC program, and θ_r was fixed at a value slightly lower than the θ value that corresponds to –1.5 MPa (table 5). A constant flux was imposed at the upper boundary, and applied fluxes ranged from 11 to 1.1×10^4 mm a^{-1} (0.4 to 433 inches a^{-1}) in different computer runs.

When flux values were less than the Ks of the clay, the clay remained unsaturated (fig. 40a and b). Flux values similar to the Ks of the clay resulted in saturation at the contact between the clay and overlying coarser material (fig. 40c and d). Saturation of the clay and coarser material resulted when the applied flux was approximately 10 times greater than Ks of the clay (fig. 40e and f). Two-dimensional simulation results show lateral spreading of the saturated zone at the lithologic contact (fig. 41a). Increasing the anisotropy in the saturated hydraulic conductivity by 2 resulted in a greater degree of lateral spreading (fig. 41b). Based on the reported saturated hydraulic conductivities of the clays (Kreitler and others, 1987) and the simulation results, fluxes similar to –0.02 to 10 mm a^{-1} (-7.9×10^{-4} to 0.4 inch a^{-1}) that reach the contact between the coarse and fine material could result in perched water conditions and lateral water movement.

DISCUSSION

Moisture Content and Water Potential

Spatial variability in moisture content is controlled primarily by variations in sediment grain size. Discontinuities in moisture content across different lithologies indicate that moisture-content variations with depth cannot be used to determine the direction of water movement. Temporal variations in moisture content were restricted to the upper 0.7 m (2.3 ft) of the unsaturated zone. The shallow penetration of the wetting zone is attributed to the fine grain size, large storage capacity, and low degree of saturation (10 to 20 percent) of the surficial sediments. In addition, high-intensity precipitation events result in a large percentage (≤50 percent) of surface runoff (Akhter and Dutton, 1990). The absence of temporal variations in moisture content monitored in deep access tubes indicates that recharge pulses were not moving through the system. Because a constant flux could result in temporally invariant moisture content, the absence of such variations does not preclude recharge.

The range in water potentials measured by the laboratory psychrometer (–15.6 to –0.1 MPa) is compatible with the range observed from the in situ psychrometers (<–8 to –1.7 MPa) and suggests that sample drying during collection for laboratory measurements was minimal. The low observed water potentials indicate that the unsaturated system is very dry. Unsaturated hydraulic conductivities that correspond to water potentials from –15 to –2 MPa range from 2.6×10^{-24} to 2.0×10^{-21} m s^{-1} (8.5×10^{-24} to 6.6×10^{-21} ft s^{-1}) for gravel and 3.3×10^{-18} to 5.1×10^{-16} m s^{-1} (1.1×10^{-17} to 1.7×10^{-15} ft s^{-1}) for clay. Because of these low hydraulic conductivities and low water potentials, moisture fluxes are expected to be minimal.

Except in the upper 0.5 m (1.6 ft) after rainfall, the water-potential gradients indicate upward flow under isothermal conditions, probably controlled by evapotranspiration. Sharp water-potential gradients associated with steep wetting fronts may not be clearly defined by laboratory water-potential measurements because the water potentials were homogenized within the sample interval thickness (0.05 m [0.16 ft]), and detailed sampling in borehole 41C (sample interval thickness 0.01 m [0.03 ft]) showed that water potential gradients at the base of the wetting fronts were ≤–13 MPa in 0.05 m (0.16 ft). Although laboratory water potential measurements generally are not used to evaluate temporal variations in water potential because of destructive sampling, lower water potentials of samples collected in the summer relative to those collected in the winter probably reflect higher evapotranspiration rates in the summer. The high evaporation zone is more condensed in the winter and closer to land surface (borehole 56, fig. 17h).

Temporal variations in water potential were recorded primarily in the shallow (≤0.8 m [≤2.6 ft]) psychrometers that were installed in the field. These psychrometers showed gradually decreasing water potential from March through August, which was attributed to increased evapotranspiration in this period. Because of temperature gradients, the shallowest depth that could be monitored was 0.3 m (1 ft); therefore, wetting fronts at shallower depths could not be monitored. Psychrometers above 0.8 m (2.6 ft) were out of range throughout much of the monitoring period, which could result from the unsaturated zone being too dry or too wet; however, evaporation curves for these psychrometers indicated that the system was too dry.

Calculated osmotic potentials were close to zero; therefore, osmotic-potential gradients can be ignored in the equation describing flow at this site. Downward temperature gradients in the summer and upward temperature gradients in the winter result in a net zero temperature gradient throughout the year. The downward summer temperature gradients generally oppose the observed water-potential gradients and may result in downward movement of water vapor; however, numerical simulations by Milly (1984) suggested that the nonisothermal vapor flow component is negligible.

Comparison with Other Arid Regions

Results of studies at the Hueco Bolson were compared with those from other arid regions to evaluate controls on unsaturated flow. Although many of the earlier studies concentrated on flow in the shallow zone in response to agricultural irrigation (Gaudet and others, 1977; Van de Pol and others, 1977), recent interest in unsaturated systems of arid regions has developed because of their suitability as repositories of radioactive materials.

Studies of unsaturated flow related to radioactive-waste disposal have been conducted at Hanford, Washington, Beatty and Yucca Mountain, Nevada, and Las Cruces, New Mexico (Enfield and others, 1973; Gee and Heller, 1985; Montazer and others, 1985; Nichols, 1987). These sites represent a variety of hydrologic and climatic conditions. In areas of shallow-water tables, such as near Socorro, New Mexico, matric potential was high ($\geq$–0.08 MPa) and calculated Darcy fluxes ranged from 8 to 37 mm a^{-1} (0.3 to 1.5 inch a^{-1}) (Stephens and Knowlton, 1986). The high matric potentials in this arid region are attributed to the shallow ($\leq$5 m [$\leq$16 ft]) water table. The water-table depth can be used to estimate water potentials in the unsaturated zone because if the unsaturated zone is in hydraulic equilibrium with the water table, then the sum of the matric and gravitational potentials is zero and the matric potential at the soil surface is equal to the water table depth. Lower water potentials recorded in most other arid regions reflect, in part, deeper (≥100 m [≥328 ft]) water tables in these regions and generally require the use of psychrometers. Much of the psychrometric data in the literature is questionable because of poor installation procedures and lack of sophisticated data loggers for recording water potentials accurately. Laboratory-based and field-installed psychrometers were used to measure water potential in a 387-m-deep (1,269-ft) borehole in Yucca Mountain (Montazer and others, 1985). In situ water potentials ranged from 0 to –4 MPa and were an order of magnitude higher than laboratory-based measurements. This discrepancy between laboratory and field measurements was attributed in part to sample drying during drilling with vacuum reverse air circulation below 18 m (59 ft). Various problems make it difficult to interpret the field water-potential data, such as the use of water to drill part of the borehole, the large diameter borehole (4.4 m [14.4 ft]), which resulted in long equilibration times (≤90 d), and the lack of information on evaporation curves to distinguish between wet and dry systems. All the water-potential data at this site were from zones deeper than those monitored in the Hueco Bolson.

Comparison of water-potential data from Hanford and the Hueco Bolson shows that the unsaturated zone of the Hueco Bolson is much drier than that of Hanford (fig. 42). Water potentials ranged from 0 to –1 MPa at Hanford, and calculated flow rates were ≤10 mm a^{-1} (≤0.4 inch a^{-1}) (Enfield and others, 1973). Water potentials generally were higher than what would be expected if the unsaturated zone were in equilibrium with the water table and indicate that the system is draining. Although the mean annual precipitation at Hanford (160 mm [6.3 inches]) is much lower than that recorded in the Hueco Bolson (280 mm [11 inches]), much of the precipitation at Hanford occurs as snowfall when temperature and evapotranspiration are lowest and recharge potential is greatest. These data indicate that the seasonal precipitation pattern may be more important than the amount of precipitation in determining deep percolation within the unsaturated zone. Also, surficial sediments are much coarser at Hanford, which would further contribute to drainage at this study area. Psychrometers were installed to 14 m (46 ft) in a vertical shaft at Beatty (Morgan and Fisher, 1984). Lower water potentials at Beatty (J. M. Fisher, personal communication, 1989) relative to those in the Hueco Bolson indicate that the unsaturated zone at Beatty is drier, and the drier conditions are attributed to lower annual precipitation (110 mm [4.3 inches]). The water potential gradients at Beatty and in the Hueco Bolson indicate upward movement of water, which is controlled by evapotranspiration. Comparison of physical data from these study areas indicates that meteorologic (mean annual precipitation and seasonal precipitation pattern), hydrologic (depth to water table), and soil texture must all be considered in determining unsaturated-flow conditions.

Limitations of the Numerical Simulations

The modeling studies were restricted to analysis of single-phase, isothermal flow; however, physical-flow processes in the shallow unsaturated zone are much more complex with liquid and vapor transport in response to water potential and temperature gradients. Evaluating the relative importance of liquid- and vapor-phase flow is difficult because studies of these phenomena under natural conditions are limited. Analysis of evaporation rates in arid systems indicates that neglecting thermal effects results in an error of approximately 1 percent; therefore, unsaturated-flow processes may not be sensitive to thermal gradients (Milly, 1984).

The modeling studies neglected hysteresis because it was not measured in the soil samples. The retention curves were estimated from desorption experiments; however, most of the modeling cases involved sorption. Many of the test cases evaluated in this study simulated flow in isotropic systems. Recent field studies in arid systems indicate that the vertical to horizontal anisotropy ration of the hydraulic conductivity increases with decreasing water potential (McCord and others, 1987); however, tension-dependent anisotropy was not evaluated. Neglecting anisotropy would cause the wetting front to propagate more rapidly in the vertical direction and would reduce the degree of lateral spreading.

Results of test problem 2 indicate the importance of unsaturated hydraulic conductivity (K_u) in controlling flow directions. Field measurements of K_u by the instantaneous-profile method were restricted to the wet range and were generally not applicable for most of the modeling test cases. Data on the accuracy of K_u estimates from K_s and retention data (Van Genuchten, 1980) are generally unavailable. K_s measurements of the deeper clays are important in determining the downward flux that can be tolerated before a saturated zone develops; therefore, more detailed measurements of this parameter that would take into account the overburden pressure and the expansive nature of some of these clays are required.

CONCLUSIONS

(1) Spatial variations in moisture content are related to the distribution of sediment types in the unsaturated zone: low moisture contents are characteristic of the shallow, coarse-grained material (12 to 15 m [39 to 49 ft] thick), and high moisture contents are characteristic of the deeper clays. The surficial sediments are only 10 to 20 percent saturated, whereas the deeper clays are close to saturation.

(2) During the monitoring period, penetration of moisture was restricted to the upper 1 m (3 ft) of the unsaturated zone because of the fine grain size, large porosity, and low degree of saturation of the surficial sediments.

(3) Low measured water potentials (≥–15.6 MPa) indicate that the system is very dry. Water-potential gradients are generally positive upward except in the shallow subsurface after rainfall events. These gradients indicate primarily upward water movement under isothermal conditions, probably controlled by evapotranspiration. Osmotic-potential gradients were negligible and can be ignored in the flow equation.

(4) Numerical simulations of upward flow in a stratified soil system indicate that the fluxes are low (9 mm a^{-1} [0.35 inch a^{-1}]). One-dimensional simulations of infiltration were calibrated using ^{36}Cl data. Sensitivity analyses suggest that the most important parameters in controlling the

propagation of the wetting front are the applied flux and the initial water potentials. Two-dimensional simulations of infiltration show preferred vertical migration of the core of the moisture plume relative to the fringe of the plume. During redistribution, the moisture plume shrinks and eventually becomes attenuated.

(5) Numerical analysis of potential leakage from the base of a possible facility indicates that the direction of moisture movement is controlled by soil stratification. Lower unsaturated hydraulic conductivities of the underlying gravel relative to the overlying silty clay result in primarily upward water movement.

(6) Downward fluxes similar to the saturated hydraulic conductivity of the deeper clays will result in a saturated zone at the contact between the shallow coarse material and deeper clay. Two-dimensional simulations show lateral spreading of the saturated zone, which is dependent on the anisotropy ratio of the hydraulic conductivity.

ACKNOWLEDGMENTS

This project was funded by the Texas Low-Level Radioactive Waste Disposal Authority under contract no. IAC(88-89)0932. We acknowledge the work of the drillers, James Doss and Daniel Ortuno, and the chemical analyst, Steven W. Tweedy. The assistance of William F. Mullican III in organizing the drilling is gratefully appreciated. Alan R. Dutton reviewed early versions of the report. The manuscript was edited by Tucker F. Hentz and Lana Dieterich. Figures were drafted by J. Jobst under the direction of R. L. Dillon. Jamie H. Coggin prepared the illustrations, and word processing was done by Susan Lloyd and Melissa Snell under the direction of Susann Doenges.

REFERENCES

Ababou, Rachid, 1988, Three-dimensional flow in random porous media: Massachusetts Institute of Technology Report No. 318, 833 p.

Akhter, M. S., and Dutton, A. R., 1990, Surface-water hydrology of the proposed low-level radioactive waste isolation site, Hudspeth County, Texas: The University of Texas at Austin, Bureau of Economic Geology, report prepared for the Texas Low-Level Radioactive Waste Disposal Authority under Interagency Contract Number IAC(90-91)0268, 10 p.

Amoozegar, A., and Warrick, A. W., 1986, Hydraulic conductivity of saturated soils: field methods, *in* Klute, Arnold, ed., Methods of soil analysis, part 1. Physical and mineralogical methods: Madison, Wisconsin, American Society of Agronomy, Soil Science Society of America, p. 735–770.

Baumgardner, R. W., Jr., 1990, Geomorphology of the Hueco Bolson in the vicinity of the proposed low-level radioactive waste disposal site, Hudspeth County, Texas: The University of Texas at Austin, Bureau of Economic Geology, report prepared for the Texas Low-Level Radioactive Waste Disposal Authority under Interagency Contract Number IAC(90-91)0268, 98 p.

Bouyoucos, G. J., 1962, Hydrometer method improved for making particle size analyses of soils: Agronomy Journal, v. 54, p. 464–465.

Briscoe, R. D., 1984, Thermocouple psychrometers for water potential measurements, *in* Proceedings of the Advanced Study Institute on Advanced Agricultural Instrumentation: NATO, Report No. II, p. 1–14.

Brown, R. W., and Bartos, D. L., 1982, A calibration model for screen-caged peltier thermocouple psychrometers: U.S. Department of Agriculture Report No. 293, 24 p.

Brown, R. W., and van Haveren, B. P., 1972, Psychrometry in water relations: Logan, Utah,

Utah State University, Utah Agricultural Experiment Station, 342 p.

Campbell, G. S., 1985, Soil physics with basic transport models for soil-plant systems: New York, Elsevier, 150 p.

Davis, L. A., and Neuman, S. P., 1983, Documentation and user's guide: UNSAT2-variably saturated flow model: U.S. Nuclear Regulatory Commission Report No. NUREG/CR-3390.

de Marsily, Ghislain, 1986, Quantitative hydrogeology: London, Academic Press, 440 p.

Elrick, D. E., Reynolds, W. D., and Tan, K. A., 1988, A new analysis for the constant head well permeameter technique, *in* Proceedings of the International Conference and Workshop on the Validation of Flow and Transport Models for the Unsaturated Zone: Las Cruces, New Mexico, New Mexico State University, Department of Agronomy and Horticulture, p. 23–26.

Elrick, D. E., Sheard, R. W., and Baumgartner, N., 1981, A simple procedure for determining the hydraulic conductivity and water retention of putting green soil mixtures, *in* Proceedings of the Fifth International Turfgrass Research Conference: Ontario, Canada, University of Guelph, p. 189–200.

Enfield, C. G., Hsieh, J. J. C., and Warrick, A. W., 1973, Evaluation of water flux above a deep water table using thermocouple psychrometers: Soil Science Society of America Proceedings, v. 37, p. 968–970.

Folk, R. L., 1974, Petrology of sedimentary rocks: Austin, Texas, Hemphill, 182 p.

Gaudet, J. P., Jegat, H., Vachaud, G., and Wierenga, P. J., 1977, Solute transfer, with exchange between mobile and stagnant water, through unsaturated sand: Soil Science Society of America Journal, v. 41, p. 665–671.

Gee, G. W., and Heller, P. R., 1985, Unsaturated water flow at the Hanford site: a review of literature and annotated bibliography: Richland, Washington, Pacific Northwest Laboratory Report No. PNL-5428, 42 p.

Hillel, Daniel, Krentos, V. D., and Stylianou, Y., 1972, Procedure and test of an internal drainage method for measuring soil hydraulic characteristics in situ: Soil Science, v. 114, p. 395–400.

Hills, R. G., Hudson, D. B., Porro, I., and Wierenga, P. J., 1989a, Modelling one-dimensional infiltration into very dry soils 2. Estimation of the soil water parameters and model predictions: Water Resources Research, v. 25, p. 1271–1282.

Hills, R. G., Porro, I., Hudson, D. B., and Wierenga, P. J., 1989b, Modeling one-dimensional infiltration into very dry soils 1. Model development and evaluation: Water Resources Research, v. 25, p. 1259–1269.

Hudson, D. B., and Wierenga, P. J., 1988, Neutron probe standard counts: Madison, Wisconsin, American Society of Agronomy Abstracts, p. 184–185.

Huyakorn, P. S., Kretschek, A. G., Broome, R. W., Mercer, J. W., and Lester, B. H., 1984, Testing and validation of models for simulating solute transport in ground water: development, evaluation, and comparison of benchmark techniques: Indianapolis, Indiana, Butler University, International Ground Water Modeling Center Report No. GWMI 84-13.

Klute, Arnold, 1986, Water retention: laboratory methods, *in* Klute, Arnold, ed., Methods of soil analysis, part 1. Physical and mineralogical methods: Madison, Wisconsin, American Society of Agronomy, Soil Science Society of America, p. 635–662.

Kreitler, C. W., Raney, J. A., Nativ, Ronit, Collins, E. W., Mullican, W. F., III, Gustavson, T. C., and Henry, C. D., 1987, Siting a low-level radioactive waste disposal facility in Texas, volume four — geologic and hydrologic investigations of State of Texas and University of Texas lands: The University of Texas at Austin, Bureau of Economic Geology, final report prepared for the Low-Level Radioactive Waste Disposal Authority under contract no. IAC(86-87)1722, 330 p.

Lang, A. R. G., 1967, Osmotic coefficients and water potentials of sodium chloride solutions from 0 to 40 C: Australian Journal of Chemistry, v. 20, p. 2017–2023.

Larkin, T. J., and Bomar, G. W., 1983, Climatic atlas of Texas: Texas Department of Water Resources Report No. LP-192, 151 p.

Marquadt, D. W., 1963, An algorithm for least-squares estimation of nonlinear parameters: Journal of the Society of Industrial and Applied Math, v. 11, p. 431–441.

Marthaler, H. P., Vogelsanger, W., Richard, F., and Wierenga, P. J., 1983, A pressure transducer for field tensiometers: Soil Science Society of America Journal, v. 47, p. 624–627.

McCord, J. T., Stephens, D. B., and Wilson, J. L., 1987, Field-scale unsaturated flow and transport in a sloping uniform porous medium: field experiments and modeling considerations, *in* Proceedings of the International Conference and Workshop on the Validation of Flow and Transport Models for the Unsaturated Zone, Las Cruces, New Mexico, New Mexico State University, Department of Agronomy and Horticulture, p. 256–267.

Milly, P. C. D., 1984, A simulation analysis of thermal effects on evaporation from soil: Water Resources Research, v. 20, p. 1087–1098.

Montazer, Parviz, Weeks, E. P., Thamir, Falah, Yard, S. N., and Hofrichter, P. B., 1985, Monitoring Parviz Falah the vadose zone in fractured tuff, Yucca Mountain, Nevada, *in* Proceedings of the Conference on Characterization and Monitoring of the Vadose (Unsaturated) Zone: National Water Well Association, p. 439–469.

Morgan, D. S., and Fisher, J. M., 1984, Unsaturated-zone instrumentation in coarse alluvial deposits of the Amargosa Desert near Beatty, Nevada, *in* Proceedings of the Sixth Annual Participants' Information Meeting: U.S. Department of Energy Low-Level Waste Management Program, p. 617–630.

Mualem, Yechezkel, 1976, A new model for prediciting the hydraulic conductivity of unsaturated porous media: Water Resources Research, v. 12, p. 513–521.

Mullican, W. F., III, Kreitler, C. W., Senger, R. K., and Fisher, R. S., 1989, Truly deep saturated zone investigations at the proposed low-level radioactive waste disposal site for Texas, *in* Proceedings of the Third National Outdoor Action Conference on Aquifer Restoration, Ground Water Monitoring and Geophysical Methods: National Water Well

Association, p. 447–461.

Narasimhan, T. N., Witherspoon, P. A., and Edwards, A. L., 1978, Numerical model for saturated-unsaturated flow in deformable porous media, 3. Applications: Water Resources Research, v. 14, p. 1017–1034.

Nichols, W. D., 1987, Geohydrology of the unsaturated zone at the burial site for low-level radioactive waste near Beatty, Nye County, Nevada: U.S. Geological Survey, Water Supply Paper 2312, Report No. 57, variously paginated.

Papendick, R. I., and Campbell, G. S., 1980, Theory and measurement of water potential, *in* Water potential relations in soil microbiology: Madison, Wisconsin, Soil Science Society of America, p. 1–22.

Rawlins, S. L., and Campbell, G. S., 1986, Water potential: thermocouple psychrometry, *in* Black, C. A., Evans, D. D., White, J. L., Ensminger, L. E., and Clark, F. E., ed., Methods of soil analysis, part 1. Physical and mineralogical methods: Agronomy Monograph, p. 597–617.

Reynolds, W. D., and Elrick, D. E., 1985, In situ measurement of field-saturated hydraulic conductivity, sorptivity, and the alpha-parameter using the Guelph permeameter: Soil Science, v. 140, p. 292–302.

_____ 1986, A method for simultaneous in situ measurement in the vadose zone of field-saturated hydraulic conductivity and the conductivity-pressure head relationship: Ground Water Monitoring Review, v. 6, p. 84–95.

Robinson, R. A., and Stokes, R. H., 1959, Electrolyte solutions: London, Butterworths Publishing, 571 p.

Rose, C. W., Stern, W. R., and Drummond, J. E., 1965, Determination of hydraulic conductivity as a function of depth and water content for soil in situ: Australian Journal of Soil Research, v. 3, p. 1–9.

Scanlon, B. R., and Richter, B. C., 1990, Analysis of unsaturated flow based on chemical tracers (chloride, ^{36}Cl, ^{3}H, and bromide) and comparison with physical data, Chihuahuan Desert, Texas: The University of Texas at Austin, Bureau of Economic Geology, report prepared for the Texas Low-Level Radioactive Waste Disposal Authority under Interagency Contract Number IAC(90-91)0268, 58 p.

Spanner, D. C., 1951, The Peltier effect and its use in the measurement of suction pressure: Journal of Experimental Botany, v. 11, p. 145–168.

Stephens, D. B., and Knowlton, R. J., 1986, Soil water movement and recharge through sand at a semiarid site in New Mexico: Water Resources Research, v. 22, p. 881–889.

Travis, B. J., and Birdsell, K. H., 1990, TRACRN 1.0: a model of flow and transport in porous media for the Yucca Mountain Project, model description and user's manual: Los Alamos National Laboratory Report No. LA-UR-88-3986, 110 p.

U.S. Department of Agriculture, 1975, Soil taxonomy: Washington, D.C., Soil Conservation Service, 754 p.

Van de Pol, R. M., Wierenga, P. J., and Nielsen, D. R., 1977, Solute movement in a field soil: Soil Science Society of America Journal, v. 41, p. 10–13.

Van Genuchten, M. T., 1980, A closed-form equation for predicting the hydraulic conductivity of unsaturated soils: Soil Science Society of America, Journal, v. 44, p. 892–898.

______ 1985, RETC.F77: a program to analyze observed soil water tension and hydraulic conductivity data: Riverside, California, U.S. Salinity Laboratory Report No. 33, 36 p.

Winograd, I. J., 1981, Radioactive waste disposal in thick unsaturated zones: Science, v. 212, p. 1457–1464.

Yeh, G. T., and Ward, D. S., 1979, FEMWATER: a finite-element model of water flow through saturated-unsaturated porous media: Oak Ridge National Laboratory Report No. ORNL-5567, variously paginated.

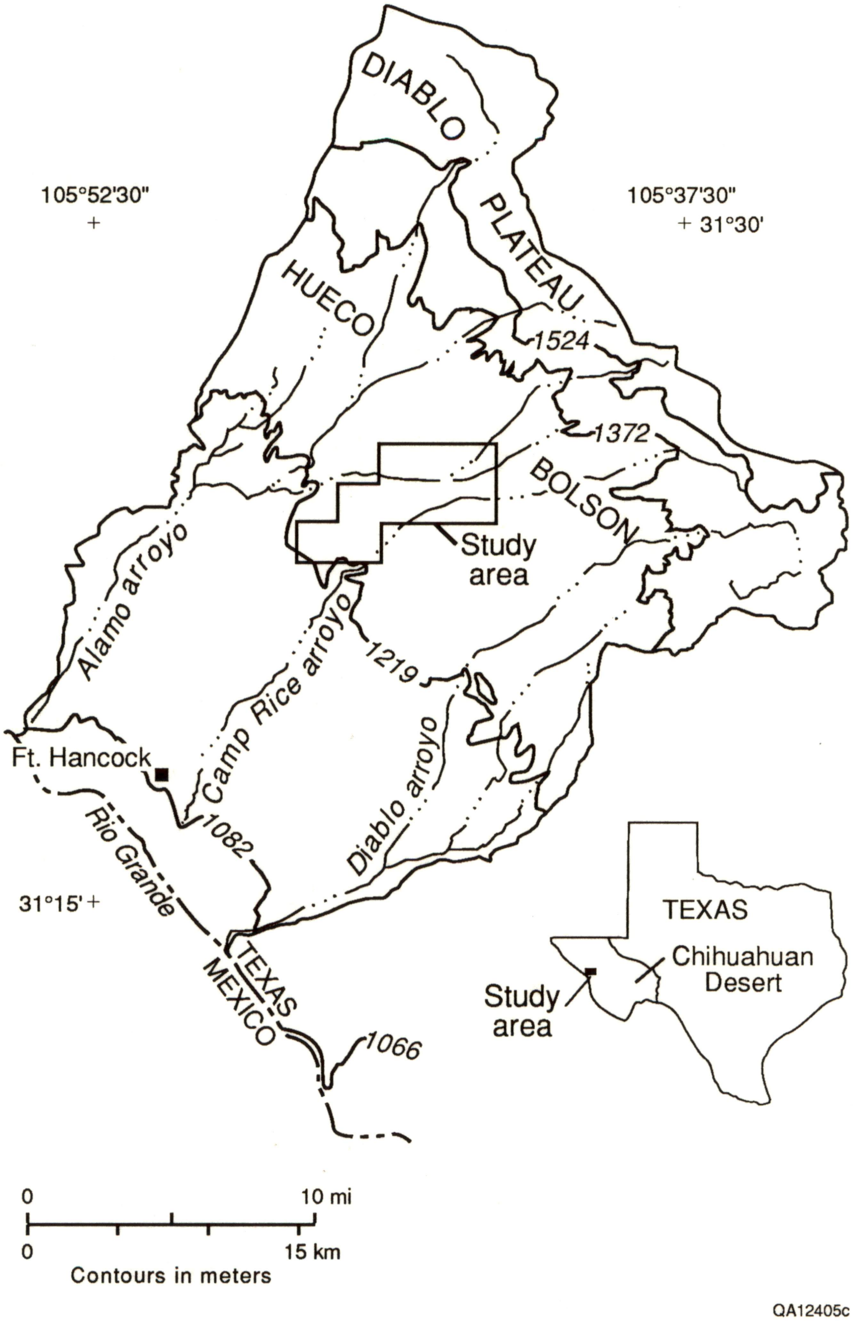

Figure 1. Location of study area.

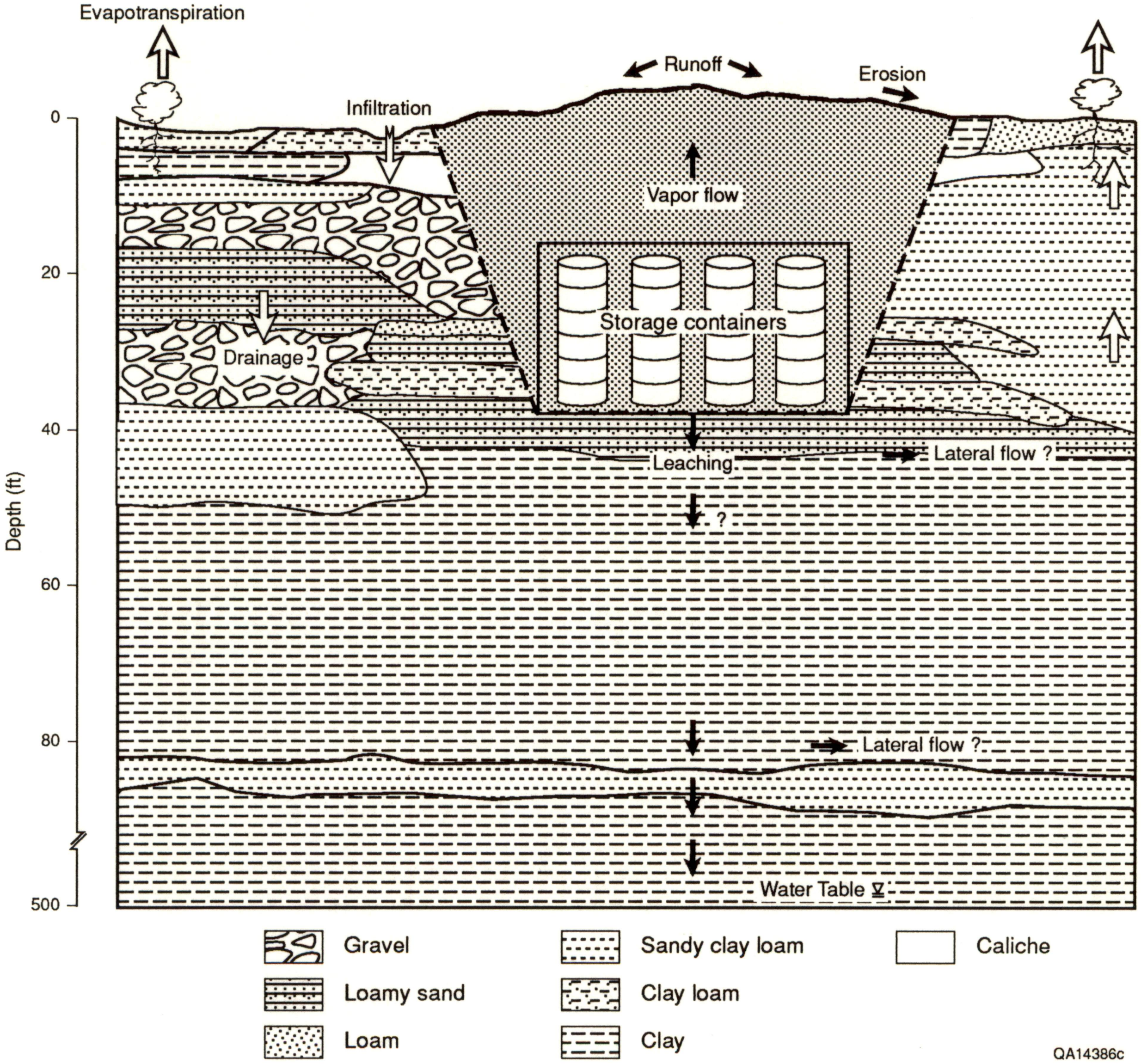

Figure 2. Conceptual model of potential pathways for radionuclide migration.

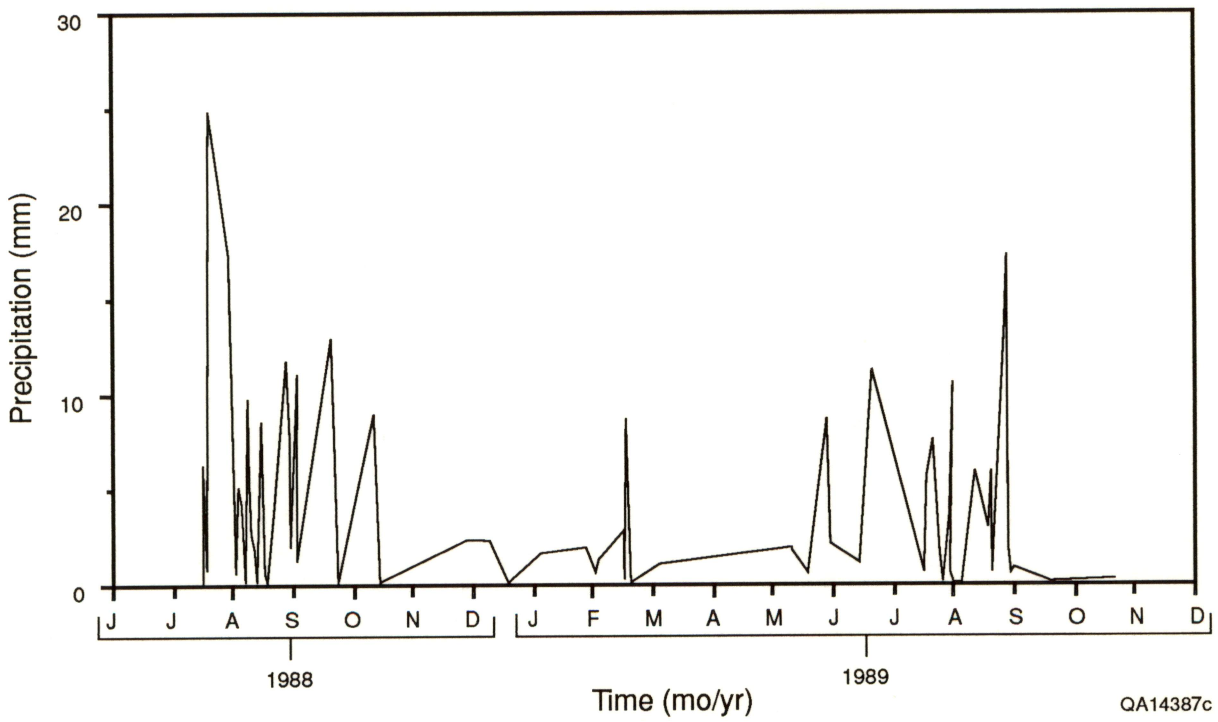

Figure 3. Daily precipitation recorded in one of the four rainfall stations from July 1988 to December 1989.

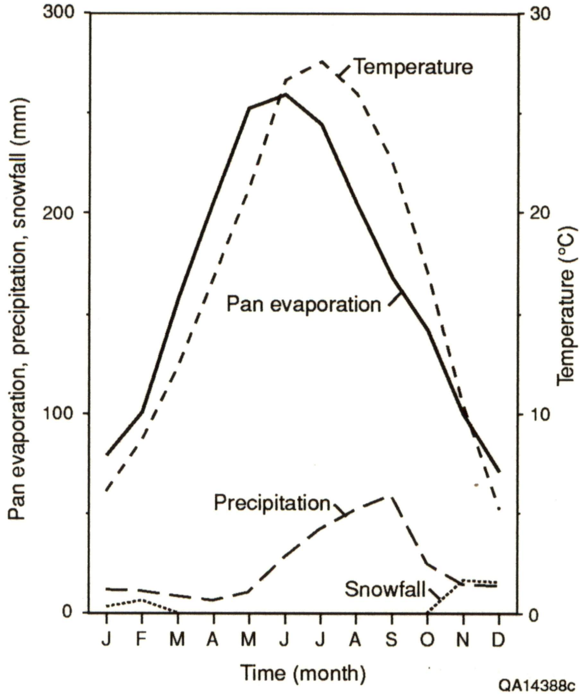

Figure 4. Mean monthly snowfall, precipitation, and temperature recorded in Fort Hancock and mean monthly pan evaporation recorded in El Paso. Monthly means were calculated from meteorological data collected between 1966 and 1987.

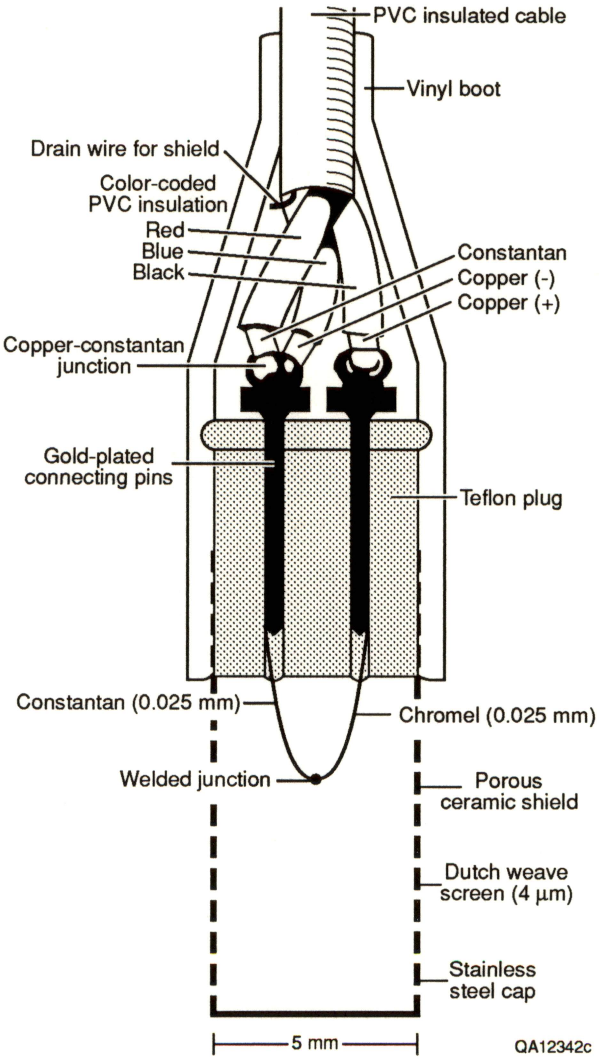

Figure 5. Screen-caged, Spanner-type thermocouple psychrometer modified from Briscoe (1984).

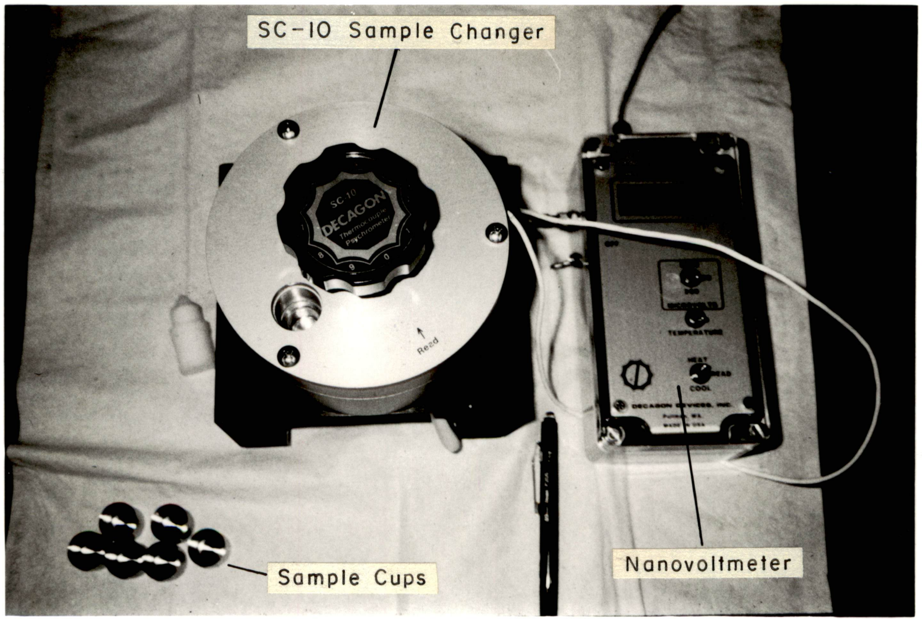

Figure 6. SC-10 thermocouple psychrometer sample changer.

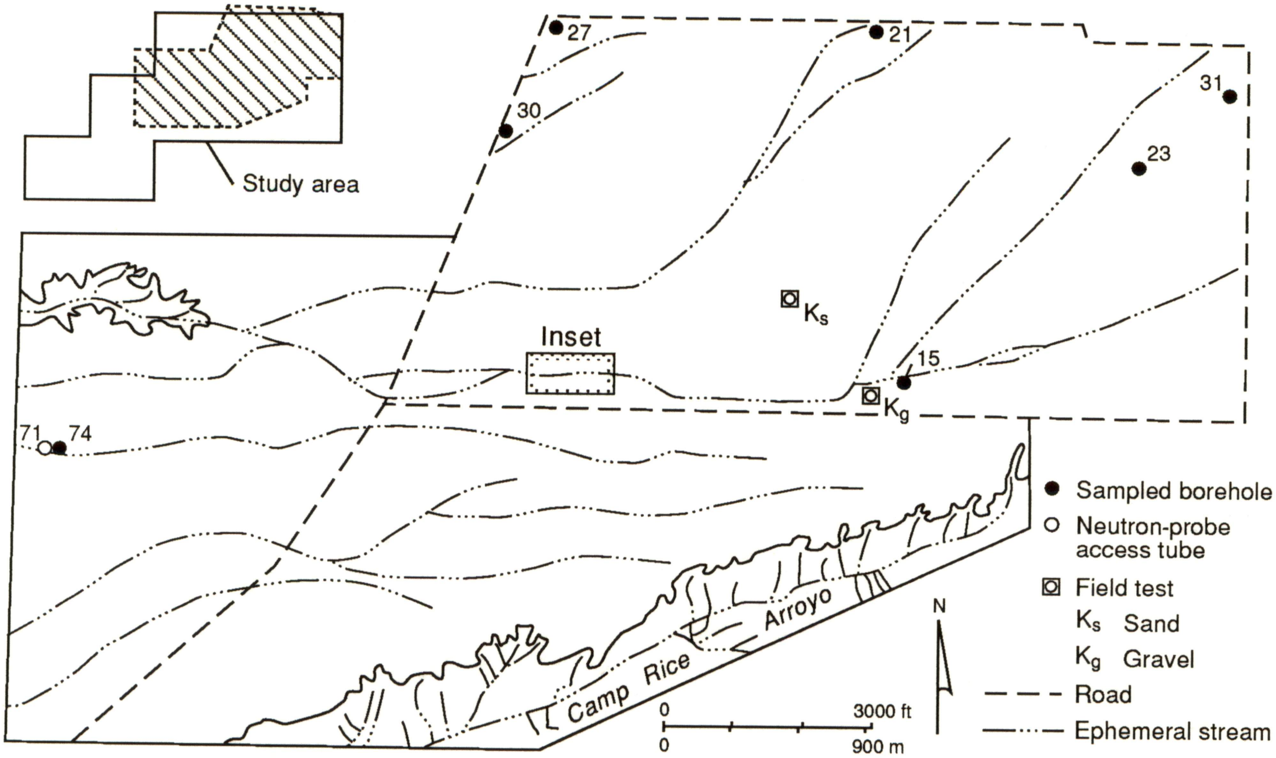

Figure 7a. Location of sampled boreholes and unsaturated-zone monitoring equipment in the study area.

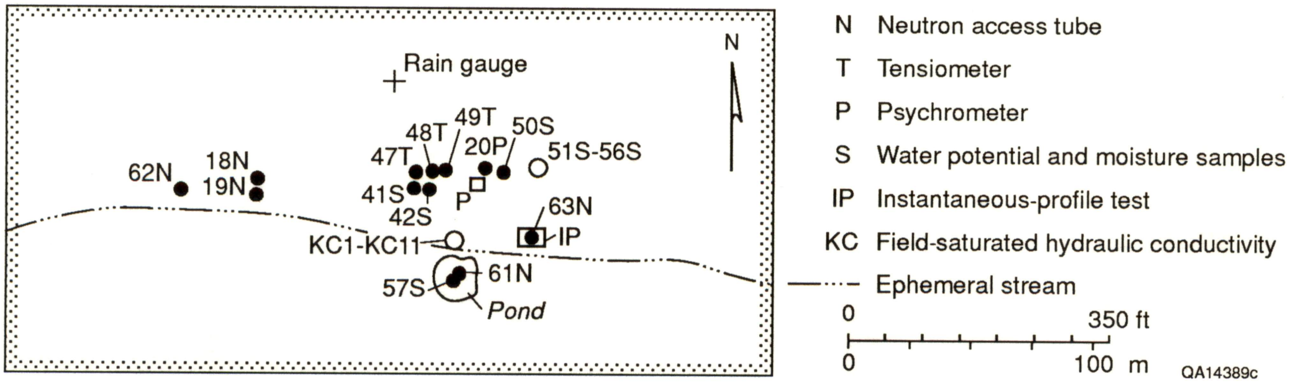

Figure 7b. Detail of unsaturated-zone studies including sampled boreholes, monitoring equipment, and hydraulic-conductivity tests in ephemeral stream.

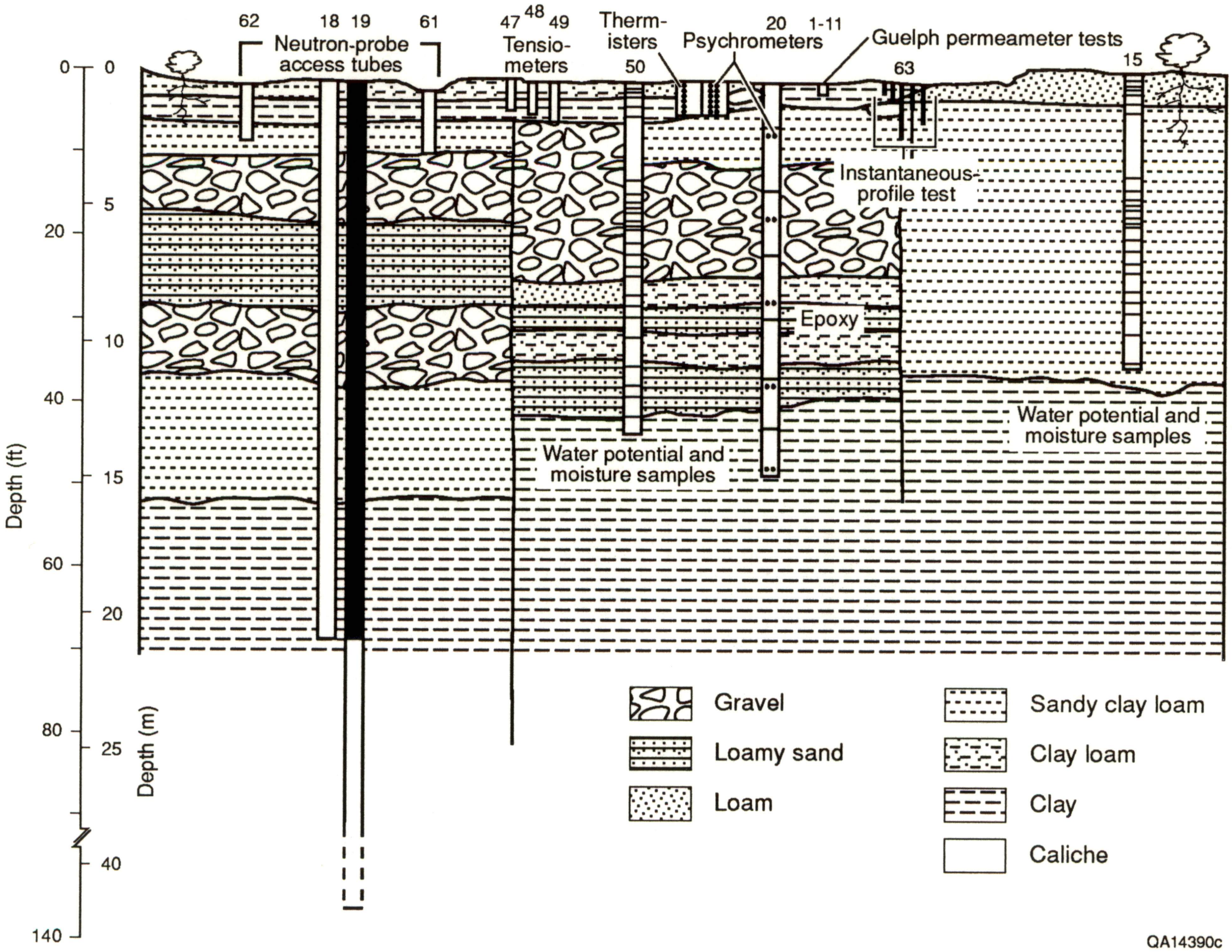

Figure 8. Schematic cross section detailing vertical distribution of monitoring equipment and sampled boreholes. This cross section generally represents studies depicted in figure 7b.

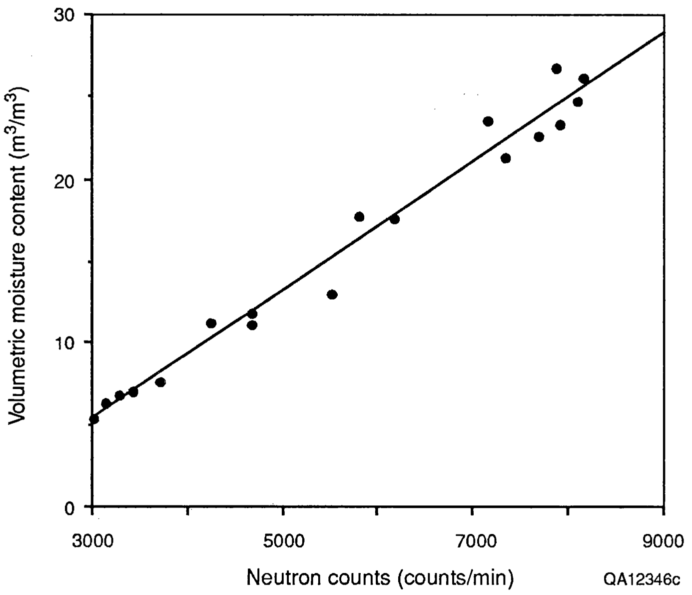

Figure 9. Calibration curve that relates moisture content to neutron count.

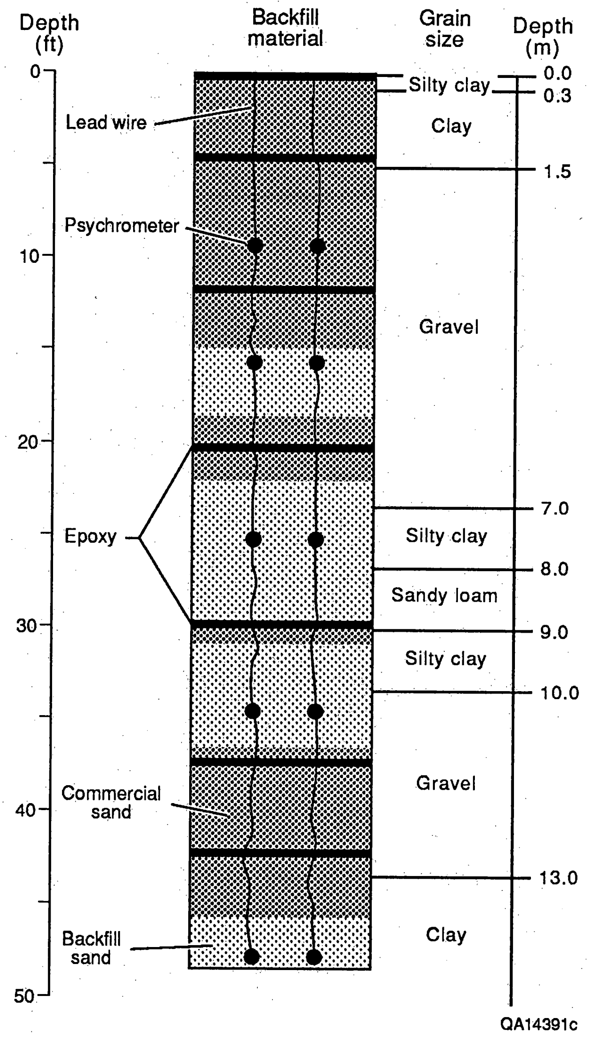

Figure 10. Distribution of psychrometers in borehole 20.

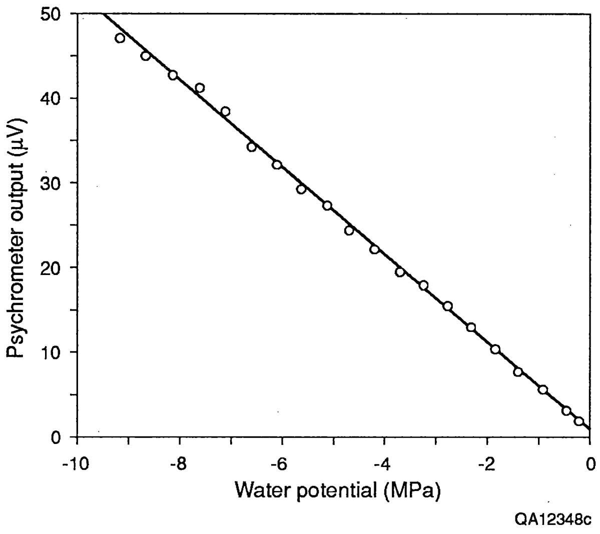

Figure 11. Calibration curve that relates SC-10 thermocouple psychrometer output (µv) to water potential (MPa). Two sets of NaCl standards are represented. Temperature was corrected to 25°C.

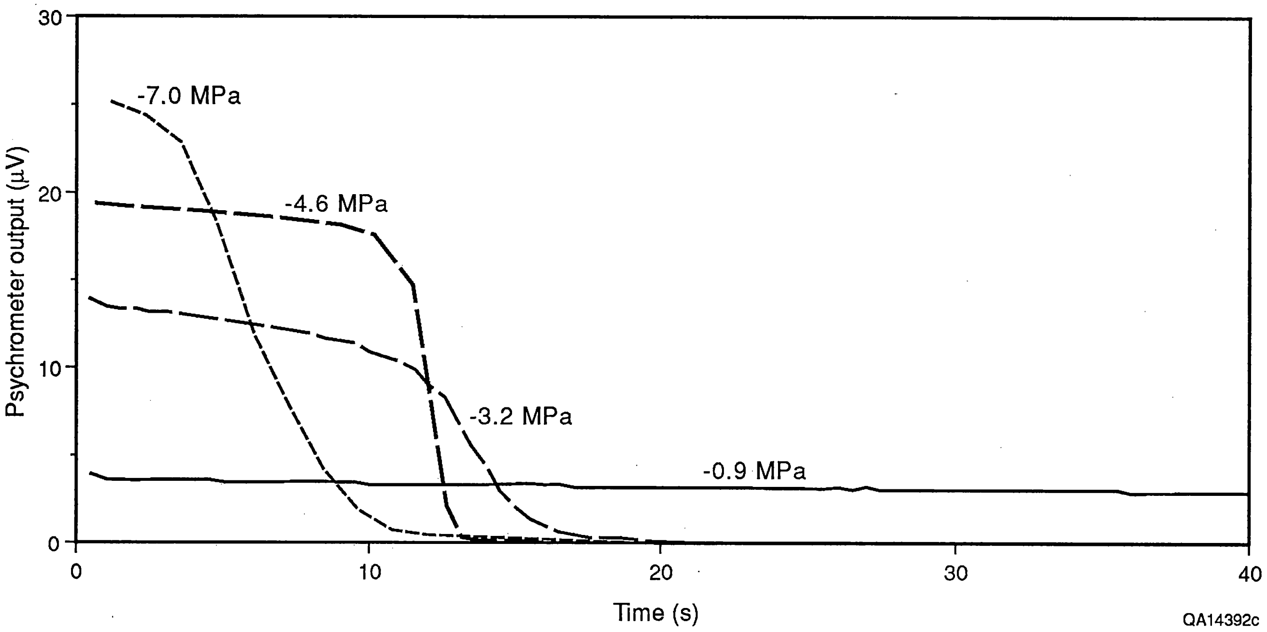

Figure 12. Typical Spanner-type thermocouple response during evaporation for different water potentials.

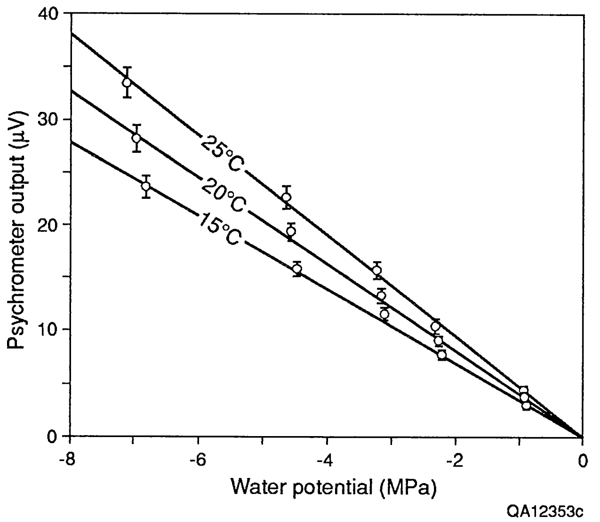

Figure 13. Calibration curve of in situ psychrometers that relates thermocouple psychrometer output (μv) to water potential (MPa). The curve represents the mean output from 24 psychrometers.

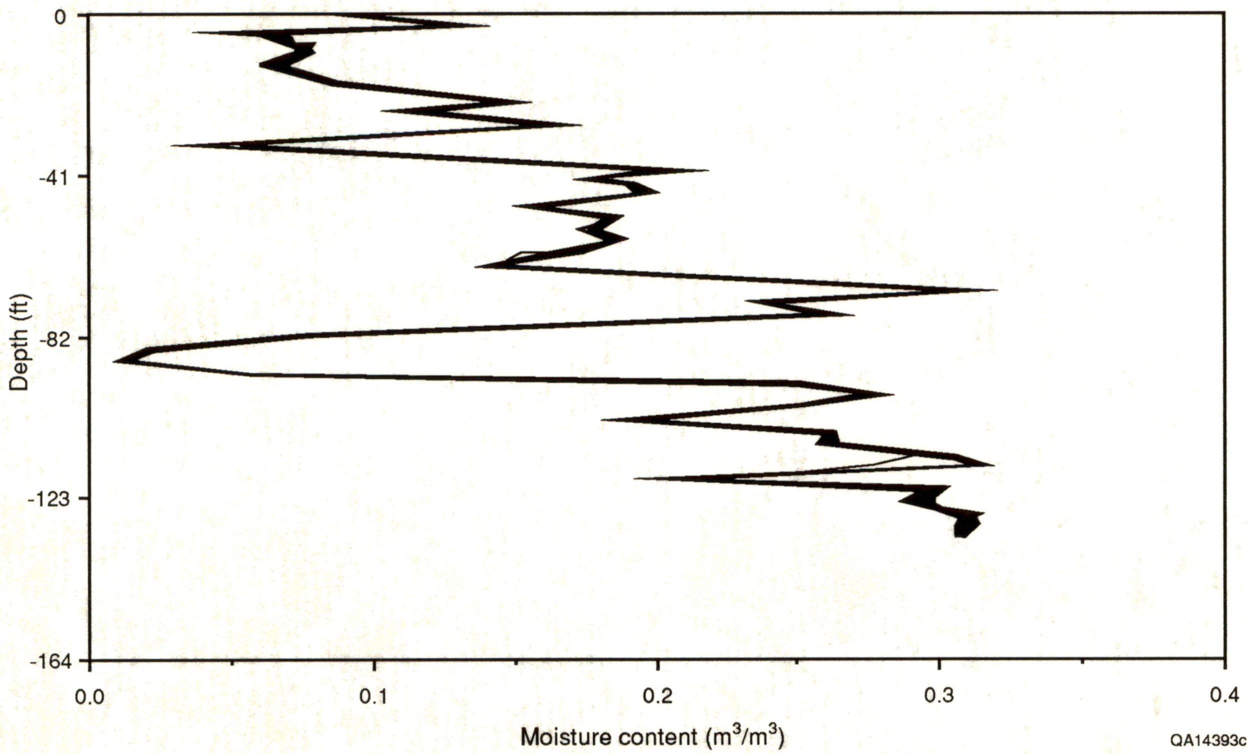

Figure 14. Variation in moisture content with depth and time in access tubes 18 and 19. Water content was monitored monthly between July 1988 and December 1989, and 17 curves are represented. The data points have been omitted for clarity. The monitoring interval ranged from 0.3-m (1-ft) intervals (from 0.3 m to 3 m [1 ft to 10 ft]) to 1-m (3.3-ft) intervals (from 3 m to 41 m [10 ft to 135 ft]). For location of access tubes, see figures 7a, 7b, and 8.

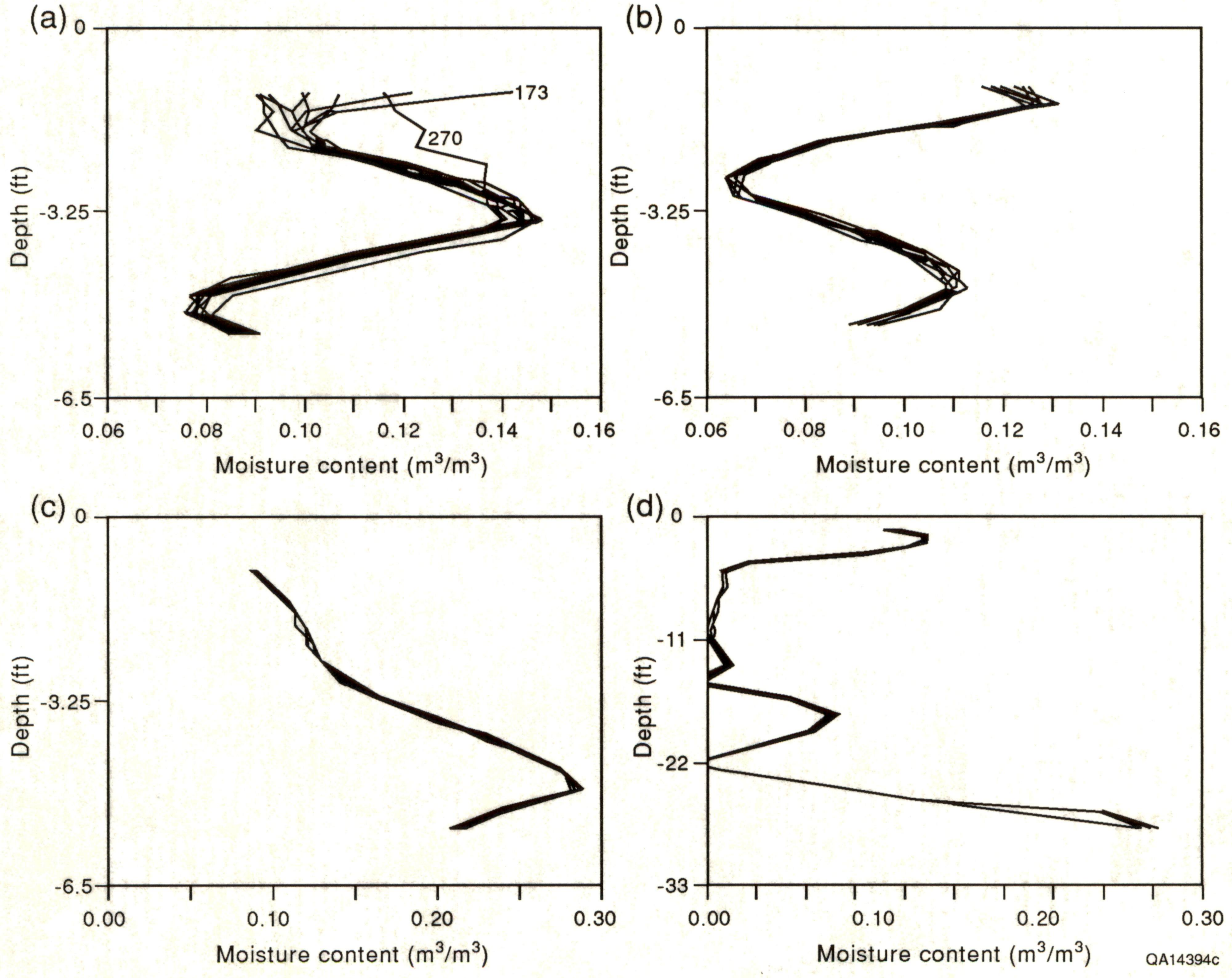

Figure 15. Variation in moisture content with depth and time in access tubes (a) 61, (b) 62, (c) 66, and (d) 71. For location of access tubes, see figure 8.

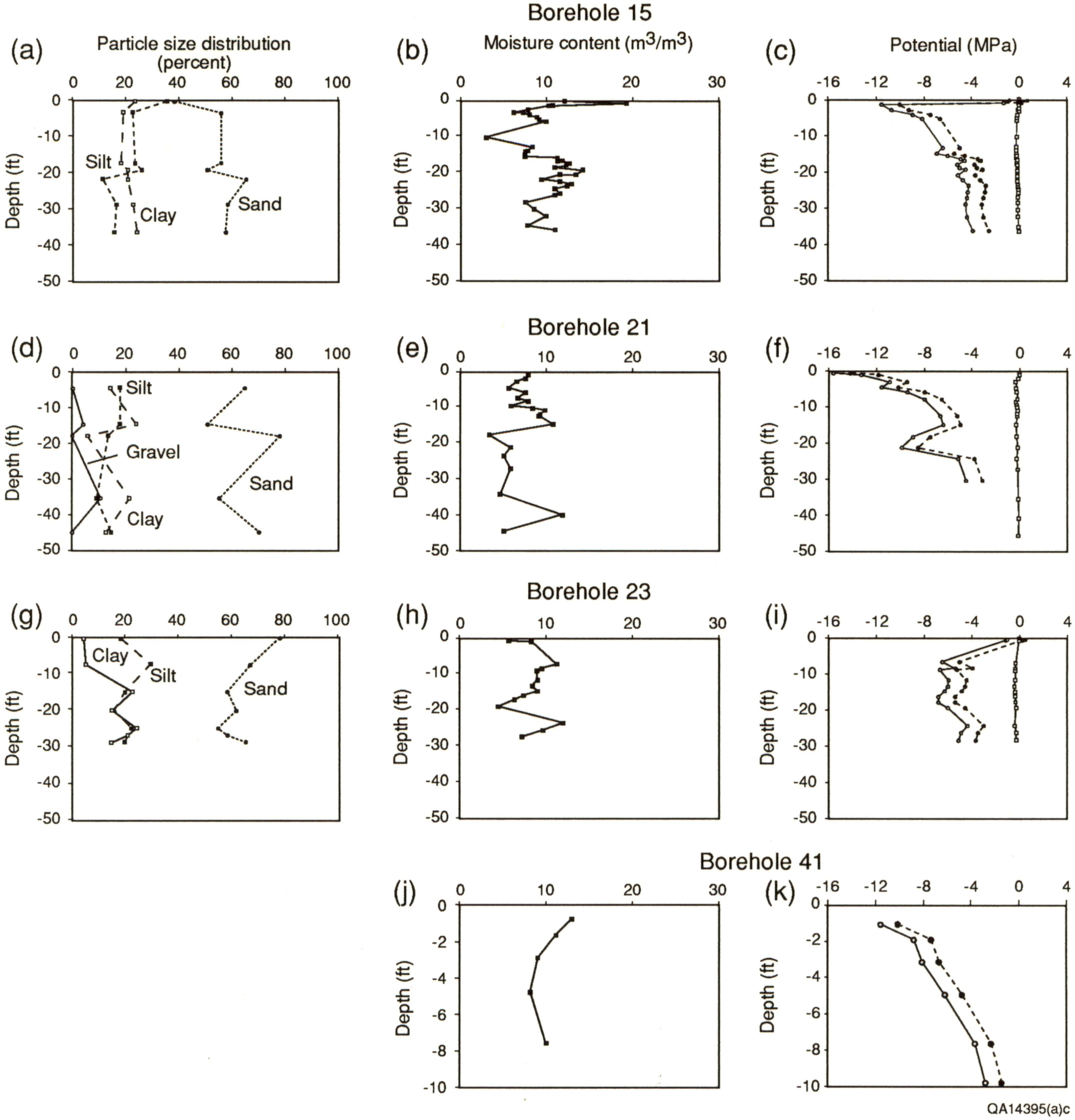

Figure 16a–t. Profiles of grain size, moisture content, and water potential for boreholes 15, 21, 23, 41, 41C, 42, 50, and 74. With the exception of borehole 74, which was sampled in September 1989, all boreholes were sampled in July and August 1988. For location of boreholes, see figures 7a and 7b.

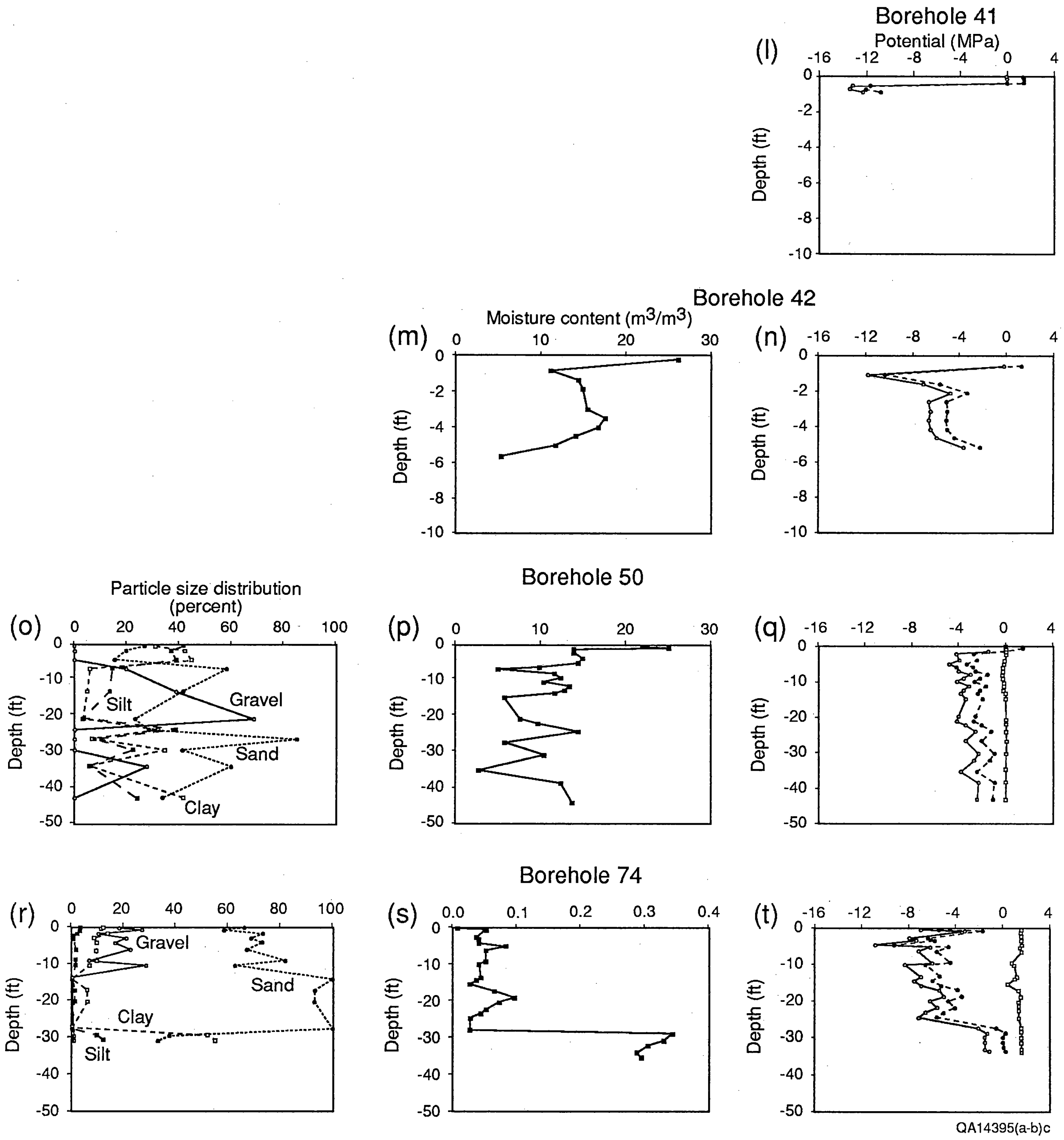

Figure 16. (continued)

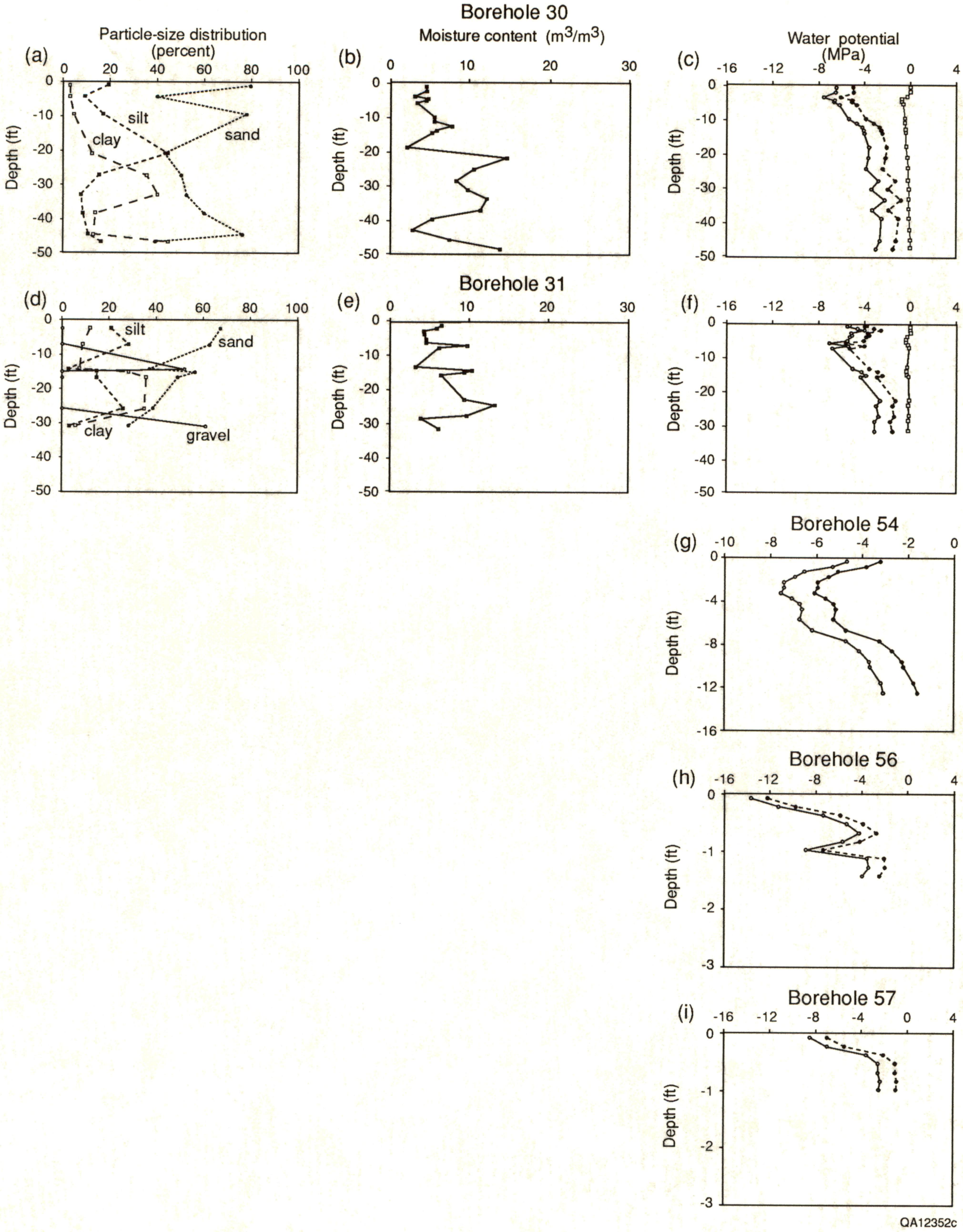

Figure 17a–i. Profiles of grain size, moisture content, and water potential for boreholes 30, 31, and water potential for boreholes 54, 56, and 57. All samples were collected in January and February 1989. For location of boreholes, see figures 7a and 7b.

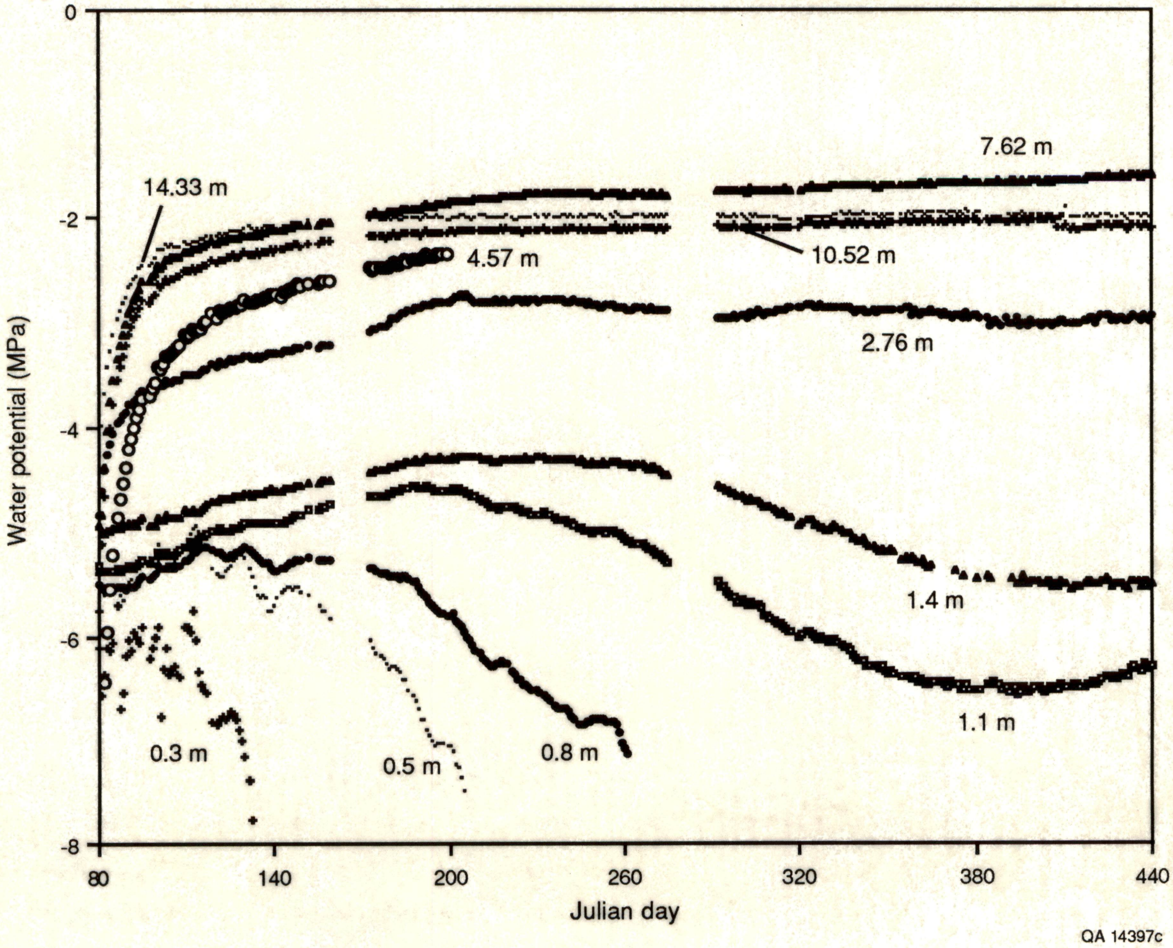

Figure 18. Temporal variations in water potential measured daily at 0900 hours in borehole 20. The monitoring period was from Julian day 80 (March 21, 1989) to Julian day 381 (January 16, 1990). For location of borehole, see figure 7b.

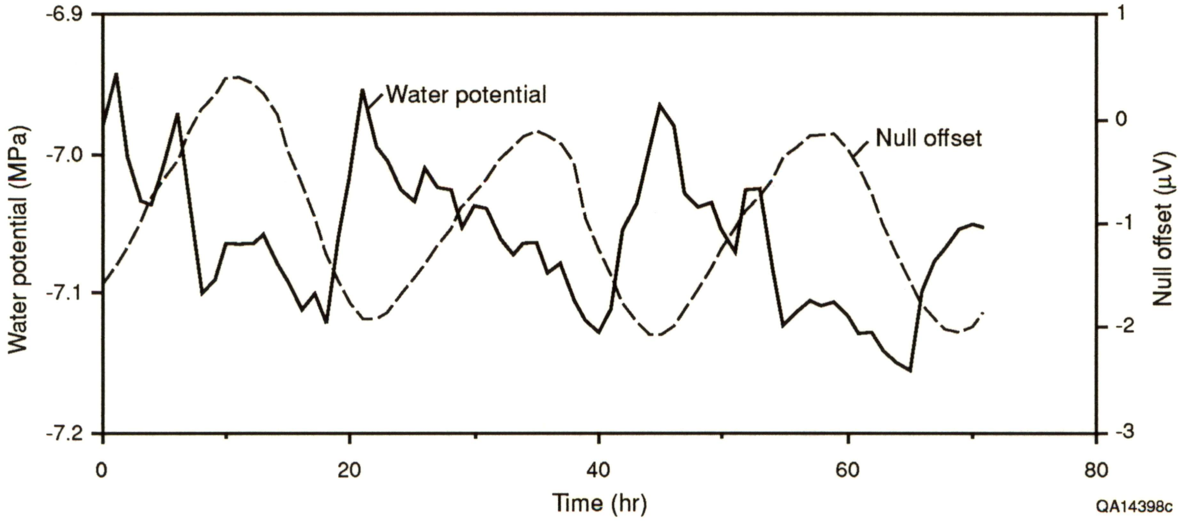

Figure 19. Relationship between variations in water potential and null offset in field psychrometers installed at 0.3-m (1-ft) depth.

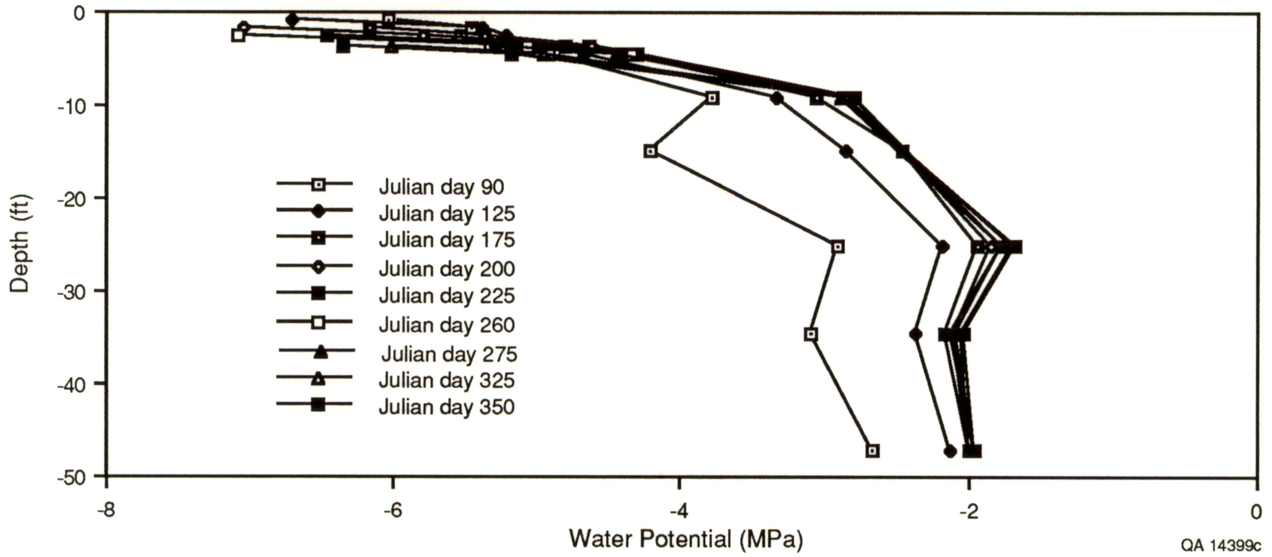

Figure 20. Vertical distribution of water potentials measured between Julian day 90 (March 31) and Julian day 350 (December 16).

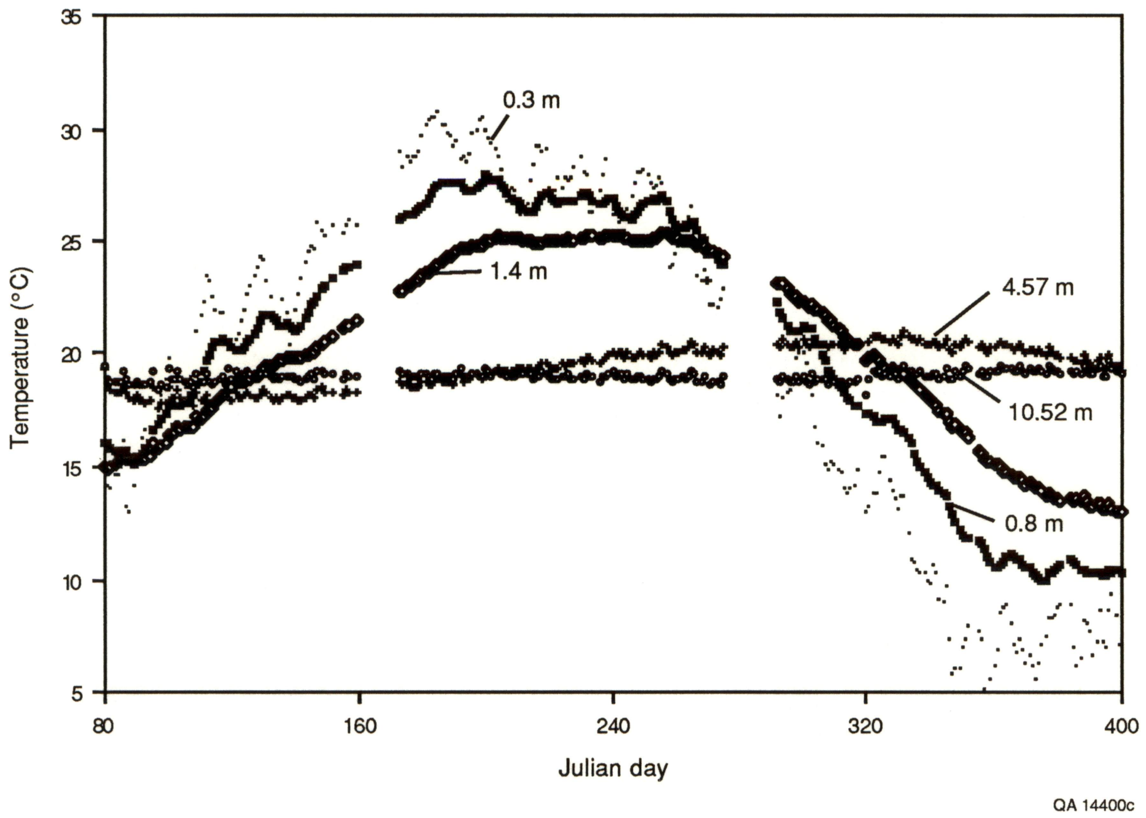

Figure 21. Temporal variations in temperature measured daily at 0900 hours in borehole 20. The monitoring period was from Julian day 80 (March 21, 1989) to Julian day 381 (January 16, 1990). For location of borehole, see figure 7b.

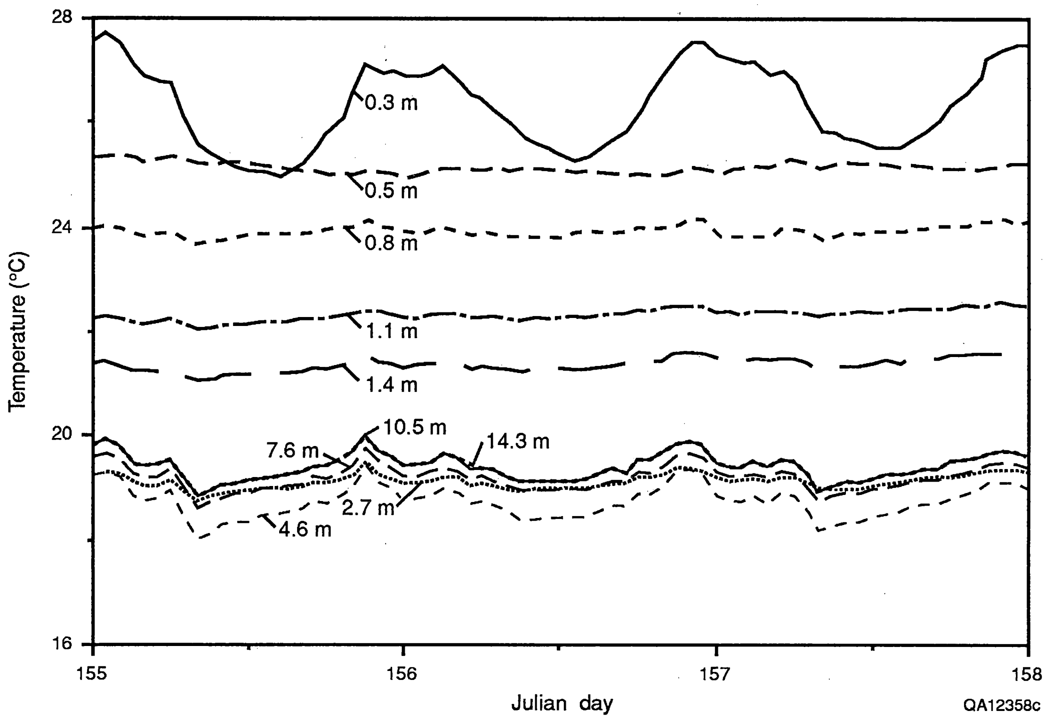

Figure 22. Hourly variations in temperature measured from Julian day 155 (June 4) to Julian day 158 (June 7).

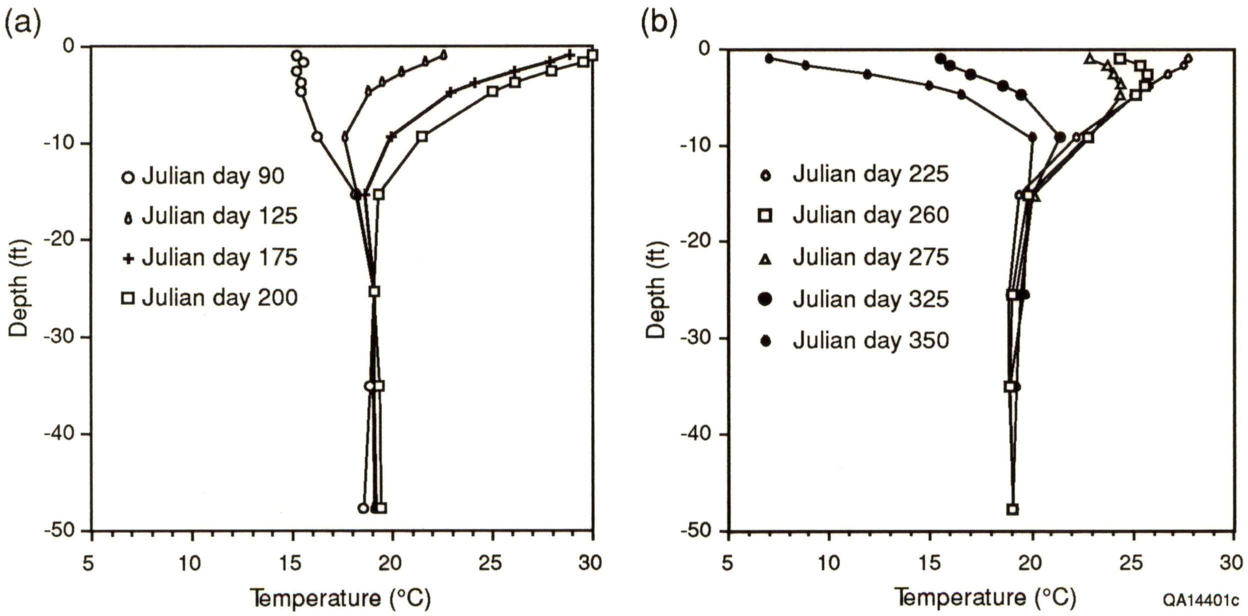

Figure 23. Vertical distribution of temperature measured between (a) Julian days 90 to 200 (March 31 to June 24) and (b) Julian days 225 to 350 (August 13 to December 16).

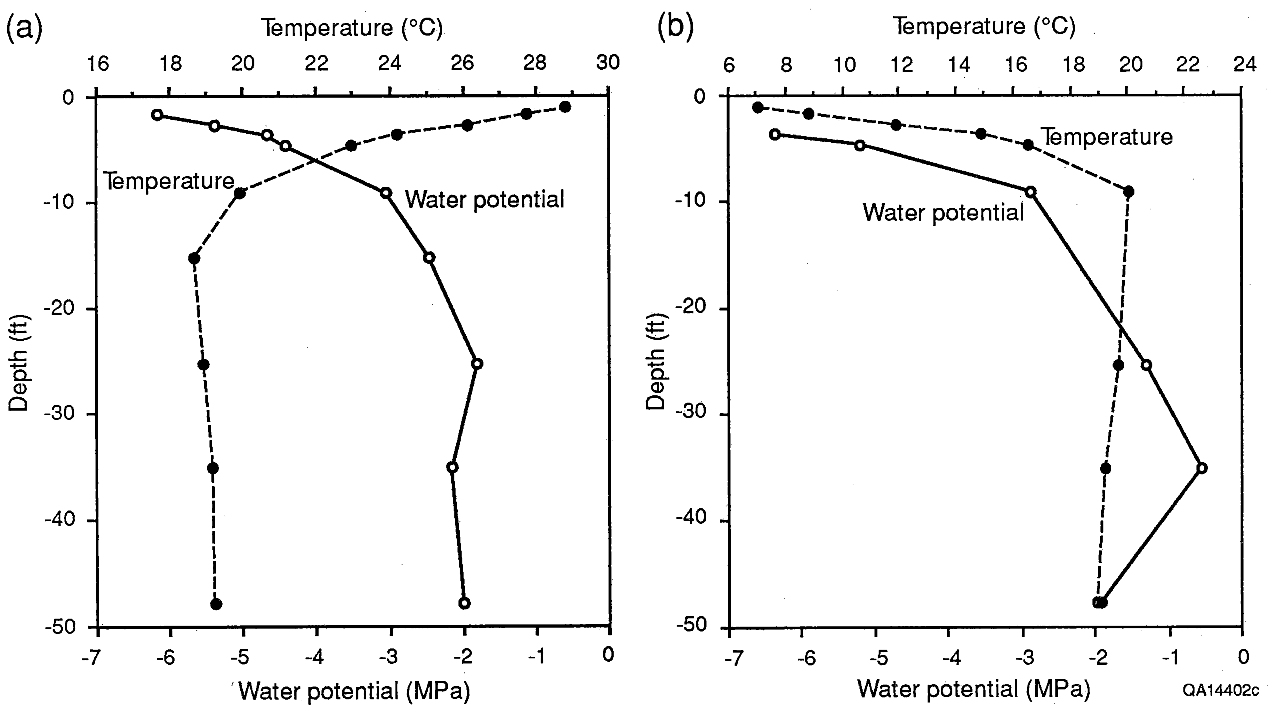

Figure 24. Comparison of water potential and temperature profiles measured on (a) Julian day 175 (June 24) and (b) Julian day 350 (December 16).

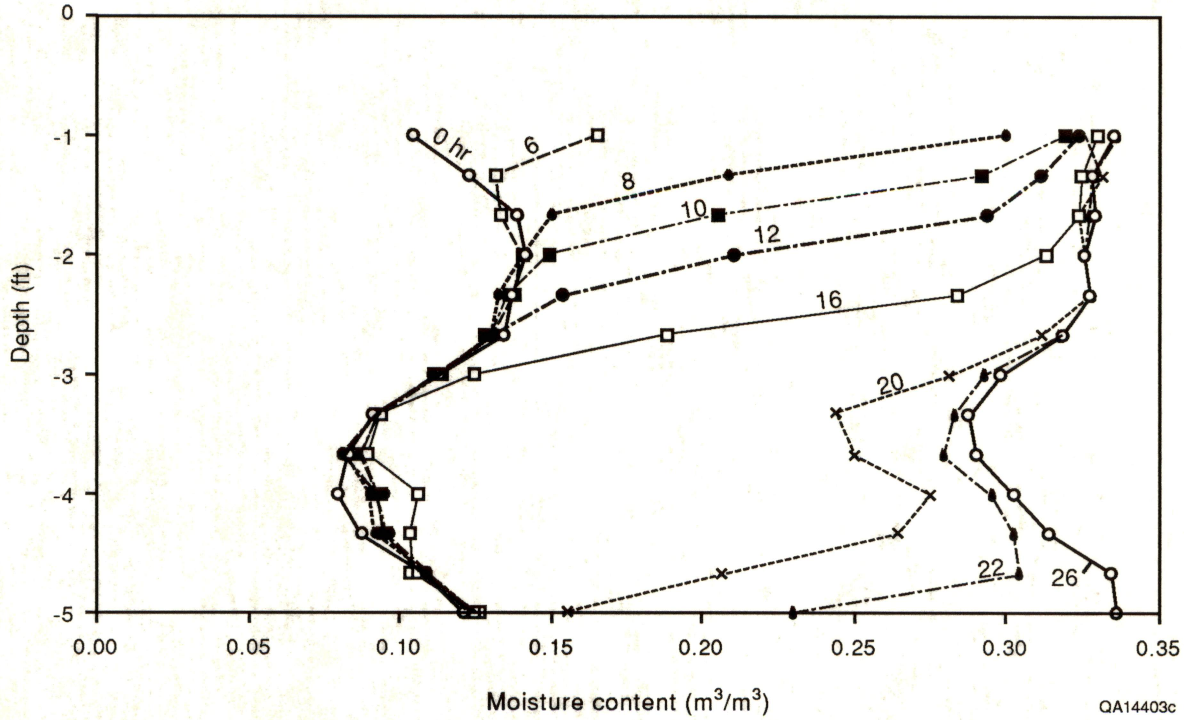

Figure 25. Propagation of the wetting front with time (hr) during the ponding phase of the instantaneous-profile test.

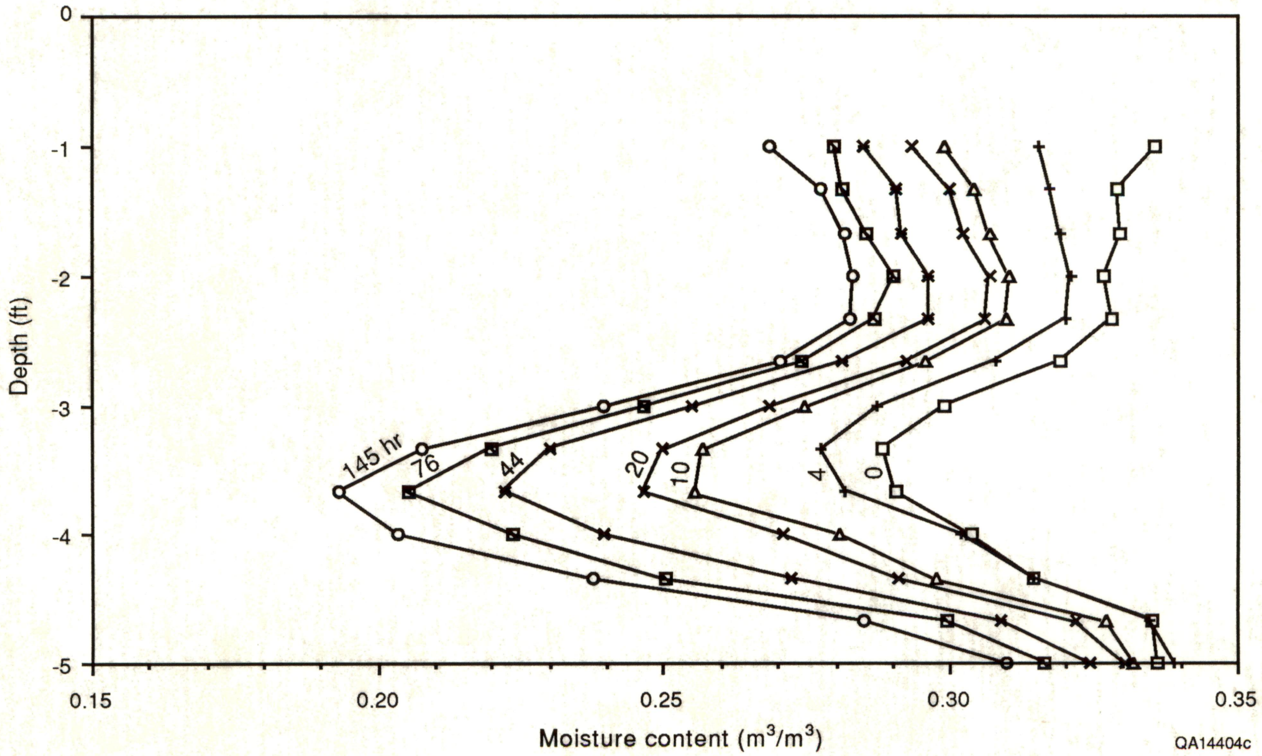

Figure 26. Moisture-content profiles measured during the drainage phase of the instantaneous-profile test.

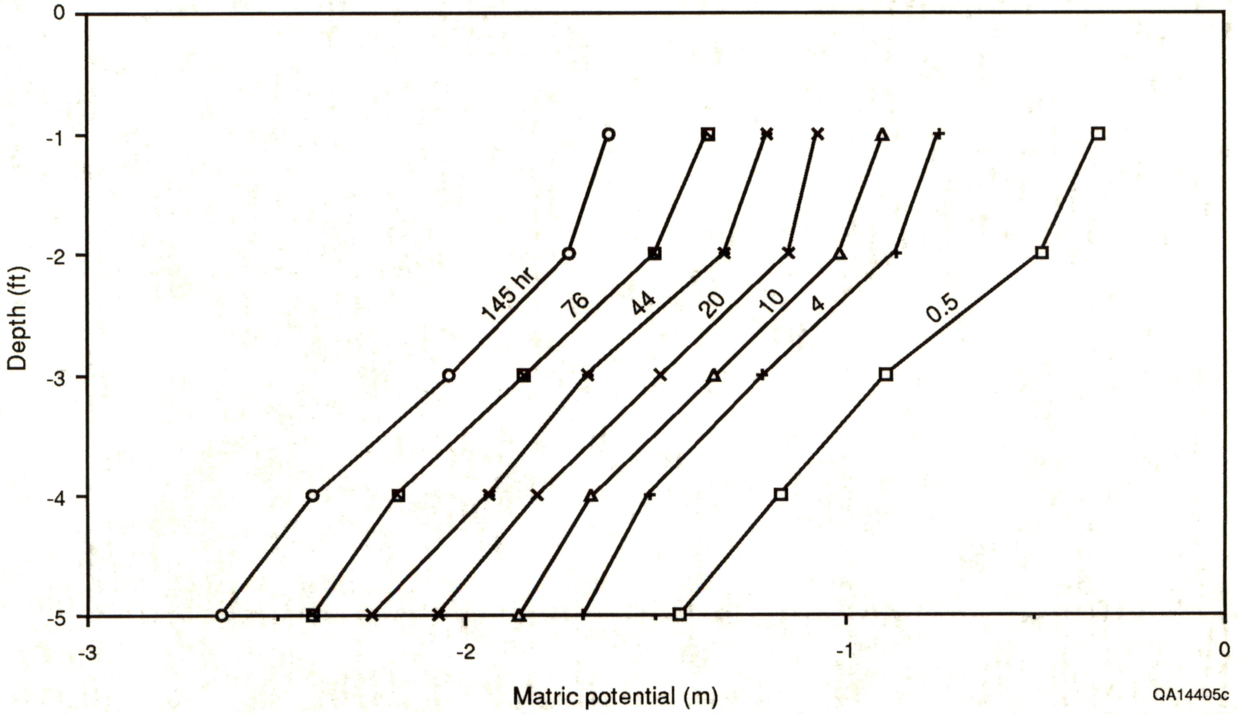

Figure 27. Vertical distribution in matric potentials during the drainage phase of the instantaneous-profile test.

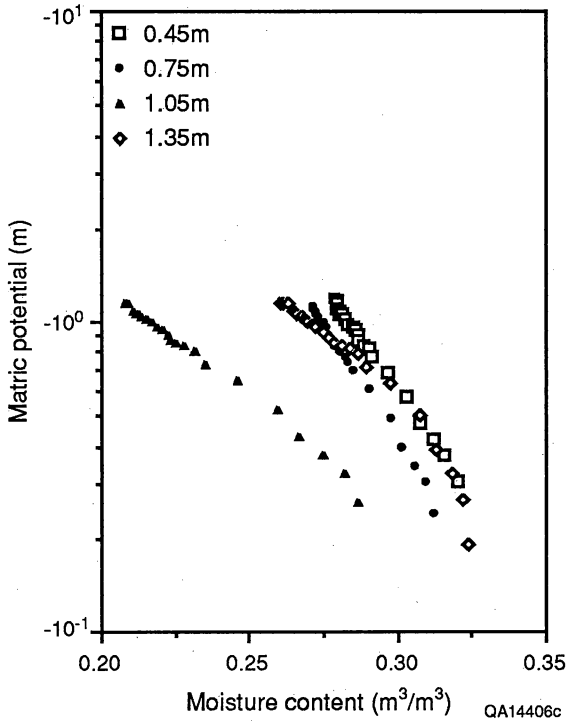

Figure 28. Retention curves based on the instantaneous-profile test.

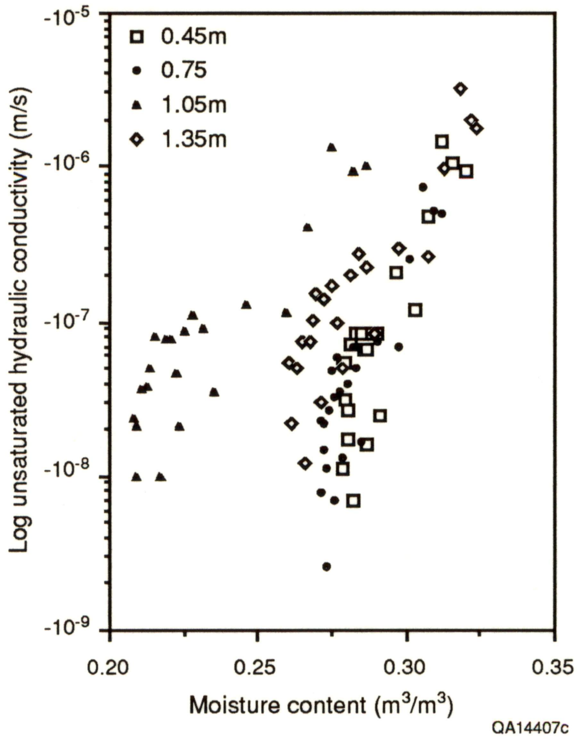

Figure 29. Unsaturated hydraulic conductivity versus moisture content based on the instantaneous-profile test.

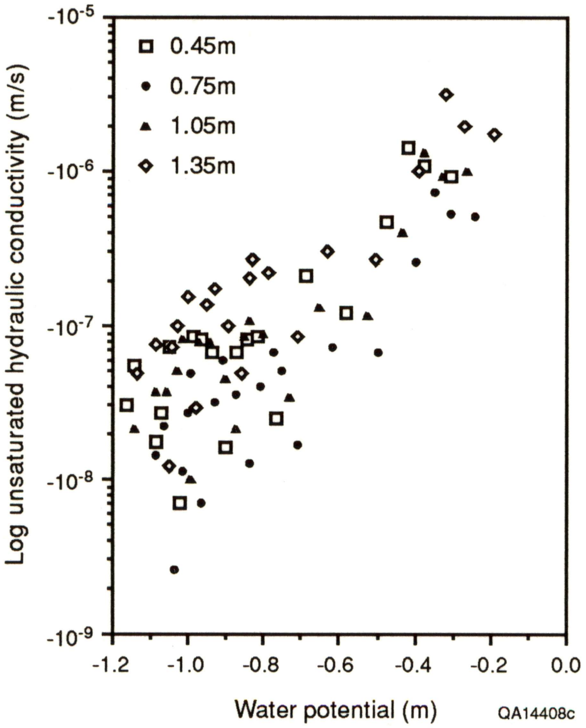

Figure 30. Unsaturated hydraulic conductivity versus water potential based on the instantaneous-profile test.

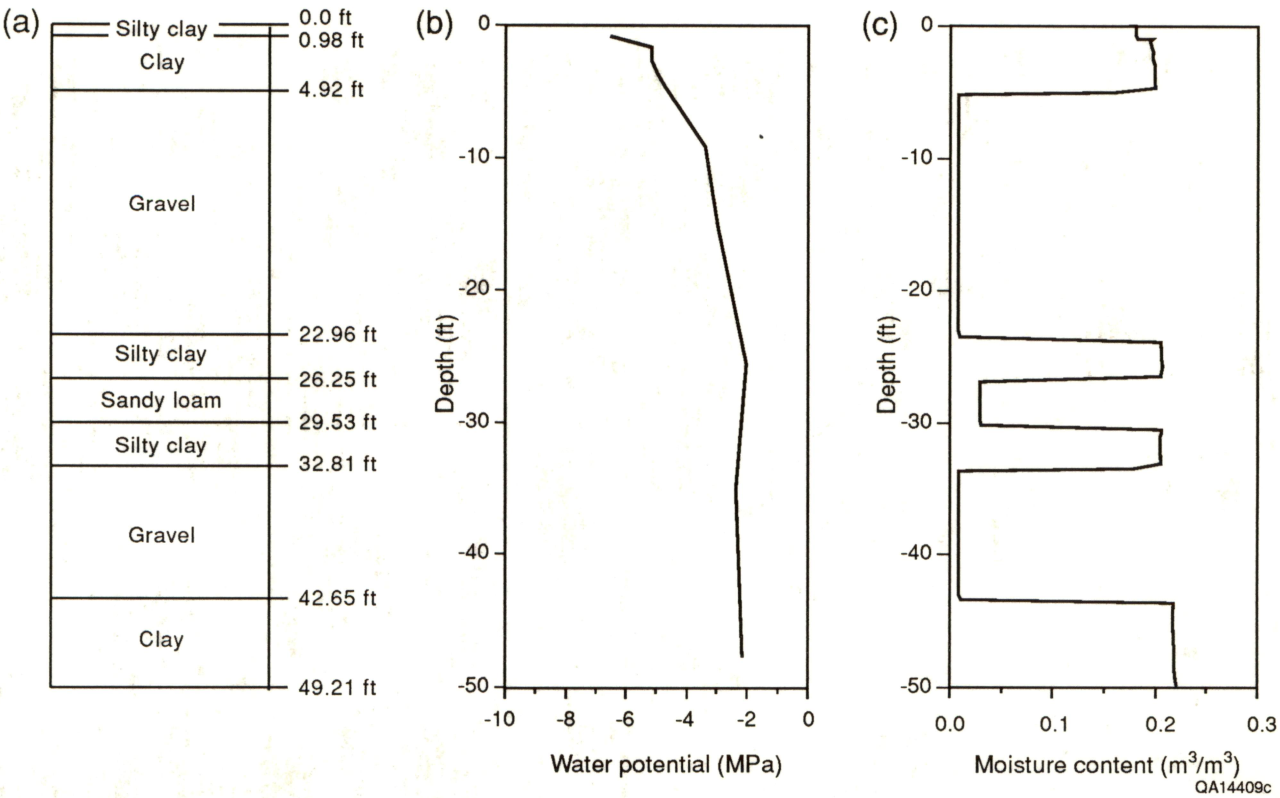

Figure 31. Grain-size classifications from borehole 50 used in (a) numerical simulations, (b) water potentials measured on Julian day 117 (April 27), and (c) the corresponding moisture content, which constitute the initial conditions for the upward-flow simulation.

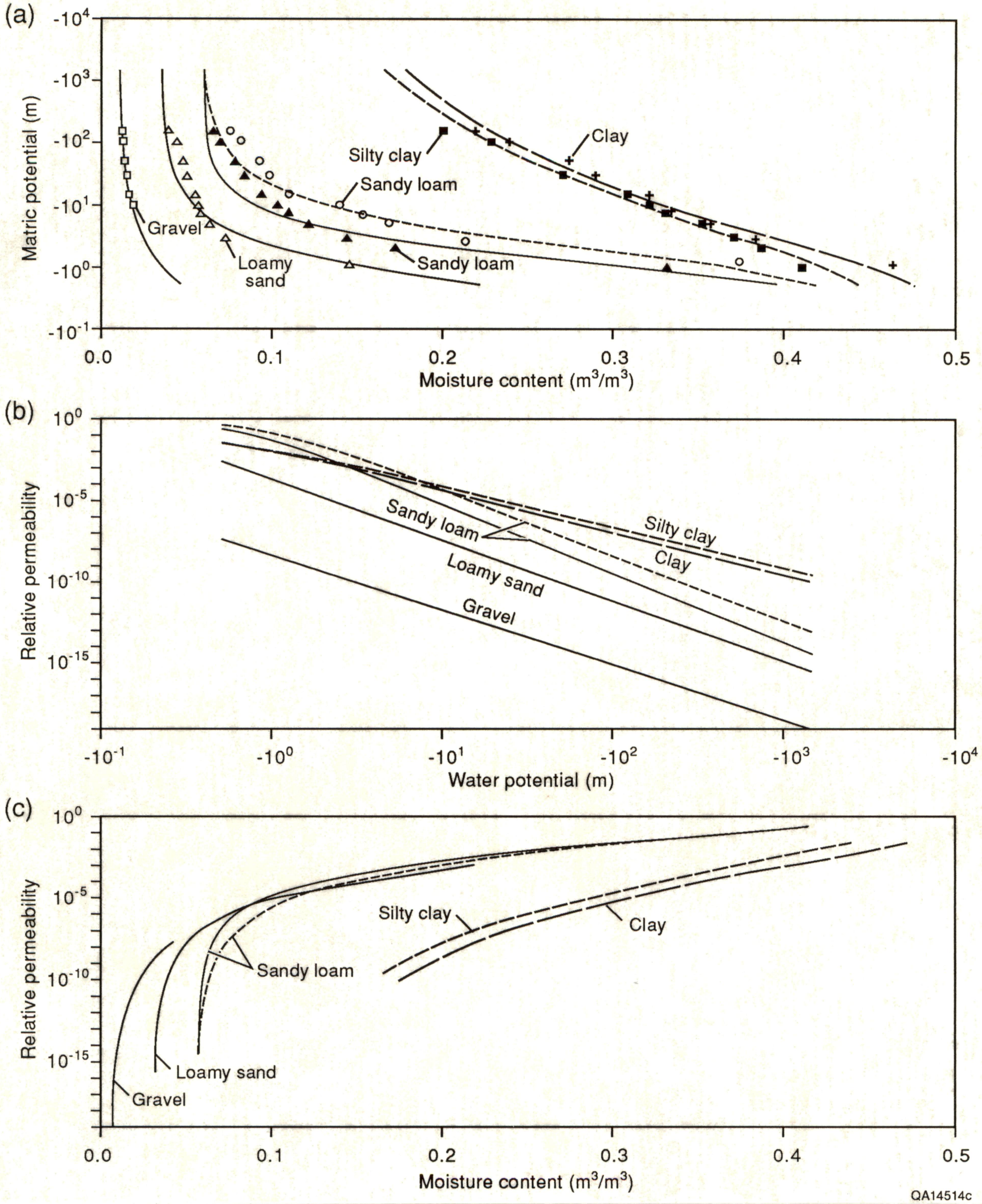

Figure 32. Retention curves for (a) different soil textures and (b,c) calculated relative permeability based on Van Genuchten's equation (eq. 16).

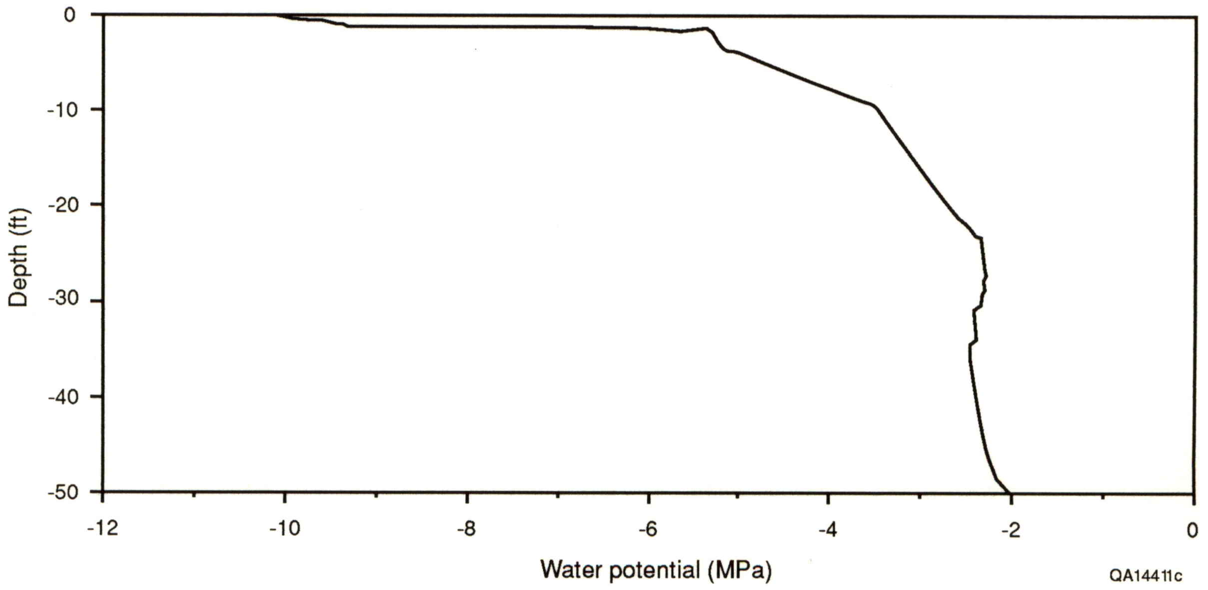

Figure 33. Water-potential gradient based on upward-flow simulation.

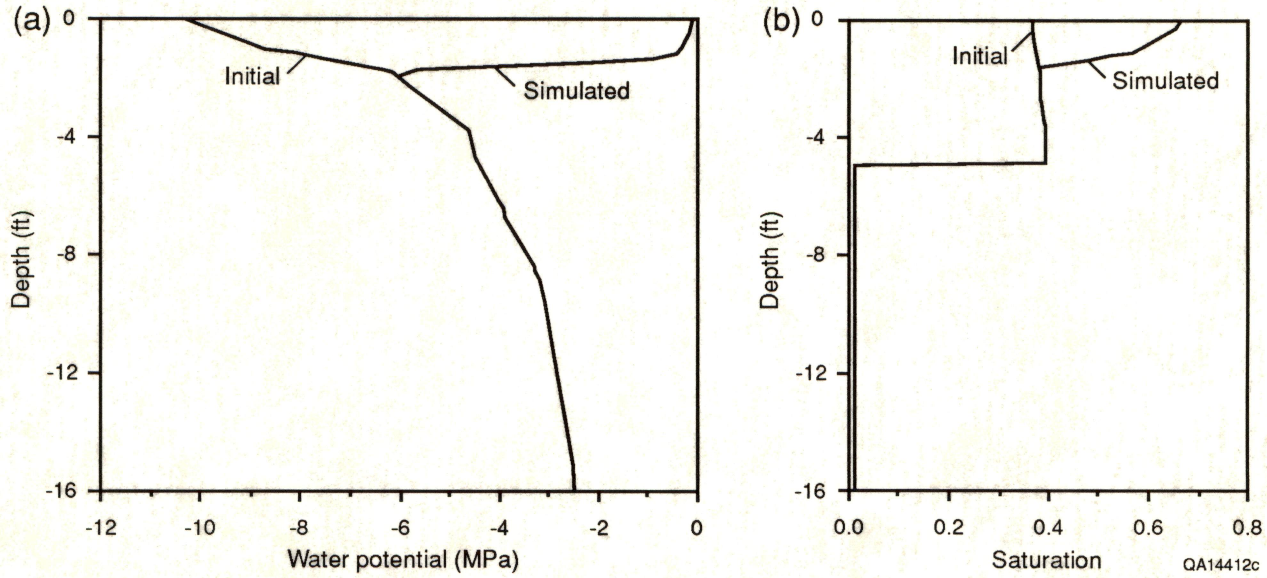

Figure 34. (a) Water potential and (b) saturation profiles based on one-dimensional simulation of infiltration (1.4 mm a^{-1} [0.06 inch a^{-1}] for 35 yr) into a dry system (observed water potentials on Julian day 175 [June 24]).

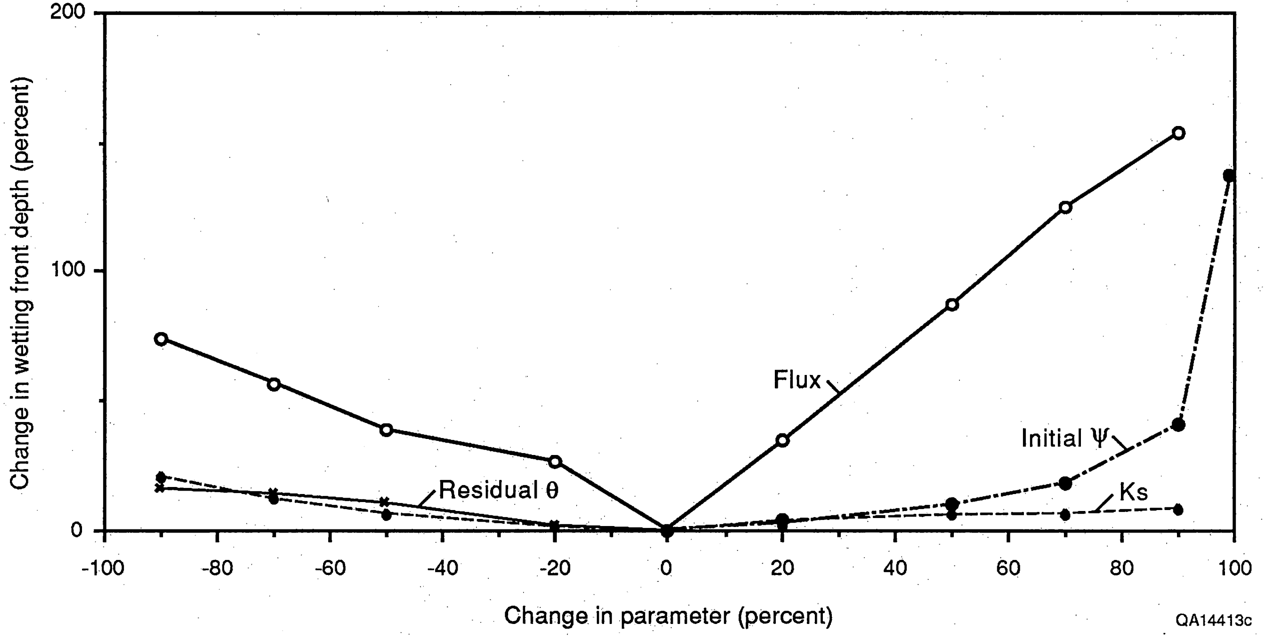

Figure 35. Results of sensitivity analyses evaluating the effect of changing the applied flux, initial water potentials (ψ), residual-water content (θ), and saturated hydraulic conductivity (Ks).

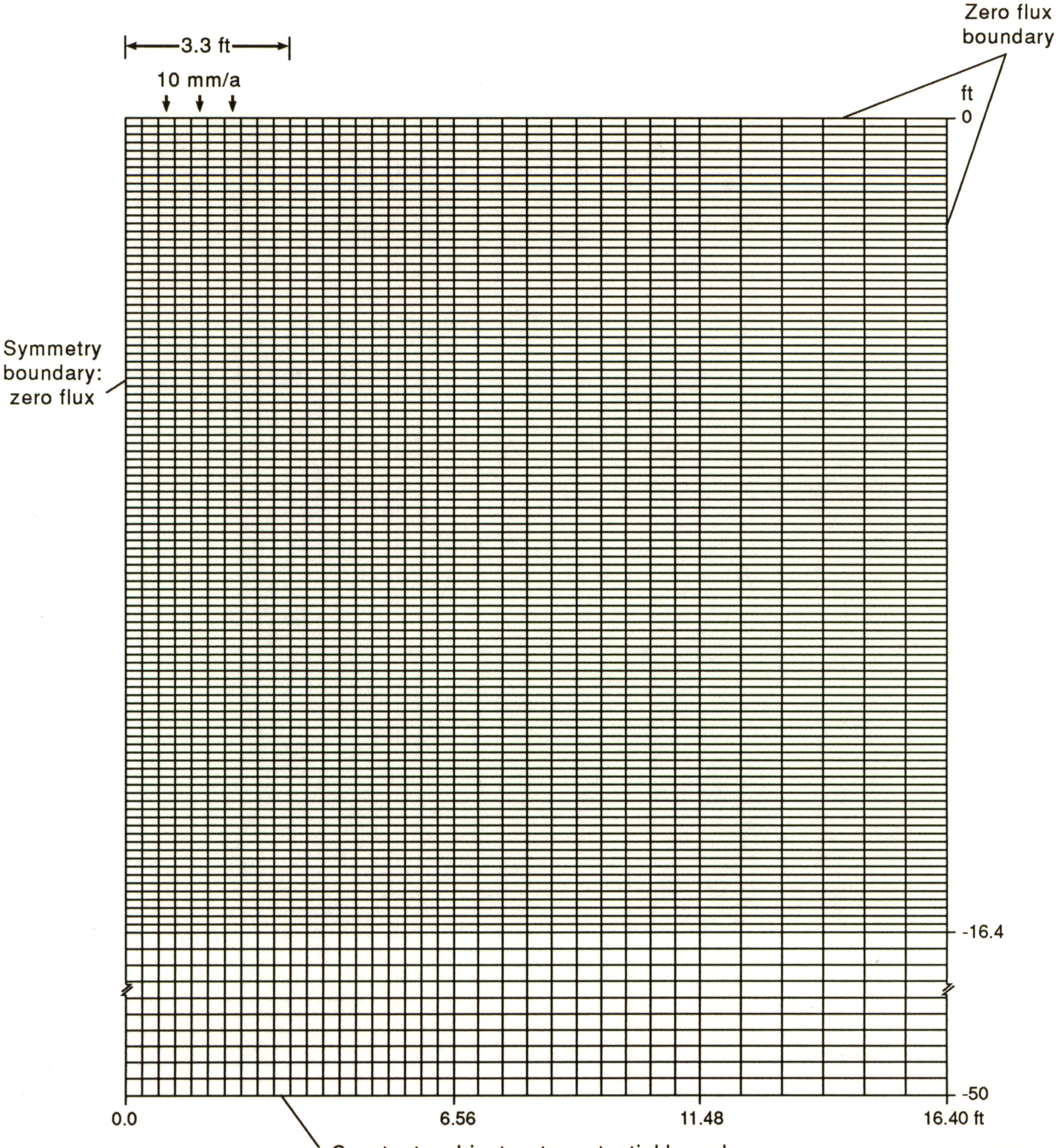

Figure 36. Two-dimensional grid and boundary conditions used in simulations of infiltration.

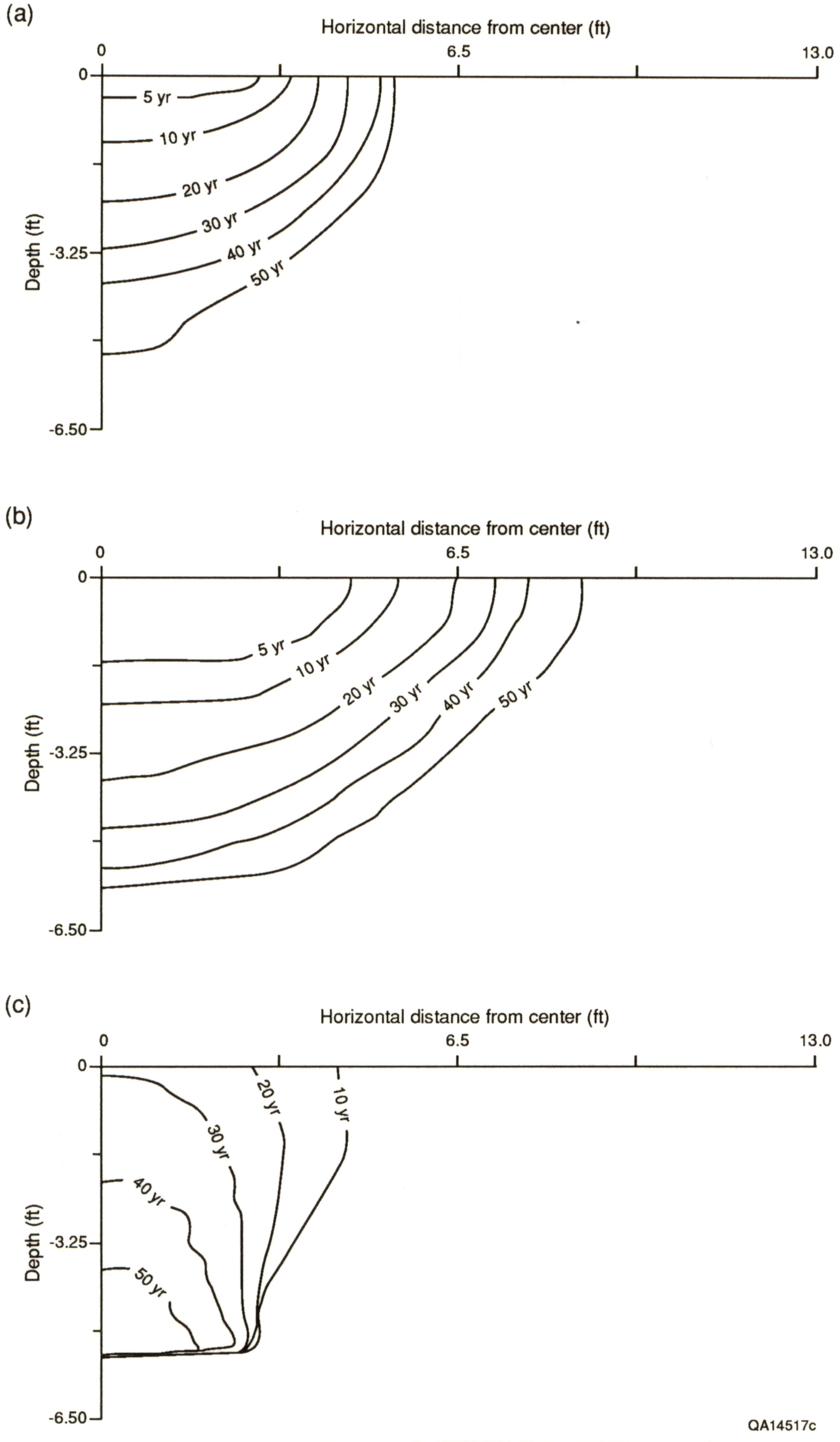

Figure 37. Results of numerical simulations of (a, b) infiltration and (c) redistribution shown by propagation of the (a, c) core of the moisture plume.

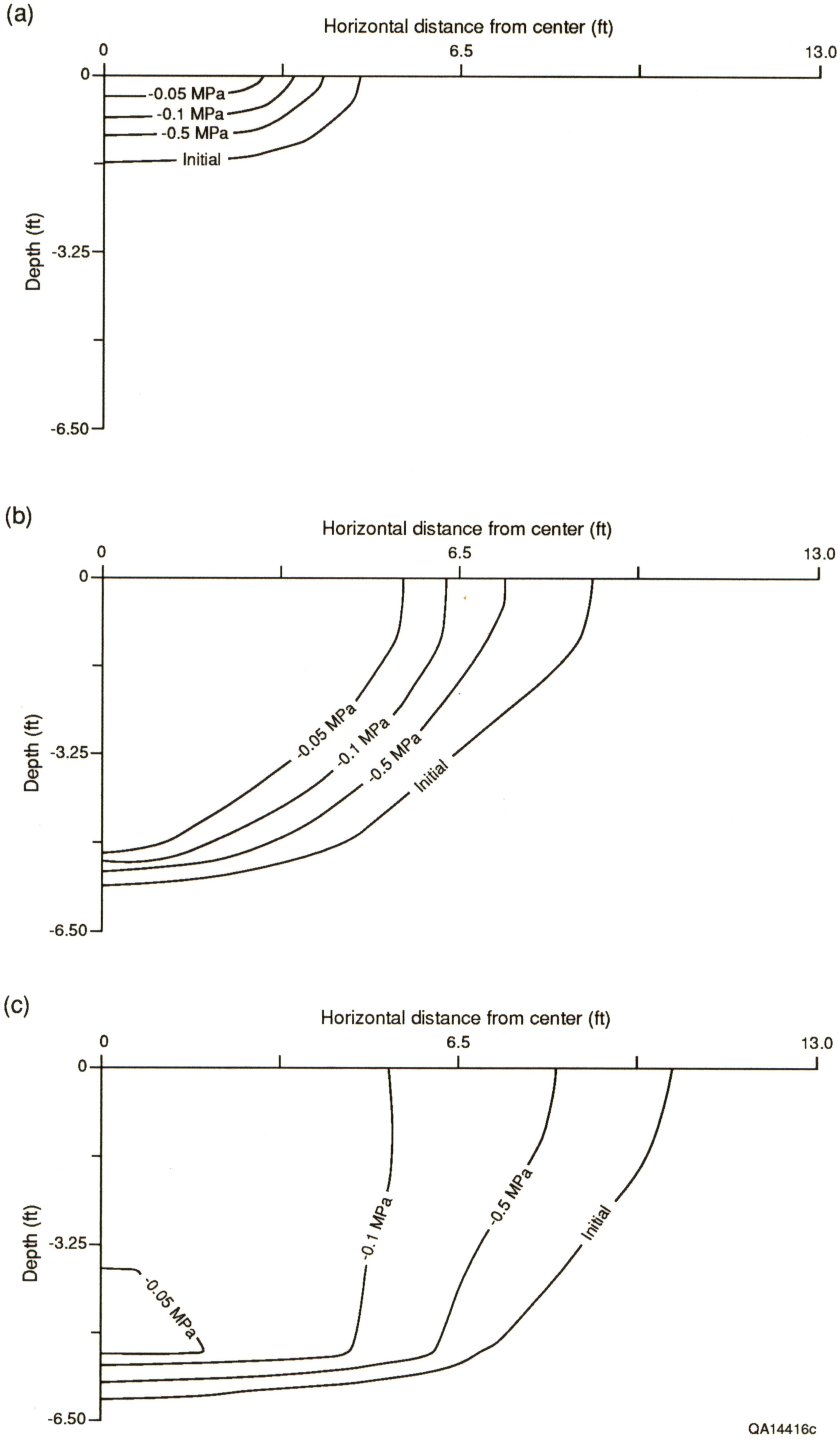

Figure 38. Water-potential gradients at (a) 5 yr and (b) 50 yr, which result from infiltration, and at (c) 100 yr, which result from redistribution.

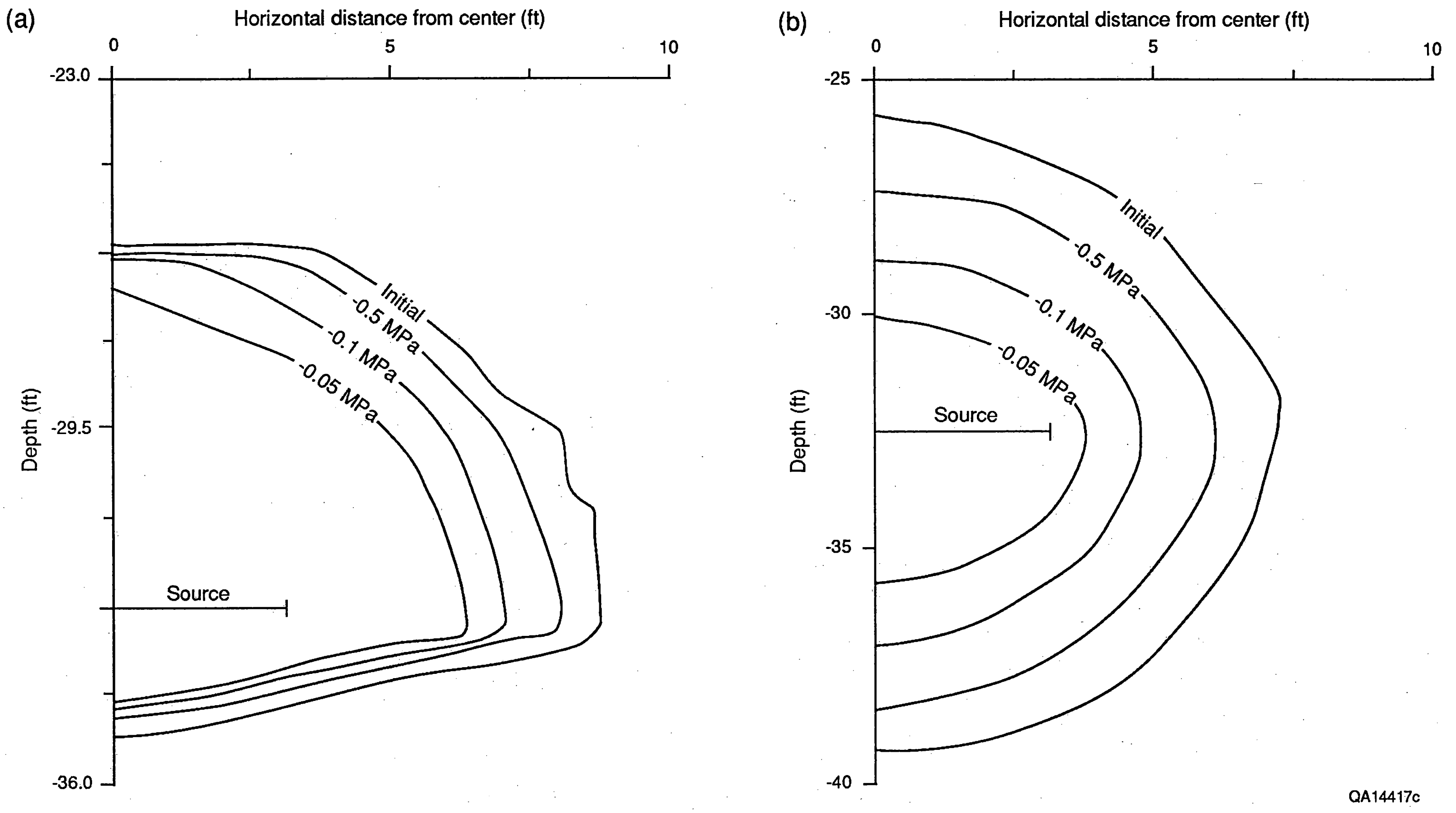

Figure 39. Water-potential gradients that result from applying a constant flux of 10 mm a^{-1} (0.4 inch a^{-1}) at a depth of 10 m (32.8 ft) in (a) a stratified soil system and (b) a homogeneous system. For distribution of lithologies, see figure 31a.

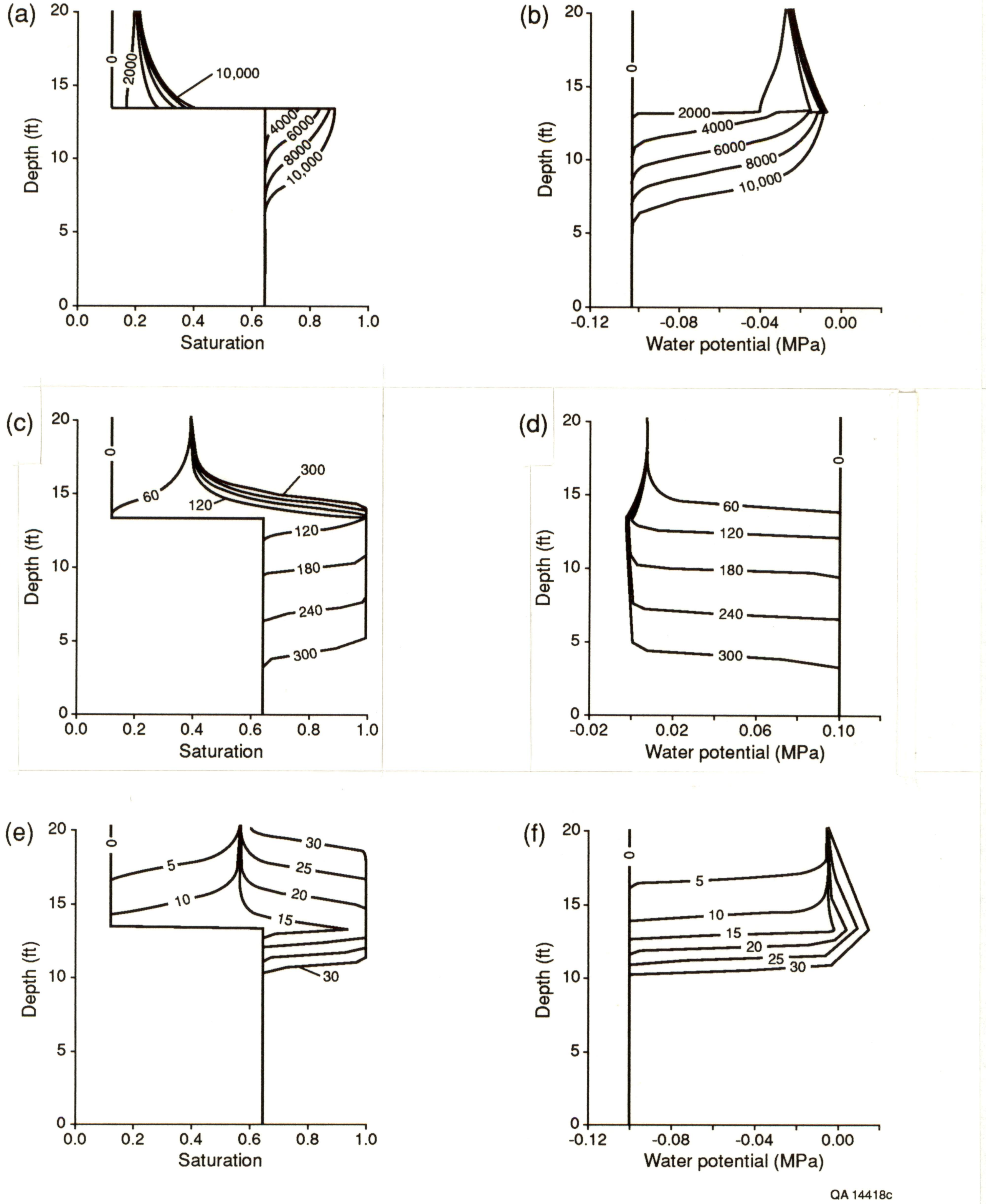

Figure 40. Propagation of wetting front shown by temporal variations in water potential and saturation as a result of applied fluxes of (a, b) 11 mm a^{-1} (0.4 inch a^{-1}), (c, d) 1.1 × 10^{3} mm a^{-1} (43 inches a^{-1}), and (e, f) 1.1 × 10^{4} mm a^{-1} (433 inches a^{-1}).

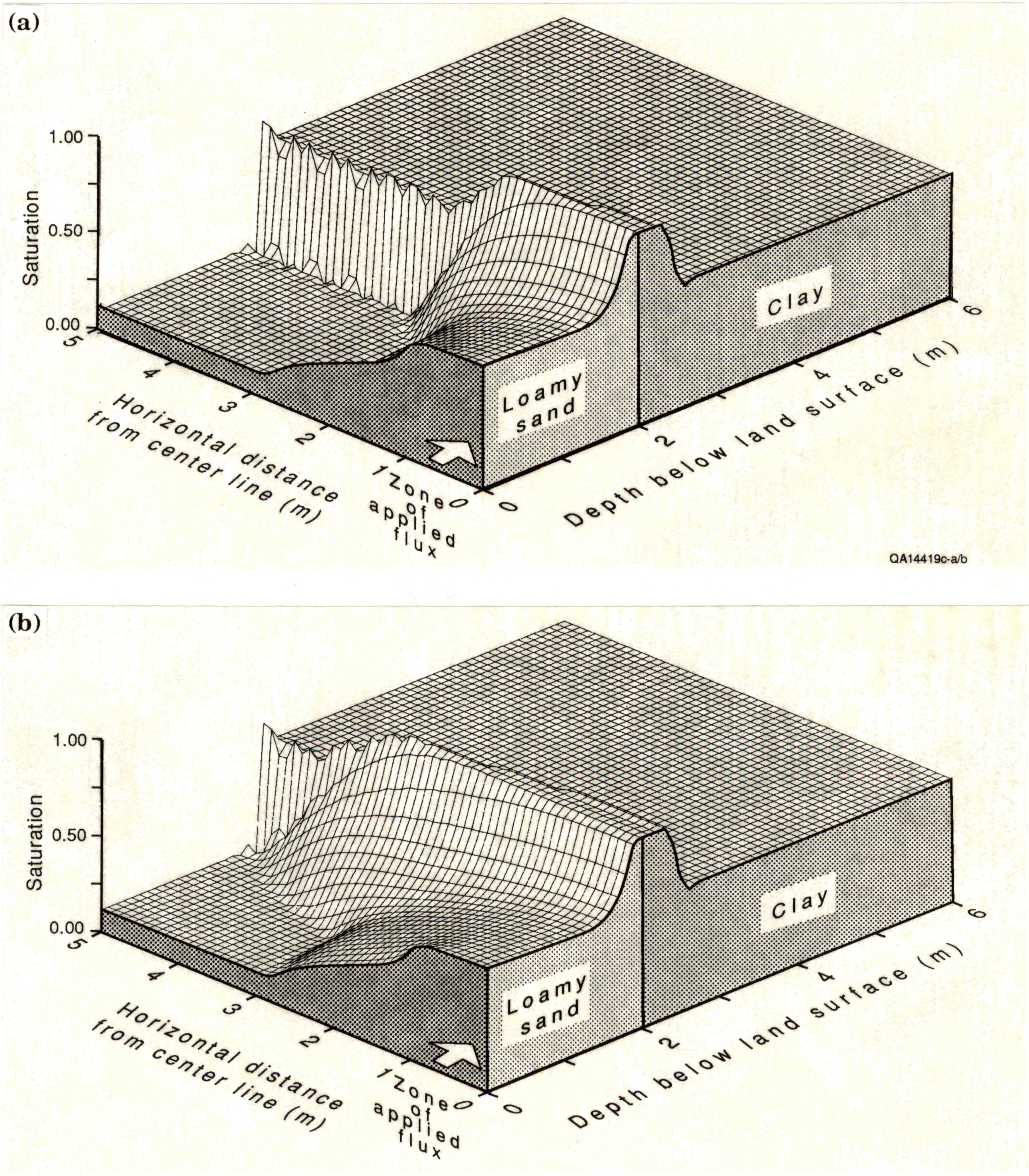

Figure 41. Perspective view of spatial variation in saturation as a result of a flux of 1.1 × 10^4 mm a^{-1} (433 inches a^{-1}) into (a) an isotropic system and (b) an anisotropic system ($K_x = 2 \times K_z$).

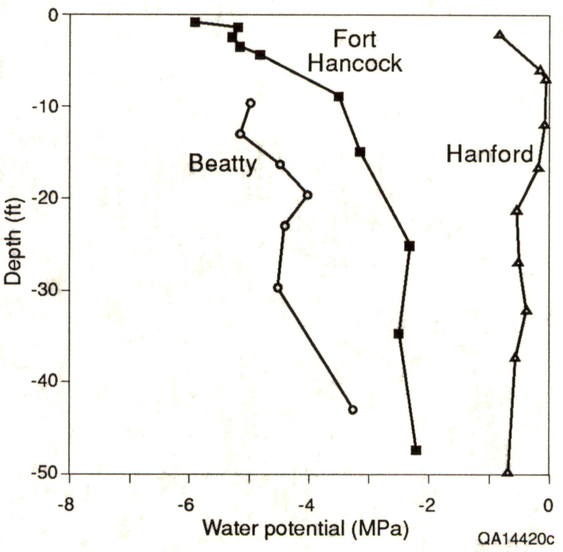

Figure 42. Comparison of water-potential profiles measured at the Fort Hancock, Hanford (Enfield, 1973), and Beatty (Nichols, 1987) study areas.

Table 1. Summary of boreholes drilled, monitoring equipment installed, and type of samples collected.

Borehole no.	Date drilled	Total depth (ft)	No. samples	Type of analysis	Monitoring equipment
15	7/26/88	36	22	Water potential	Soil solution sampler
	7/27/88		38	Moisture content	
			38	Chloride	
18	6/27/88	70	22	Moisture content	Neutron-probe access tube
	6/30/88			Chloride	
19	6/30/88	135	NA	NA	Neutron-probe access tube
20	3/17/89	48	NA	NA	In situ psychrometers
21	6/27/88	67	12	Water potential	
	7/6/88		24	Moisture content	
			24	Chloride	
23	7/19/88	80	14	Water potential	
	7/25/88		13	Moisture content	
			13	Chloride	
27	7/21/88	80	22	Moisture content	
	8/5/88		22	Chloride	
30	1/25/89	48	22	Water potential	
	1/28/89		22	Moisture content	
			22	Chloride	
31	1/29/89	31	20	Water potential	
	1/31/89		17	Moisture content	
			17	Chloride	
41	7/6/88	32	6	Water potential	
	7/8/88				
41C	7/11/88	1	6	Water potential	
41D	7/11/88	0.8	5	Water potential	
42	7/12/88	6	10	Water potential	
50	7/14/88	43	25	Water potential	
	7/15/88		23	Moisture content	
			23	Chloride	
51	2/1/89	14	22	Moisture content	
54	2/2/89	15	18	Water potential	
56	2/2/89	1.6	10	Water potential	
57	2/2/89	1		Water potential	
61	4/5/89	6			Neutron-probe access tube
62	4/5/89	6			Neutron-probe access tube
71					Neutron-probe access tube
74	9/26/89	35	24	Moisture content	
			24	Water potential	

Table 2. Osmotic potentials of NaCl solutions (Lang, 1967) and temperatures used in calibration of in situ psychrometers.

NaCl (molality)	Water Potential (MPa) 15°C	20°C	25°C
0.2	0.88	0.90	0.92
0.5	2.20	2.24	2.28
0.7	3.09	3.15	3.21
1.0	4.46	4.55	4.64
1.5	6.84	6.99	7.13

Table 3. Soil texture and field-saturated hydraulic conductivity results based on Guelph permeameter measurements.

Sample number	Classification	Soil texture				Steady State Outflow Rate (m^3/s)				Kfs Richards Eq. m/s	m/s	Kfs Glover Eq. m/s	m/s	m/s
		Gravel %	Sand %	Silt %	Clay %	Q1	Q2	Q3	Q4					
PG1		28	60	9	3		4.0E–06		4.8E–06	–8.8E–06		7.4E–05		3.3E–05
PG2		24	66	7	3	2.8E–06	4.1E–06			2.6E–05	1.3E–04	7.7E–05		
P1	Clay loam	0	33	35	32	2.6E–07			1.4E–06	9.9E–06	1.2E–05			9.9E–06
P2	Clay loam	0	32	36	32	2.0E–07	4.1E–07	8.1E–07	1.5E–06	6.0E–06	9.3E–06	7.7E–06	8.5E–06	1.0E–05
P3	Clay loam	0	37	35	28	1.8E–07			1.1E–06	8.5E–06	8.0E–06			7.9E–06
P4	Clay loam	0	35	37	28		5.0E–07		1.2E–06	7.6E–06		9.3E–06		8.1E–06
P5	Clay loam	0	36	35	29		5.9E–07		1.5E–06	1.0E–05		1.1E–05		1.0E–05
P6	Clay loam	0	31	32	37		4.4E–07		1.2E–06	8.8E–06		8.2E–06		8.1E–06
P7	Clay	0	25	35	40		5.0E–07		1.4E–06	1.1E–05		9.3E–06		9.5E–06
P8	Clay	1	24	31	34		5.3E–07		1.3E–06	9.3E–06		9.8E–06		9.1E–06
P9	Clay loam	6	39	23	32	9.4E–07		1.6E–06		2.8E–06	4.3E–05		1.7E–05	
P10	Clay	0	16	33	51		4.7E–07		8.2E–07	2.8E–06		8.7E–06		5.6E–06
P11	Clay	0	15	38	47		4.7E–07		9.9E–07	5.5E–06		8.7E–06		6.9E–06
PS1	Sandy loam	0	75	20	5		3.3E–06	4.4E–06		1.9E–05		6.1E–05	4.6E–05	
PS2	Sandy loam	0	71	22	7	2.2E–06	3.0E–06			8.0E–06	9.9E–05	5.6E–05		
PS3	Sandy loam	0	58	32	10	1.9E–06	2.6E–06			3.2E–06	8.8E–05	4.8E–05		
PS4	Loamy sand	0	86	10	4	1.6E–06	2.9E–06			3.7E–05	7.2E–05	5.5E–05		
PS5	Sandy loam	0	73	20	7	1.4E–06	3.0E–06			4.8E–05	6.4E–05	5.5E–05		
PS6	Sandy loam	0	70	19	11	1.7E–06	1.4E–06			9.8E–06	7.7E–05	2.6E–05		
PS7	Sandy loam	0	71	22	7	1.9E–06	3.4E–06			3.8E–05	8.8E–05	6.3E–05		
PS8	Sandy loam	0	64	26	10	1.6E–06	2.6E–06			2.3E–05	7.2E–05	4.9E–05		
PS9	Loam	0	45	42	13	1.1E–06	1.4E–06			2.2E–07	4.9E–05	2.6E–05		

Table 4. Saturated hydraulic conductivity results based on laboratory measurements on cores.

Saturated hydraulic conductivity (Ks=QwL/(AhΔT))

Sample length L (m): 0.06

Sample area A (m^2) : 0.00229

Sample ID	Outflow Qw (m^3)	Head diff., h (m)	Time ΔT(s)	Ks (m/s)	Ks, average (m/s)
3	0.000295	0.111	8160	8.53E–06	
	0.00044	0.094	27360	4.48E–06	6.18E–06
5	0.000319	0.23	1124400	3.23E–08	3.23E–08
6	0.000113	0.342	178080	4.86E–08	
	0.00017	0.342	350040	3.72E–08	
	0.000164	0.342	509400	2.47E–08	3.55E–08
7	0.000228	0.31	427200	4.51E–08	
	0.000213	0.31	341940	5.26E–08	
	0.000203	0.31	350040	4.90E–08	
	0.00023	0.31	508440	3.82E–08	4.59E–08
8	0.000178	0.354	772560	1.71E–08	
	0.000175	0.354	863400	1.50E–08	1.60E–08
9	0.000216	0.315	427200	4.21E–08	
	0.000205	0.317	343620	4.93E–08	
	0.000242	0.317	431040	4.64E–08	4.58E–08
10	0.000202	0.325	691920	2.35E–08	
	0.00013	0.325	513000	2.04E–08	2.19E–08
14	0.000112	0.096	3060	9.99E–06	
	0.000487	0.077	22620	7.33E–06	
	0.000066	0.077	4320	5.20E–06	7.25E–06
15	0.0005	0.06	1320	1.65E–04	
	0.004228	0.024	25260	1.83E–04	1.74E–04
25	0.000125	0.09	1260	2.89E–05	
	0.000262	0.09	1920	3.97E–05	
	0.002931	0.034	25980	8.69E–05	4.64E–05
40	0.000463	0.166	22080	3.31E–06	
	0.000128	0.175	5280	3.63E–06	
	0.000257	0.175	13260	2.90E–06	3.27E–06

Table 5. Soil texture and hydrologic parameters for numerical simulations, which include saturated hydraulic conductivity, bulk density, porosity, and parameters for fitting van Genuchten equation (eq. 16) to laboratory-measured retention data for the wet and dry range.

Sample no.	NU9-8	NU5	PS7	PS3	PSd	PG3
Texture	Clay	Silty clay	Sandy loam	Sandy loam	Loamy sand	Gravel
Gravel (%)	0	0	0	0	0	24
Sand (%)	21	17	64	69	84	58
Silt (%)	30	42	24	21	10	14
Clay (%)	49	41	12	10	6	4
Ks field (m/s)			3.80E–05	3.20E–06	3.70E–05	2.60E–05
Ks lab (m/s)	2.71E–08	3.20E–08	5.20E–05	3.30E–06		
Bulk density	1.30	1.40		1.46		1.56
Porosity	0.51	0.47	0.45	0.45	0.45	0.41
Test problems 1 & 2						
θ_r			0.04	0.03	0.02	0.005
Parameter α			0.0099±0.0054	0.0184±0.0111	0.1530±0.1711	1.2786±3.0151
Parameter n			1.628±0.202	1.612±0.196	1.474±0.135	1.456±0.215
r^2			0.95	0.92	0.90	0.91
MSR			4.11E–04	4.76E–04	8.90E–05	2.50E–06
Test problem 3						
θ_r	0.1	0.08	0.06	0.05	0.03	0.01
Parameter α	0.0138±0.0070	0.0116+0.0045	0.0084±0.0033	0.0117±0.0040	0.0494±0.0252	2.0414±3.947
Parameter n	1.218±0.037	1.202+0.029	1.806±0.226	2.055±0.325	1.790±0.174	1.517±0.123
r^2	0.98	0.98	0.97	0.96	0.97	0.98
MSR	1.06E–04	6.30E–05	2.63E–04	2.59E–04	3.40E–05	0.00E+00

The value after ± gives the difference between 95% confidence intervals.

MSR (Mean Squared Residual)=(Observed(θ)–Predicted(θ^2)/(number of data points).

Table 6. Summary of input data for numerical simulation test problems.

	Test problem 1	Test problem 2					Test problem 3			
		Case 1	Case 2	Case 3	Case 4	Case 5	Case 1	Case 2	Case 4	Case 5
Total simulation time (yr)	10,000	35	50	50	50	50	27	0.08	0.08	0.08
Initial time step size (s)	60	60	60	60	60	60	60	60	60	60
Time step multiplier	1.2	1.2	1.2	1.2	1.2	1.2	1.2	1.2	1.2	1.2
Maximum time step size (d)	100	100	100	100	100	100	100	100	6	6
Problem dimensions (ft)	49	49	49	16 × 13	16 × 49	16 × 49	20	20	16 × 20	16 × 20
Horizontal grid spacing (ft)				0.3–0.8	0.3–0.8	0.3–0.8				
Vertical grid spacing (ft)	0.16–0.3	0.16–0.3	0.16–0.3	0.16–0.3	0.16–0.3	0.16–0.3	0.16–0.3			
Boundary conditions										
Upper (constant ψ) (MPa)	–10		–10							
Upper (constant flux) (mm/yr)		1.4		10	0	0	11	1.1E+04	1.1E+04	1.1E+04
Lower (constant ψ) (MPa)	–2	–2	–2	–3	–2	–2	–0.1	–0.1	–0.1	–0.1
Left (constant flux) (mm/yr)				0	0	0			0	0
Right (constant flux) (mm/yr)				0	0	0			0	0
Source flux (mm/yr)					10	10				
Source depth (ft)					33	33				
Initial conditions (MPa)	2–7	2–10	2–10	3–10	2–10	2–10	–0.1	–0.1	–0.1	–0.1
Isotropic/anisotropic				isotropic	isotropic	isotropic			isotropic	anisotropic
Homogeneous/heterogeneous	Hetero-geneous	Hetero-geneous	Hetero-geneous	Hetero-geneous	Hetero-geneous	homo-geneous	Hetero-geneous	Hetero-geneous	Hetero-geneous	Hetero-geneous

Appendix. Gravitational, water, total, and osmotic potential of samples from 13 boreholes.

Borehole no.	Depth (ft)	Gravitational potential (MPa)	Water potential (MPa)	Total potential (MPa)	Depth (ft)	Osmotic potential (MPa)
15	-0.30	1.5	-0.8	0.7	-0.05	-0.01
	-0.80	1.5	-1.3	0.2	-0.55	0.00
	-1.25	1.5	-11.5	-10.0	-1.05	-0.01
	-2.75	1.5	-10.7	-9.2	-2.95	-0.05
	-4.25	1.5	-8.9	-7.4	-4.05	-0.16
	-5.35	1.5	-8.1	-6.6	-5.35	-0.15
	-13.15	1.4	-6.4	-5.0	-12.95	-0.23
	-14.60	1.4	-6.9	-5.5	-14.75	-0.21
	-15.25	1.4	-6.0	-4.6	-15.05	-0.21
	-16.25	1.4	-4.9	-3.5	-16.05	-0.19
	-16.70	1.4	-4.6	-3.2	-16.45	-0.17
	-17.70	1.4	-5.2	-3.8	-17.50	-0.15
	-18.95	1.4	-4.5	-3.1	-18.75	-0.15
	-18.60	1.4	-5.0	-3.6	-19.15	-0.14
	-20.60	1.4	-5.1	-3.7	-20.75	-0.12
	-21.90	1.4	-4.7	-3.3	-21.68	-0.12
	-23.40	1.4	-4.2	-2.8	-23.60	-0.10
	-25.05	1.4	-4.3	-2.9	-25.35	-0.09
	-26.70	1.4	-4.4	-3.0	-26.50	-0.09
	-28.35	1.4	-4.5	-3.1	-28.10	-0.08
	-31.95	1.4	-4.4	-3.0	-31.65	-0.08
	-35.60	1.4	-3.9	-2.5	-35.83	-0.05
21	-0.75	1.5	-15.6	-14.1	-0.75	-0.01
	-0.98	1.5	-13.3	-11.8	-1.00	-0.01
	-3.08	1.5	-10.9	-9.4	-3.00	-0.25
	-4.49	1.5	-11.6	-10.1	-4.80	-0.27
	-6.00	1.5	-9.4	-8.0	-6.00	-0.19
	-7.81	1.4	-8.0	-6.6	-7.80	-0.24
	-12.50	1.4	-6.7	-5.3	-12.50	-0.25
	-14.80	1.4	-6.4	-5.0	-14.80	-0.27
	-18.21	1.4	-8.9	-7.5	-18.00	-0.20
	-21.00	1.4	-9.9	-8.5	-21.00	-0.14
	-24.02	1.4	-5.2	-3.8	-24.00	-0.20
	-29.99	1.4	-4.5	-3.1	-27.00	-0.17

Appendix (cont.)

Borehole no.	Depth (ft)	Gravitational potential (MPa)	Water potential (MPa)	Total potential (MPa)	Depth (ft)	Osmotic potential (MPa)
23	-0.35	1.5	-1.0	0.5	-0.15	-0.02
	-0.75	1.5	-1.2	0.3	-0.65	-0.01
	-6.65	1.5	-6.5	-5.0	-7.05	-0.37
	-8.35	1.4	-5.4	-4.0	-8.45	-0.36
	-8.85	1.4	-6.7	-5.3	-8.95	-0.36
	-11.60	1.4	-5.9	-4.5	-11.70	-0.38
	-13.35	1.4	-6.0	-4.6	-13.45	-0.41
	-14.73	1.4	-6.3	-4.9	-14.83	-0.40
	-16.15	1.4	-6.8	-5.4	-16.25	-0.33
	-17.70	1.4	-6.8	-5.4	-17.80	-0.33
	-19.15	1.4	-6.0	-4.6	-19.25	-0.32
	-24.00	1.4	-4.4	-3.0	-24.07	-0.34
	-26.00	1.4	-4.9	-3.5	-26.10	-0.27
	-28.00	1.4	-5.1	-3.7	-28.10	-0.30
30	-0.85	1.5	-6.5	-5.0	-0.65	-0.01
	-2.15	1.5	-6.5	-5.1	-1.95	-0.01
	-3.55	1.5	-7.6	-6.1	-3.35	-0.32
	-4.35	1.5	-6.6	-5.1	-4.15	-0.79
30	-4.85	1.5	-6.6	-5.2	-4.65	-0.75
	-5.65	1.5	-6.2	-4.8	-5.45	-0.64
	-9.55	1.4	-5.4	-4.0	-9.35	-0.49
	-10.85	1.4	-4.7	-3.3	-10.65	-0.47
	-11.95	1.4	-4.2	-2.8	0.00	
	-12.85	1.4	-4.1	-2.7	-12.65	-0.42
	-13.85	1.4	-4.0	-2.6	-13.65	-0.42
	-17.75	1.4	-3.6	-2.2	-17.55	-0.39
	-20.85	1.4	-3.7	-2.3	-20.65	-0.26
	-23.85	1.4	-3.9	-2.5	-23.65	-0.25
	-27.35	1.4	-2.8	-1.4	-27.15	-0.21
	-29.85	1.4	-3.4	-2.1	-29.65	-0.16
	-32.85	1.4	-2.2	-0.9	-32.65	-0.16
	-35.55	1.4	-3.4	-2.0	-35.35	-0.15
	-38.15	1.4	-2.5	-1.2	-37.95	-0.13
	-44.35	1.3	-2.7	-1.3	-44.15	-0.03
	-46.85	1.3	-3.0	-1.7	-46.65	-0.02

Appendix (cont.)

Borehole no.	Depth (ft)	Gravitational potential (MPa)	Water potential (MPa)	Total potential (MPa)	Depth (ft)	Osmotic potential (MPa)
31	-0.35	1.5	-5.3	-3.8	-0.95	-0.01
	-0.75	1.5	-5.5	-4.1	-1.95	-0.04
	-1.35	1.5	-4.7	-3.2	-2.65	-0.03
	-1.75	1.5	-4.0	-2.6	-3.55	-0.30
	-2.65	1.5	-5.2	-3.8	-4.50	-0.43
	-3.35	1.5	-5.1	-3.6	-5.35	-0.39
	-3.75	1.5	-5.3	-3.9	-6.15	-0.19
	-4.80	1.5	-5.6	-4.1	-6.80	-0.18
	-5.55	1.5	-7.1	-5.6	-12.45	-0.26
	-6.35	1.5	-5.5	-4.0	-13.65	-0.33
	-7.00	1.5	-6.8	-5.3	-14.65	-0.35
	-12.85	1.4	-5.1	-3.6	-15.05	-0.22
	-13.85	1.4	-4.3	-2.8	-22.10	-0.18
	-14.85	1.4	-3.9	-2.5	-23.65	-0.19
	-15.35	1.4	-4.4	-3.0	-26.65	-0.17
	-22.30	1.4	-2.7	-1.3	-28.15	-0.22
	-23.85	1.4	-3.0	-1.6	-31.05	-0.18
	-26.85	1.4	-2.8	-1.4	0.00	
	-28.35	1.4	-3.2	-1.8	0.00	
	-31.25	1.6	-3.2	-1.6	0.00	
41	-0.09	1.5	-0.2	1.3	0.00	
	-0.25	1.5	-0.1	1.4	0.00	
	-0.42	1.5	-0.1	1.4	0.00	
	-0.58	1.5	-13.2	-11.7	0.00	
	-0.75	1.5	-13.5	-12.0	0.00	
	-0.92	1.5	-12.3	-10.8	0.00	
	-1.05	1.5	-11.6	-10.1	0.00	
	-1.87	1.5	-8.8	-7.3	0.00	
	-3.08	1.5	-8.1	-6.6	0.00	
	-4.92	1.5	-6.2	-4.7	0.00	
	-7.55	1.4	-3.7	-2.3	0.00	
	-9.65	1.4	-2.8	-1.4	0.00	

Appendix (cont.)

Borehole no.	Depth (ft)	Gravitational potential (MPa)	Water potential (MPa)	Total potential (MPa)	Depth (ft)	Osmotic potential (MPa)
42	-0.60	1.5	-0.2	1.3	0.00	
	-1.10	1.5	-11.8	-10.3	0.00	
	-1.60	1.5	-7.1	-5.6	0.00	
42	-2.10	1.5	-4.8	-3.3	0.00	
	-2.60	1.5	-6.6	-5.1	0.00	
	-3.10	1.5	-6.5	-5.0	0.00	
	-3.60	1.5	-6.6	-5.1	0.00	
	-4.10	1.5	-6.5	-5.0	0.00	
	-4.60	1.5	-5.9	-4.4	0.00	
	-5.10	1.5	-3.7	-2.2	0.00	
50	-0.20	1.5	-0.1	1.4	-0.45	0.00
	-0.70	1.5	-0.1	1.4	-0.95	0.00
	-1.45	1.5	-1.6	-0.1	-1.70	-0.01
	-2.20	1.5	-4.3	-2.8	-2.45	-0.03
	-3.95	1.5	-4.0	-2.5	-4.20	-0.16
	-4.95	1.5	-4.9	-3.4	-5.20	-0.22
	-5.95	1.5	-4.3	-2.8	-6.20	-0.28
	-6.95	1.5	-4.1	-2.7	-7.20	-0.30
	-7.95	1.4	-3.1	-1.7	-8.20	-0.33
	-8.95	1.4	-3.7	-2.3	-9.20	-0.30
	-9.95	1.4	-4.2	-2.8	-10.20	-0.24
	-11.20	1.4	-3.2	-1.8	-11.45	-0.24
	-12.20	1.4	-3.7	-2.3	-12.45	-0.19
	-13.20	1.4	-3.9	-2.5	-13.45	-0.10
	-14.75	1.4	-3.5	-2.1	-14.65	-0.06
	-19.50	1.4	-4.1	-2.7	-20.55	-0.05
	-20.80	1.4	-4.2	-2.8	-21.55	-0.04
	-21.80	1.4	-3.5	-2.1	-23.95	-0.04
	-23.70	1.4	-2.7	-1.3	-26.45	-0.03
	-26.20	1.4	-3.5	-2.1	-29.95	-0.04
	-29.70	1.4	-2.4	-1.0	-34.05	-0.05
	-31.70	1.4	-2.8	-1.4	-37.55	-0.05
	-34.70	1.4	-3.9	-2.5	-42.70	-0.05
	-37.80	1.4	-2.4	-1.0	0.00	
	-42.45	1.3	-2.5	-1.2	0.00	

Appendix (cont.)

Borehole no.	Depth (ft)	Gravitational potential (MPa)	Water potential (MPa)	Total potential (MPa)	Depth (ft)	Osmotic potential (MPa)
54	-0.35	1.5	-4.7	-3.2	0.00	
	-0.85	1.5	-5.3	-3.8	0.00	
	-1.35	1.5	-6.5	-5.1	0.00	
	-1.85	1.5	-6.9	-5.5	0.00	
	-2.35	1.5	-7.4	-5.9	0.00	
	-2.85	1.5	-7.4	-6.0	0.00	
	-3.35	1.5	-7.6	-6.1	0.00	
	-3.85	1.5	-7.1	-5.6	0.00	
	-4.35	1.5	-6.7	-5.3	0.00	
	-4.85	1.5	-6.6	-5.2	0.00	
	-5.85	1.5	-6.7	-5.3	0.00	
	-6.85	1.5	-6.2	-4.7	0.00	
	-7.85	1.4	-4.7	-3.3	0.00	
	-8.85	1.4	-4.2	-2.7	0.00	
	-9.85	1.4	-3.7	-2.3	0.00	
	-10.35	1.4	-3.7	-2.2	0.00	
	-11.85	1.4	-3.2	-1.8	0.00	
	-12.85	1.5	-3.1	-1.6	0.00	
56	-0.08	1.5	-13.7	-12.2	0.00	
	-0.25	1.5	-11.3	-9.8	0.00	
56	-0.41	1.5	-7.4	-5.9	0.00	
	-0.57	1.5	-5.4	-3.9	0.00	
	-0.74	1.5	-4.3	-2.8	0.00	
	-0.90	1.5	-5.7	-4.2	0.00	
	-1.07	1.5	-8.9	-7.4	0.00	
	-1.23	1.5	-3.6	-2.1	0.00	
	-1.39	1.5	-3.5	-2.0	0.00	
	-1.56	1.5	-4.0	-2.5	0.00	
57	-0.08	1.5	-8.5	-7.0	0.00	
	-0.25	1.5	-7.0	-5.5	0.00	
	-0.41	1.5	-3.6	-2.1	0.00	
	-0.57	1.5	-2.6	-1.1	0.00	
	-0.74	1.5	-2.6	-1.1	0.00	
	-0.90	1.5	-2.4	-0.9	0.00	
	-1.07	1.5	-2.5	-1.0	0.00	

Appendix (cont.)

Borehole no.	Depth (ft)	Gravitational potential (MPa)	Water potential (MPa)	Total potential (MPa)	Depth (ft)	Osmotic potential (MPa)
74	-0.35	1.5	-7.9	-6.4	-0.15	-0.06
	-0.85	1.5	-4.6	-3.1	-0.65	-0.01
	-2.35	1.5	-8.8	-7.3	-2.15	-0.03
	-3.35	1.5	-8.2	-6.8	-3.15	-0.02
	-4.35	1.5	-11.5	-10.0	-4.15	-0.04
	-5.30	1.5	-7.2	-5.7	-5.10	-0.19
	-6.35	1.5	-8.1	-6.7	-6.15	-0.07
	-9.35	1.4	-6.9	-5.5	-9.15	-0.83
	-10.15	1.4	-9.0	-7.6	-9.95	-0.65
	-13.35	1.4	-7.9	-6.5	-13.15	-0.49
	-14.35	1.4	-8.4	-7.0	-14.15	-0.68
	-15.60	1.4	-7.8	-6.4	-15.40	-1.14
	-17.15	1.4	-6.4	-5.0	-16.95	-0.19
	-18.85	1.4	-6.1	-4.7	-18.75	-0.13
	-20.35	1.4	-7.2	-5.8	-20.15	-0.34
	-21.85	1.4	-6.6	-5.2	-21.65	-0.33
	-23.15	1.4	-7.5	-6.1	-22.95	-0.29
	-24.55	1.4	-8.0	-6.6	-24.35	-0.21
	-27.65	1.4	-3.4	-2.0	-27.45	-0.06
	-28.90	1.4	-2.7	-1.3	-28.70	-0.06
	-30.55	1.4	-2.9	-1.6	-30.35	-0.06
	-31.70	1.4	-2.9	-1.5	-31.70	-0.07
	-33.35	1.4	-2.9	-1.6	-33.15	-0.07
	-34.35	1.4	-2.6	-1.2	-34.35	-0.06